Linewidth modelling and measurements of single-mode VCSELs

Thesis submitted for the master degree in

Nanotechnologies for ICTs

at

Politecnico di Torino

Author:

Marco Novarese

Supervisor:

Francesco Bertazzi

Co-supervisors:

Pierluigi Debernardi

Michele Goano

Alberto Tibaldi

Anders Larsson

Abstract

The vertical-cavity surface-emitting laser (VCSEL) is used for many applications and is today produced in large volumes for optical interconnects in data centres, gas sensors, and smart-phones. Some of these applications require the VCSEL to be single-mode, in other words to achieve a single spectral emission line. The linewidth, which is related to the phase noise and coherence of the laser, represents the width of such emission. It depends on the design of the single-mode VCSEL and on the operating conditions. This thesis work covers the analysis of VCSEL lasers, from basic power vs current to linewidth measurements, developed at Chalmers University of Technology.
Since the theory for the linewidth formulation is well developed, the present thesis doesn't focus on it. Rather the involved physical quantities are retrieved in a much more accurate way with respect to the common literature models. For such purpose a theoretical study of the physics of the strained quantum wells (QWs) forming the active regions of the device is presented. The used code is one of the constituents of the VCSEL electro-opto-thermal numerical simulator VENUS [1] that has been revised and modified to include a strained structure also able to simulate different QWs. The calculation of the electronic band structure and the optical properties of the nano-structure are described in this thesis work. Strain is included in the calculation of the band structure based on the $\mathbf{k}\cdot\mathbf{p}$ method by implementing a conduction band offset model to retrieve the changes in the band structures of the material composing the wells.
The next step involves the assembling of 8x8 Hamiltonian with strain related terms which is later block diagonalized to obtain a 4x4 Hamiltonian. The implemented $\mathbf{k}\cdot\mathbf{p}$ method also includes the so called Burt–Foreman ordering that mitigates spurious solution in the QW band gap. Moreover the parameters of the well have all been changed and adjusted to have results very similar with the experiments. To perform such comparisons the previously calculated band structure and sub-bands are used to extract quantities such as the spontaneous emission, refractive index change, photolumiscence peak, and gain. The whole description is completed with a brief description of the many body effects related to the Coulomb interactions between charge carriers leading to the re-normalization of the gap. Then the performed measurements at Chalmers are shown and explained. In this framework different type of VCSELs are taken into consideration and characterized

in many ways: I-P-V, spectrum, near field imaging of the spontaneous emission and linewidth are collected for all of them together with an in depth explanation of the used set-up and and related problems in the measurements.
The whole data is sampled for different temperatures to see how the devices operate in different ambient conditions.
In conclusion the experimental linewidth of the VCSELs are obtained. Then a comparison with the theory is carried out using the previously obtained linewidth normalised with respect to the inverse of the power. To do so the physical quantities from the model are used in conjunction with an appropriate fitting with the experiment.
The theoretical part of the thesis has been carried out at Politecnico di Torino and CNR-IEIIT, while the experiments have been performed at Chalmers in the Photonics Laboratory at the department of Microtechnology and Nanoscience.

Contents

1 Introduction **7**

1.1 Motivation . . . 7

1.2 VENUS . . . 8

1.3 Thesis structure . . . 10

I Theoretical part **11**

2 VCSEL **13**

2.1 Semiconductor lasers . . . 13

2.2 VCSEL structure . . . 15

2.2.1 Electrical Contacts . . . 15

2.2.2 Distributed Bragg Reflactors . . . 16

2.2.3 Oxide apertures . . . 16

2.2.4 Substrate . . . 17

2.2.5 Anti-phase and Surface relief . . . 17

2.2.6 Active region . . . 17

2.3 Linewidth . . . 17

3 InGaAs/GaAsP Quantum well **23**

3.1 Strain . . . 23

3.2 Strain models . . . 27

3.2.1 Model solid theory . . . 27

3.2.2 Harrison model . . . 29

3.3 Band Diagram . . . 30

4 k·p method **35**

4.1 Introduction . . . 35

4.2 Bulk case . . . 36

4.3 QW case . . . 37

4.3.1 8x8 **k·p** formulation . . . 40
4.3.2 4x4 **k·p** Strain Hamiltonian . . . 42
4.4 QW sub-bands . . . 46

5 Optical processes **55**
5.1 Dielectric constant . . . 55
5.2 Many body effects . . . 61
5.3 Linewidth parameters . . . 65
5.4 Theoretical part: conclusion . . . 72

II Experimental part **75**

6 IPV and spectrum **77**
6.1 Introduction . . . 77
6.2 VCSELs category . . . 77
6.3 IPV . . . 80
6.4 Spectrum . . . 88

7 Near field spontaneous emission **93**
7.1 Set-up . . . 93
7.2 Results . . . 94

8 Linewidth **97**
8.1 Linewidth set-up: SFPI . . . 97
8.2 Linewidth measurement . . . 99
8.3 Theory comparison . . . 102

9 Conclusion **107**
9.1 Future work . . . 108

A Techniques for linewidth measurements **109**

Chapter 1

Introduction

1.1 Motivation

Nowadays VCSELs represent one of the state of the art of the laser industry. The reasons are found in the fact that they are low-cost light source with many interesting performances, such as low operating current and miniaturization. The low fabrication cost is due to the ease of performing on-wafer testing and screening of broken/ not working part of the device during the whole fabrication. High speed performances at low currents and a a good beam shape enabling easy fiber-coupling make VCSELs very attractive, also on the energy efficient side [2]. This together with its fairly easy integration in two-dimensional arrays makes it a good candidate for short-distance single links [4], and much more other applications. For example gas sensing, laser printing, optical storage are other fields in which VCSELs are used.
The first VCSEL was conceived in 1979 by K. Iga [6], from Tokyo Institute of Technology, Where the possibility to collect light directly from the top surface of the device was roughly sketched. From that moment many improvements were made and more than 1 billion of units were sold worldwide. Each delivered laser must behave and work correctly in the specified range. In this contest, the linewidth is one of the key parameters that correlates with a requested low noise application.
Here the emission peak should be as sharp as possible at the desired wavelength in order to perform high precision tasks such as low-power atomic sensors based on spectroscopic analysis of alkali atoms [7].
For this reason optimization of VCSELs is mandatory. To do so CAD analysis of the structure are becoming more and more important to arrive to a viable structure without having to test many expensive different configuration experimentally. The scope of this thesis is to apply corrections to the given code of the gain of a Quantum well and most importantly to extend it in order to include the strain and make it possible to simulate different single mode VCSELs active regions. The complete device is then being simulated in VENUS and the obtained outcomes compared to the measurements performed

on VCSELs at Chalmers. In this way the code is validated with the experiments.

1.2 VENUS

Vertical-cavity surface-emitting laser Electro-opto-thermal NUmerical Simulator (VENUS) [1] is a simulator aimed to deeply describe the physics of a VCSEL. It is mainly constituted of four blocks which communicate one with the other depending on their role as depicted in figure taken from [1], in the paper all the blocks are heavily described and the results of the total simulation presented in the case of a AlGaAs/GaAs Quantum well.
For clarity and completeness here the main blocks are briefly summarized, the Quantum

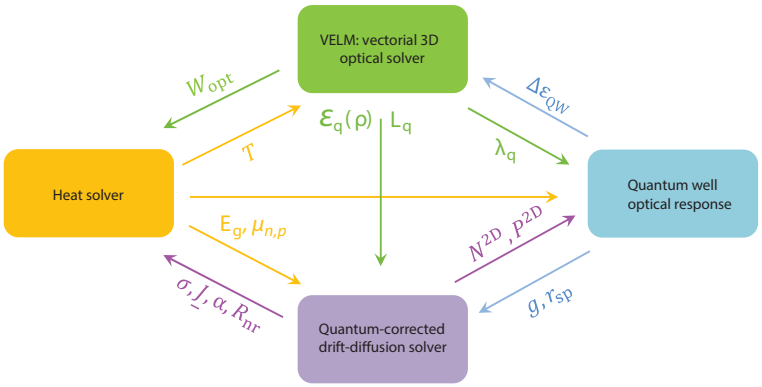

Figure 1.1: Representation of Venus block and how they interact with each other.

Well block is not discussed since this thesis work is based on it and so an in depth explanation is given later.

- **VELM**: The model is based on the couple mode theory applied to the electromagnetic field in the cavity expanded in TE and TM modes [8]. In other words the total electromagnetic field may be written as a sum of the modal basis $\mathbf{E}_\mu$:

$$\boldsymbol{\mathcal{E}}(\rho,\phi,z) = \sum_\mu \int A_\mu(z,k)\mathbf{E}_\mu(\rho,\phi,z)dk. \tag{1.1}$$

  Where the modal field basis is known and expressed in cylindrical components, k is the wave vector referring to the continuous radial variation of the modes, and $A_\mu(z,k)$ is the amplitude of the mode μ. With the latter to be found.
  To do so the integral in eq. is discretized in $A_\mu\Delta k$ and the unknown vector $\mathbf{A} = \{A_\mu\Delta k\}$ is obtained by proper solution of the coupled-mode equations. Since the VCSEL structure is vertical and formed by many layers deposited one on the other, the couple mode theory is a good way to proceed in order to determine the propagating field by dividing the whole structure in a sufficient number of layers of thickness L_i. The amplitude of the modes comes from the solution of equation

$$\frac{d\mathbf{A}}{dz} = (B + K_{\mu\mu'}\Delta k)\mathbf{A}, \tag{1.2}$$

with B being the diagonal matrix describing the propagation of the wave in the reference material, so both forward and backward waves will be present (different sign). Lastly the coupling between different modes is kept into account in the coupling coefficient $K_{\mu\mu'}$.
As shown in [8] in order to find the mode coefficients, the boundary condition at the extreme upper and lower layers are related one with the other using a transmission matrix made by the products of the transmission matrices of each laye;, in this way an eigenvalue problem for $\boldsymbol{A}(0)$ can formulated and numerically solved. Then, thanks to 1.1, the total field distribution at $z = 0$ is retrieved, while for other layers, eq. 1.2 is used. The output of the simulation are then the modal losses L_q, the profile of the field for each mode $\boldsymbol{\mathcal{E}}_q$, and the related wavelength λ_q.

- **Drift-diffusion** In this block the effect of the electrons and holes flowing into the active region from the surrounding layers is considered. A drift diffusion model is used together with quantum correction [9] to take into account the effect of the confined direction. Thus carriers are separated in bulk and bound carriers, where the first one is described with the normal drift-diffusion model and the second one are distributed along the confined direction of the QW. The lasing is then described by the solution of the rate equations in static condition so that all time derivatives are equal to zero:

$$\begin{cases} \nabla^2\psi = \frac{q}{\epsilon}(p^{3D} - n^{3D} + p^{2D} - n^{2D} + N_D^+ - N_A^-) \\ \frac{1}{q}\nabla \cdot \boldsymbol{\mathcal{J}}_{n^{3D}} = U_n^{3D} \\ \frac{1}{q}\nabla \cdot \boldsymbol{\mathcal{J}}_{p^{3D}} = U_p^{3D} \\ \frac{1}{q}\nabla \cdot \boldsymbol{\mathcal{J}}_{N^{2D}} = U_n^{2D} \\ \frac{1}{q}\nabla \cdot \boldsymbol{\mathcal{J}}_{P^{2D}} = U_p^{2D} \\ \Gamma_z(G'_q - L'_q)P_{st,q'} + \Gamma_z S'_q = 0 \end{cases} \tag{1.3}$$

Here the unknowns are the electrostatic potential in well ψ, the bulk (n^{3D}, p^{3D}) and bound (N^{2D}, P^{2D}) carrier densities and the stimulated power at the output of the VCSEL for each node q'. The current density for electrons and holes are expressed in the usual way by including a drift and diffusion component, where in the drift part an additional potential is present to take into account the heterointerfaces and Fermi Dirac distribution. U is the recombination rates for bound and bulk carriers which contains Auger, SHR and spontaneous recombinations effects.
Considering the electrons and holes, since they are placed in different states, it may possible for the to couple and change state. This effect is taken into account in a capture term, $C_{n/p}^{CAP}$ related to the scattering event between continuum and bound states for both electrons and hole. At the equilibrium it is equal to zero while far from it, it is associated to the exchange of type of carrier from 2D to 3D or vice versa.

- **Heat solver** The effect of the temperature hugely affects the VCSEL behaviour, from the gain reduction to the shift of wavelength (or frequency) at which lasing begins, it limits and changes physical quantities in the laser.
  Absorption, Joule effect, Recombination (from non-radiative processes) and the heating related to $C_{n/p}^{CAP}$ are the sources included to find the total heat generated by the laser.
  Having defined all the processes, an adaptive mesh is used to better describe the active region with respect to the substrate where the temperature has a linear behaviour so less mesh nodes may be used to describe it.
  Once the the whole profile of Temperature is known, all the variables depending on it are updated.

1.3 Thesis structure

This thesis is divided in two main parts.
The first one includes the physics behind the Quantum Well used to retrieve the quantities involved in the calculation of the linewidth. In Chapter 2 the studied VCSEL is presented and described explaining the role of each component, here a brief review on the theory related to the linewidth expression is presented too. Then Chapter 3 covers the strained band diagram of the active region. This is followed by the introduction of the **k·p** method in Chapter 4.The general model is described with the inclusion of strain mechanisms and compared to the un-strained case to see the impact on the sub-bands of the QW. Chapter 5 then contains the theory of the gain, spontaneous emission and refractive index together with effects such as gap re-normalization to be applied to the QW in order to reach an outcome close to the real behaviour of the device.
The second main part contains the measurements made at Chalmers. Chapter 6 describes the analysed VCSELs describing them by means of their spectrum and IPV (current power voltage) or also called LIV (light current voltage)curves. The effect of the temperature is included too. Chapter 7 presents the near field spontaneous Emission used to verify the difference in phase noise between the VCSELs. Chapter 8 finally contains the linewidth of the lasers together with the methods considered to obtain it and related problems. Here the theoretical normalized linewidth is computed and compared to the theory by fitting experimental parameters. Lastly Chapter 9 draws out the conclusion of the project.

Part I

Theoretical part

Chapter 2

VCSEL

2.1 Semiconductor lasers

A laser is a light source emitting coherent radiation through stimulated emission of photons. This process is achieved in the active region where an external source, typically based on current injection, makes it possible to achieve population inversion. In the case of a semiconductor laser, the active medium is made of semiconductor materials. In figure 2.1 the main components leading to emission are displayed. The laser cavity contains the

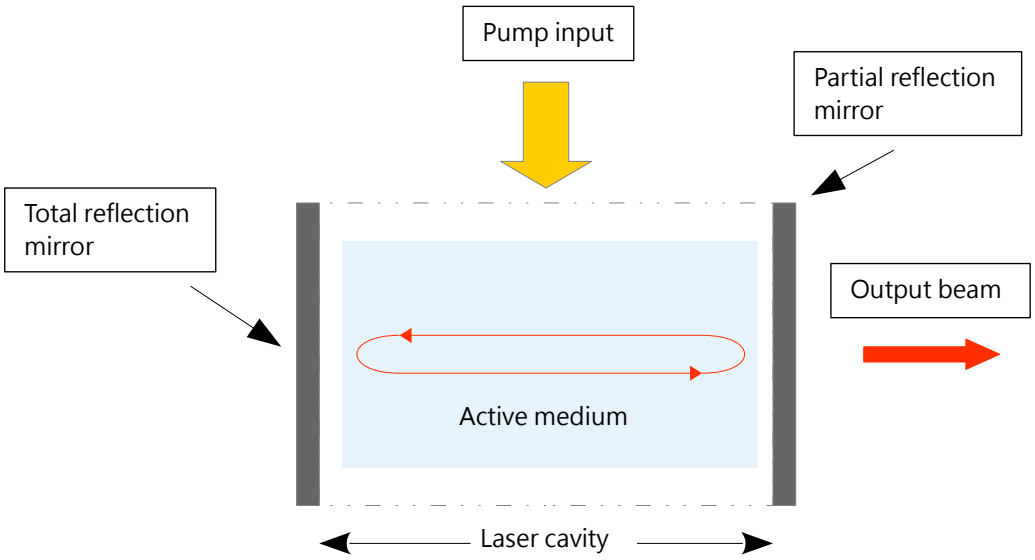

Figure 2.1: General scheme of a laser emission process.

active medium in which photons are generated and amplified thanks to the multiple reflections at the two mirrors, thus providing an optical feedback for photons whose frequency are allowed in the cavity. To achieve such result one of the two mirrors (with reflectivity labelled as r_1 and r_2) must have a very high reflectivity in order to make all the light back in the active medium, while the other must have a reflectivity less than 100% to have a transmitted beam.

The lasing itself starts when the gain plus the contribution from spontaneous emission (small amplitude with respect to stimulated emission) induced by the accumulated carriers in active material equals the cavity losses from the two mirrors.
The simpler active region structure is the *pin*-heterostructure, where an intrinsic low bandgap layer is sandwiched between a p- and n- doped semiconductor material with higher bandgap. In this way carriers are confined within the active region since smaller bandgap leads to higher refractive index.
Generally the resonance condition allowing the electric fields in the cavity to repeat after one round-trip is

$$\beta \cdot 2L = m \cdot 2\pi, \tag{2.1}$$

where β is the propagation constant of the electric field ,L is the cavity length, and m an integer.
Equation 2.1, considering that $\beta = 2\pi n_{eff}/\lambda_0$, states that not all the frequencies are permitted, and that the propagation depends on the effective index that the field experiences during the propagation.
As a consequence, structures as optical waveguides may be created alongside the plane of the active layer to have propagation of the confined wavelengths that satisfy the previous relation. In this scenario the dimensions of the waveguide may be chosen to support only the fundamental optical mode that may be TE (electric field parallel to the layers) or TM (electric field perpendicular to the layers) polarised. A laser with only one emission wavelength is said to be single mod, which is a characteristic of all studied VCSELs in this thesis.
Generally semiconductor lasers can be divided in edge emitting and surface emitting devices.
The basic edge emitter is the Fabry Pérot laser based on the previous description of the *pin* active region. The main characteristic is that the cavity is much longer than the vertical dimension perpendicular to the layers making the output beam with an elliptic cross section. The mirrors at the end are often wavelength independent thus making it easier to support multi-modes emission. To overcome this problem the mirrors may be replaced by gratings: distributed feed-back (DFB) laser in the case of grating within the active region, and distributed Bragg reflector(DBR) laser when placed at the end of the cavity. They are based on the alternation of low and high refractive index layers of semiconductor, leading to periodic variation of the mode index along the waveguide increasing the wavelength selectivity. At each pair the wave is partially reflected back, so by making the length of the layers equal to $\lambda/4$ it is possible to achieve constructively interference of the reflected wave and sustain the desired mode propagating at λ. In such a way, by using many pairs of layers one can achieve high reflection and a single mode output beam. Nonetheless the problem of the elliptic output still remains.

On the other hand, in the case of surface emitting laser the output beam shape can

be modified rather easily and made circular too. Moreover the device can be built by depositing one epitaxial layer on another and making it possible to test it through the process to ensure a correct outcome. Nonetheless it should be stated that edge emitting device are generally easier to integrate with other optical components such as modulator thanks to their waveguide like structure [4].
Nonetheless the surface emitting device that is analysed and treated in this thesis is the VCSEL where the mirrors are positioned below and above the active region. These types of device have a much lower length of the gain medium with respect to edge-emitting type thanks also to the fact that they can achieve a very high reflectivity with the superposition of many different layers ($> 99\%$).

2.2 VCSEL structure

Figure 2.2 shows the general structure of a VCSEL. On top we have a ring shaped p contact. While below we have the p-doped mesa, which refers to all layers (DBR and oxide apertures) up to the active region. The latter formed by several quantum wells. Below a n-doped mesa is present followed by the substrate and lastly a n-contact.
In the next part a in-depth description of each component is present. From now on the considered VCSEL are always 1060 nm single mode VCSEL, the propriety of being single mode is essential in order to measure the linewidth of the output beam.

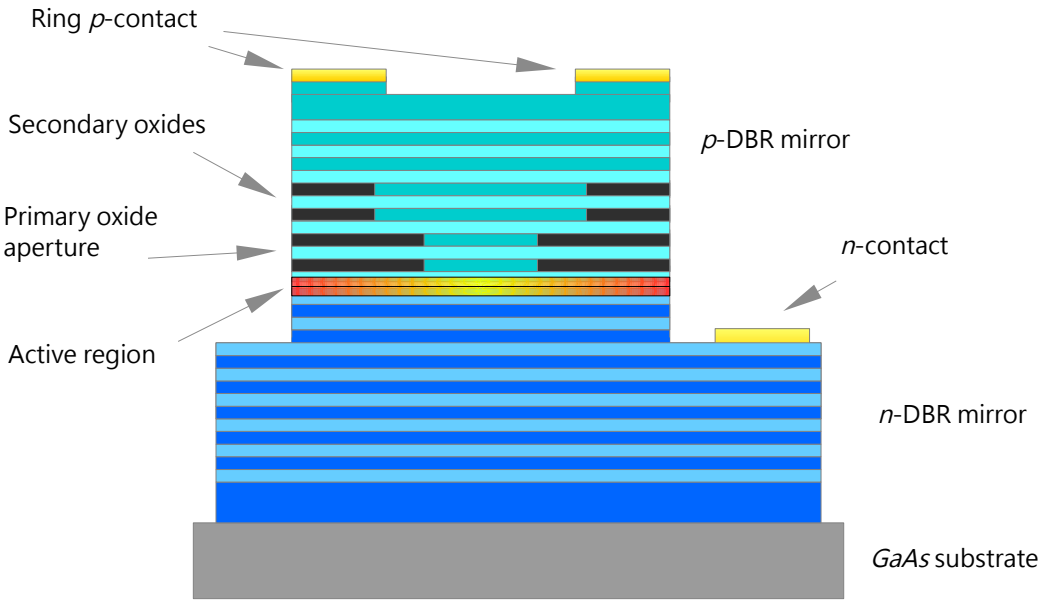

Figure 2.2: Schematic cross-section of an oxide-confined VCSEL.

2.2.1 Electrical Contacts

A ring shaped contact is a common choice for what regards top contact design of a VCSEL, in this way current may be injected almost uniformly within the structure and it

also decreases the coupling with the output light. Note that the ring contact should not be too large otherwise one would have non uniformity in the injected current and high order modes may be favoured. While a too small dimension would make the output light couple with the incoming current. The ring itself is then connected to the contacts pads where current is actually injected.
The bottom contact is used to collect the injected current that passed through the active region, thus acting as a ground.

2.2.2 Distributed Bragg Reflactors

The top and bottom DBR acts as a mirror for the VCSEL, as said before high reflectivity is needed due to thin layers of the active region. In this case the bottom DBR is constituted by first 24 pairs of AlAs/GaAs to reduce the thermal impedance, and the remaining are made of $Al_xGa_{1-x}As$/GaAs [10]. Here the concentration of Al varies through the layers of the top and bottom DBR in order to optimize reflections and decrease the resistance. The average doping level in the layers is decreased near the centre of the cavity where the optical field is high in order to decrease absorption loss from free carriers.

2.2.3 Oxide apertures

The oxide aperture acts as an electrical insulator reducing the actual area of the current from the top to the bottom contact. They are usually composed by $Al_xGa_{1-x}As$/GaAs with a very high concentration of Al; usually $x > 0.9$[10] , at these concentrations the band gap is very large ($E_g > 2Ev$), compared to GaAs ($1.412eV$) and also indirect. Its role is then to limit the actual current in the active region and to give the beam a more circular shape due to the change of refractive index induced by the insulator (the oxide has a lower refractive index with respect to the non-oxidized material), so also an optical confinement is present. The secondary oxides are implemented in order to reduce the capacitance due to charge accumulation near the primary oxides, thus improving the speed of the device. An important aspect is the distance between the first primary oxide and the active region. In fact the more distant they are the higher will be the dispersion of the mode and so less guided. As a last remark it should be noted that the DBRs introduce what is called as frequency detuning. In other words the Active region of the VCSEL may have its operating wavelength at 1045nm. Then the DBR action shift this frequencies up to approximately 1060 nm which is the actual VCSEL output wavelength. This concept is important since the DBR are not treated in this thesis , thus the aimed operating wavelength must be less than 1060 nm to account for that detuning.

2.2.4 Substrate

The substrate is made of GaAs and represent the base upon which the whole device is grown. It has to be GaAs in order to be lattice matched with the DBR above made of AlGaAs to avoid premature cracks and dislocations.

2.2.5 Anti-phase and Surface relief

From figure 1.1 it is possible to see that the last layer is not uniform. This technique is called Inverted surface relief [2]. The method can be divided in two main steps. First, the last layer is made thicker by a quarter wavelength, in this way the total mirror losses increase. In particular an extra $\frac{\lambda}{4}$thick GaAs layer is added to the top DBR to allow for fine adjustment of photon lifetime. This design is called anti-phase design. With this construction the optimization of the oxide apertures is easier together with a better etch depth control [3].

Then the top DBR anti-phase layer in the centre of the VCSEL part is etched leading to high top reflectivity and low mirror losses at the surface, this technique is called Surface relief or mode filtering.
As a consequence the fundamental mode, which has the largest overlap in the centred low loss region, experiences less losses. While the other modes will be higher suppressed due to the lateral increased mirror losses.

2.2.6 Active region

The active region has several quantum wells(QW).They make us of the injected currents from the contacts to create population inversion and then by stimulated emission to generate photons in the region. In our specific case we have three InGaAs/GaAsP QWs, the P in GaAsP is used to give partial strain compensation to the structure since InGaAs is not lattice matched to the substrate.
This region is by fare the most important since the dimensions of the QWs, their composition and distance between each other will determine the lasing wavelength of the cavity. The following chapters are all centred around the physics of the quantum wells that build the structure, in order to reach quantities such as the gain, spontaneous emission, and so the theoretical linewidth.

2.3 Linewidth

In this last section a brief review on the theory behind the used linewidth expression is presented. The reader is referred to [5] for a complete derivation.
The starting point for a complete description of the processes related to the active region

carriers generation is given by the so called rate equations.

$$V\frac{dN}{dt} = \frac{\eta_i I}{q} - (R_{sp} + R_{nr})V - (R_{21} - R_{12})V \tag{2.2}$$

$$V_p\frac{dN_p}{dt} = (R_{21} + R_{12})V - \frac{N_p V_p}{\tau_p} + R'_{sp}V. \tag{2.3}$$

Here each term is related to a decrease and increase of carrier and photon densities, figure 2.3 shows the contribution of all th terms to the overall outputs. V and V_p are respectively the volume of the carriers and photons reservoir.

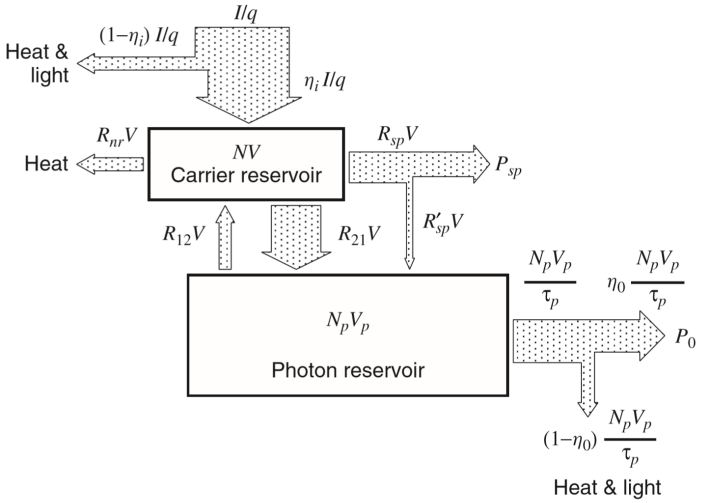

Figure 2.3: Different contributions to rate equation, figure from [5].

- Starting from the input current I, the density of injected carriers is given by $\frac{\eta_i I}{q}$ where η_i is the internal efficiency representing how many of the electrons actually contributes to the overall electrons density in the reservoir. $1 - \eta_i$ thus is the lost electrons that contribute to heating and unwanted light emission.

- R_{nr} is the loss of electrons by non-radiative recombination. Thus this contributes to the heating of the system.

- R_{sp} is the total spontaneous emission rate which related to the emitted photons from the active region.

- R'_{sp} is the single mode spontaneous emission, or in a more general way the spontaneous emission related to the lasing frequency. It contributes to increasing the photon reservoir since the emitted photons satisfy the round trip condition, while all the other are emitted at other frequencies.

- R_{12} is associated to stimulated absorption. Electrons are promoted to the CB (conduction band) thanks to the incoming energy from the photons reservoir. As a result the carrier density increases while N_p decreases.

- R_{21} corresponds to stimulated emission. Here the process is the inverse of before: Electrons from the carrier densities lose energy and fall to the VB (valance band) after the influence of the incoming photon from the photons reservoir. Then the carrier density decreases and N_p increases.

- Lastly $\frac{N_p V_p}{\tau_p}$ represents the output photons exciting the active region and forming the actual output of the laser. Again not all of them are emitted, but a part is absorbed contributing to heat and other processes such as scattering, η_0 is the optical efficiency defining such losses. τ_p is the photon lifetime in the cavity.

The rate equations can be re-written in a better form by using the formula for R_{21},R_{12} and introducing $\Gamma = \frac{V}{V_p}$ which is the confinement factor of the field within the active region.

$$\frac{dN}{dt} = \frac{\eta_i I}{Vq} - (R_{sp} + R_{nr}) - v_g G N_p \tag{2.4}$$

$$\frac{dN_p}{dt} = \left(\Gamma v_g G - \frac{1}{\tau_p}\right) N_p + R'_{sp}\Gamma \tag{2.5}$$

The linewidth is defined as the width (typically the full width at half-maximum, FWHM) of its optical spectrum. A finite linewidth comes from phase noise (random fluctuations in the phase of a waveform in the frequency domain), which can be associated to different causes. Quantum noise, in particular spontaneous emission of the gain medium into the resonator modes, but also quantum noise associated with optical losses. Moreover the noise due to vibrations of the cavity mirrors or to temperature fluctuations may be present too. In this thesis two basic sources are supposed to give contribution to the phase noise: spontaneous emission and carrier density variations. The first is present in all lasers, resulting simply from the random addition of spontaneously emitted photons to the quasi-coherent resonant cavity mode. The second is of importance only in diode lasers, and it results from the proportionality between $\Delta\nu$ and ΔN, namely

$$\Delta\nu = -\frac{4\pi}{\lambda G_{dif}} \frac{dn_r}{dN} \tag{2.6}$$

with n_r being the real part of the complex, α the linewidth enhancement factor, and G_{dif} the differential gain. The previous equation states how the variation of carrier density is reflected on a frequency change, said frequency chirping. It contains the linewidth enhancement factor, α, which derives from the fact that both the gain and the refractive index depend directly on the carrier density.

Spontaneous emission

Having said this, the spontaneous emission term can be easily obtained by considering rate equations. By assuming no stimulated effects eq. 2.5 can be solved giving an exponential

decreasing carrier density. In analogy with that, the time dependent field in the cavity is expressed as

$$\mathcal{E}(t) = E_0 e^{j\omega_0 t} e^{-\frac{t}{2tau'}}. \tag{2.7}$$

To get $\Delta\nu$,the Fourier transform of the previous equation is computed. Re-introducing the stimulated terms, an analogue expression is obtained by fixing

$$\frac{1}{\tau_p'} = \frac{1}{\tau_p} - \Gamma v_g G, \tag{2.8}$$

which is the effective carrier lifetime. Then the FWHM (full width half modulation) gives the value of the linewidth of the field to be

$$\Delta\nu_{ST} = \frac{1}{2\pi\tau_p} = \frac{\Gamma R_{sp}'}{2\pi N_p}, \tag{2.9}$$

where the solution of eq. 2.5 in the steady state case ($\frac{dN_p}{dt} = 0$) was used.

$$N_p = \frac{\Gamma R_{sp}'}{\frac{1}{\tau_p} - \Gamma v_g G} \tag{2.10}$$

With

$$R_{sp}' = \frac{\Gamma v_g G_{th} n_{sp}}{V}, \tag{2.11}$$

and G_{th} being the gain at threshold. Eq. 2.9 is called Schawlow Townes linewidth formula. I is important to notice that the linewidth decreases with increasing photon density. In other words it is inversely proportional to the output field. In fact it holds that

$$N_p = \frac{P_o}{\hbar\nu v_g \alpha_m} \tag{2.12}$$

with $v_g\alpha_m = \tau_m^{-1}$ defining the energy loss through mirrors. This particular value, together with Γ are obtained from VELM simulations of the real structures of the devices.
Equation 2.9 needs to be divided by a factor 2 in order to take into account the non linear coupling arising between the two rate equations when above the threshold, doing this leads to the so called modified Schawlow Townes linewidth formula.

Carrier noise

The latter, however, still only considers spontaneous emission noise and does not include carrier noise, eq. 2.6. To describe such effect, the Langevin sources noises for carrier and photon densities are introduced in the differential rate equations, see [5]. Later as done in the simple case, going to the frequency domain grants the writing of the carrier $S_N(\omega)$ and photon $S_{N_p}(\omega)$ spectral density. The frequency noise spectral density is then calculated as

$$S_\nu(\omega) = \frac{1}{2\pi}(\Delta\nu_{ST})(1 + \alpha^2|H(\omega)|^2), \tag{2.13}$$

with $H(\omega)$ being the modulation transfer function. Which is usually used in electronics to identify the quality of a device response over frequencies. Eq. 2.13 already gives the complete linewidth of a laser. Nonetheless in its form it is not practically usable.
To overcome this, the coherence time τ_{coh} is introduced to define the combination of the propagating field with itself, leading to the autocorrelation function

$$\mathcal{E}(t)\mathcal{E}(t-\tau)^* \propto e^{j\omega\tau - \frac{-|\tau|}{\tau_{coh}}}. \tag{2.14}$$

If in phase the two fields gives the expected interference pattern related to the term $e^{j\omega\tau}$, but after some time delay tau, they are not correlated any more and add incoherently. Assuming a constant coherence time[1] the Fourier transform of eq. 2.14 gives a Lorentzian profile[2]. Doing so allow to relate the coherence time with the noise spectral density as

$$\frac{1}{\tau_{coh}} = \pi\tau \int_{-\infty}^{+\infty} S_\nu(\omega) \frac{sin^2(\frac{\omega\tau}{2})}{\left(\frac{\omega\tau}{2}\right)^2} d\omega, \tag{2.15}$$

where the integrated function $\frac{sin^2(\frac{\omega\tau}{2})}{\left(\frac{\omega\tau}{2}\right)^2}$ is the $sinc^2$ function of $\frac{\omega\tau}{2}$. For high delay times the oscillation of sinc function becomes very low and negligible and it is possible to approximate it to $S_\nu(0)$. In other words, the high contribution comes from the peak of the sinc function which is located at low frequency values, at higher values the result is very close to zero thus making the right side of eq. 2.15 zero. Doing this makes it possible to move out of the integral S_ν and solve the integral of a $sinc^2$ function which is equal to $\frac{2\pi}{\tau}$. The final result is then

$$\Delta\nu = \frac{1}{\pi\tau_{coh}} = 2\pi S_\nu(0), \tag{2.16}$$

using eq.2.13 and the fact that at zero frequency the modulation transfer function is 1 we get to the well known formula for the laser linewidth

$$\Delta\nu = \frac{\Gamma R'_{sp}}{2\pi N_p}(1+\alpha^2). \tag{2.17}$$

Conclusion

In this thesis what is compared to the experiment is not the linewidth obtained from the previous equation. Instead the normalized linewidth with respect to the power is computed. Such compress is due to the fact that the QW gain model used does not compute the optical power, rather that is accomplished using VENUS entirely.
In addition to that it is of great importance to remark the fact that by computing the spontaneous emission rate with a much more complex model with respect of the one

[1] It may be that $\tau_{coh}(\tau)$, however here this dependence is neglected. Indeed from experimental measurements a difference in the linewidth measured over time (with the same set-up) is minimal, so this assumption is allowed

[2] This concept is crucial since the fitting of the experimental curves is done relating it to a Lorentzian curve.

contained in [5], the unit of measurement is s^{-1}. Thus 2.11 is not used. The used expression is then

$$\Delta\nu_{cof} = \frac{\Gamma E_s}{4\pi\tau_m\hbar\frac{c}{\lambda_{peak}}2\pi}(1+\alpha^2), \tag{2.18}$$

where E_s and α obtained theoretically in the following chapters. As a result also the gain and refractive index variation of the active region are calculated in order to compute the linewidth enhancement factor. On the other hand λ_{peak} refers to the experimental wavelength of the emission peak of the measured VCSELs at Chalmers.
Then to chose the most suitable value for E_s and α, a suitable threshold gain is used as a consequence of VELM simulations of the total optical spectrum.
In the next chapters the aforementioned needed quantities are calculated.

Chapter 3

InGaAs/GaAsP Quantum well

In order to reach emission at 1060 nm the VCSEL active region has been changed in the past from InGaAs/GaAs to the present version by the addition of phosphorus[10]. This change was possible due to the nature of alloy semiconductor which provide different degree of freedom considering the alloy composition and what elements are used.
Indeed the physical reason will be understood later on, but to give a qualitative explanation, the addition of P makes the barrier material undergo a tensile stress. As a consequence the gap decreases and so the total strain to the structure is partially or totally compensated. Moreover by having strain compensation, the probability of having cracks in the device decrease due to a lower net total strain.
From now on the used notation for the doping is $In_{(1-x)}Ga_xAs/GaAs_yP_{(1-y)}$ where x and y, which can go from 0 to 1, denote the fraction of respectively gallium and arsenide. To change to one notation to another one can simply substitute x with $1-x$ and y with $1-y$.

An important remark should be made about the band gap, E_g, of the two alloys. They play a huge role in the lasing frequency as explained before. Regarding the barrier material , GaAsP, after the concentration of P becomes larger than 0.45[15], the band gap of the alloy changes from direct to indirect. As a consequence all the parameters and properties are different. In the present case the concentration of P will be always lower than the upper limit.
Lastly in this thesis the flat band approximation used, i. e the bands from the well to the barrier exhibits a jumps in energy rather than a continuous conduction/ valance band.

3.1 Strain

Strain is the measure of how much an object is stretched or deformed, in its general definition it may be defined as

$$strain = \frac{\Delta L}{L}, \tag{3.1}$$

with L being the original length of the object.
In complex scenario it is rather difficult to have simple equation for the strain, since a tensor related to x, y, z, direction has to be used and it usually contains many different components. However in the case of a quantum well a simple definition can be found by assuming that the growth of material with lattice constant a on the substrate with reference lattice constant a_0 is performed along the [001] direction of the (001) crystallographic plane[11],[12],[13]

$$\epsilon = \frac{a_0 - a_1}{a_1}. \tag{3.2}$$

ϵ is the strain related to the mismatch in lattice constants between the two materials. Depending on its sign the strain will be tensile ($\epsilon > 0$) or compressive ($\epsilon < 0$). This approximation is good as soon as the used substrated and structure are GaAs-based.
In the present analysis we will always consider the substrate to be GaAs for both the well and the barrier. On the other hand the lattice constants of both $\mathrm{In}_{(1-x)}\mathrm{Ga}_x\mathrm{As}$ and $\mathrm{GaAs}_y\mathrm{P}_{(1-y)}$ will depend on the concentration x and y. Thus for a fixed concentration the strain will be different in the quantum well. The two value of lattice constants are obtained from the general expression of the lattice constant of the quaternary alloy $\mathrm{In}_{1-x}\mathrm{Ga}_x\mathrm{As}_y\mathrm{P}_{1-y}$[14]

$$a \approx 5.8688 - 0.4176x + 0.1896y + 0.0125xy \tag{3.3}$$

all measured in ångström [Å]. By putting $y = 1$ one has $\mathrm{In}_{(1-x)}\mathrm{Ga}_x\mathrm{As}$, and with $x = 1$ $\mathrm{GaAs}_y\mathrm{P}_{(1-y)}$. The two quantities are displayed in figure 3.1. In the case of InGaAs we

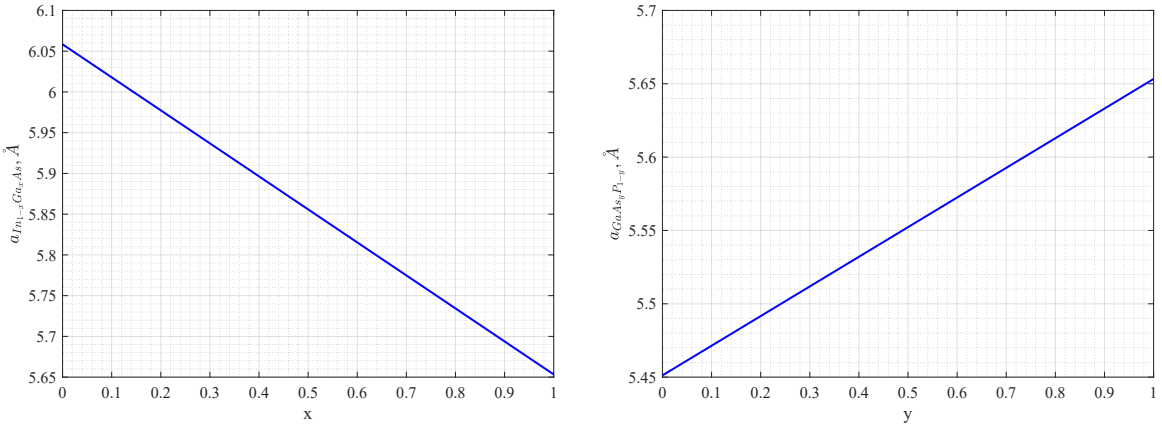

(a) $In_{1-x}Ga_xAs$ (b) $GaAs_yP_{1-y}$

Figure 3.1: Lattice constants of the QW materials vs composition.

clearly see that no matter what is the concentration of In, the lattice constant is always larger than the the one of the substrate $a_0 = 5.65325\mathring{A}$. Thus every layer of that material will always suffer a compression if deposited on GaAs.
At the same time GaAsP has a smaller lattice constant and so will experience a tensile

stress.
To reach a perfect balanced structure we should have the total strain equal, in other words we should satisfy[12]

$$t_w\epsilon_w + t_b\epsilon_b = 0, \tag{3.4}$$

with t_i being the thickness of the well and barrier. Indeed as we expect the longer is the layer, the lower is the effect of strain compared to a shorter one. To avoid defects and dislocation the total net strain should be lower than a e certain threshold. Complex models [16] should be used to get an accurate estimation for the value. Nonetheless we could get a very simple limit value by using eq. 3.4 and ensuring that the sum does not exceed $10^{-3}/nm$[17]. A suitable choice for the thickness of well and barrier is in the order of nm. While x goes from 0 to 1, y takes discretized values up to 0.6 to avoid indirect transition in the barrier band gap. Figure 3.2 shows the solutions of eq. 3.4 by using $t_w = [5, 20]nm$ and $t_w = [9, 40]nm$. The thickness of the barrier is chosen higher since its role is to isolate the well. The larger it is the better the larger its contribution will be on the total strain. In the plot we see that with increasing As concentration the allowed solutions decrease, in fact by making the GaAsP close to GaAS we reach lattice matching and thus no strain. For this reason at the maximum case where y is very close to the maximum value, the set of allowed solutions along x is very close to 1, meaning that also InGaAs goes down to GaAs. The result is a plane of solutions, since we have $\epsilon_b \approx \epsilon_w \approx 0$ all the possible values of well and barrier thickness's are solutions.
Moreover it is clear that a low y (a) makes it possible to counter act higher In composition in InGaAs due to the fact that solutions starts from $x \propto 0.6$.
Note that in general InGaAs gives an higher maximum absolute strain, in fact $\epsilon_{w,x=0} \approx -0.06$ while for GaAsP $\epsilon_{b,y=0} \approx 0.037$. This justify the non direct matching between x and y in the solutions.

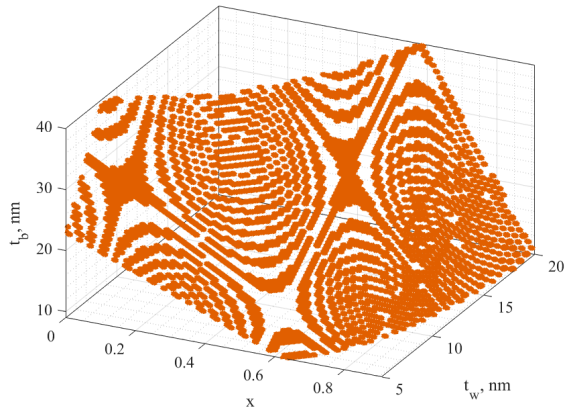

(a) $y = 0.6$

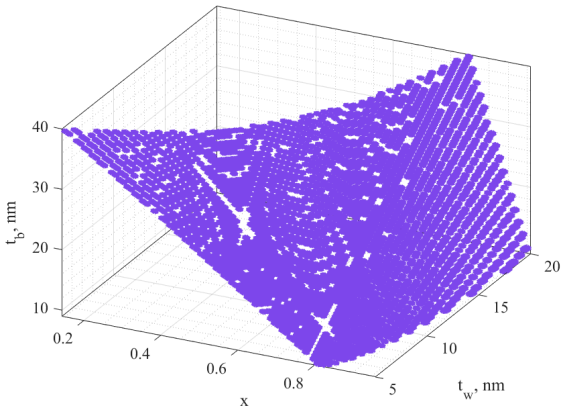

(b) $y = 0.8$

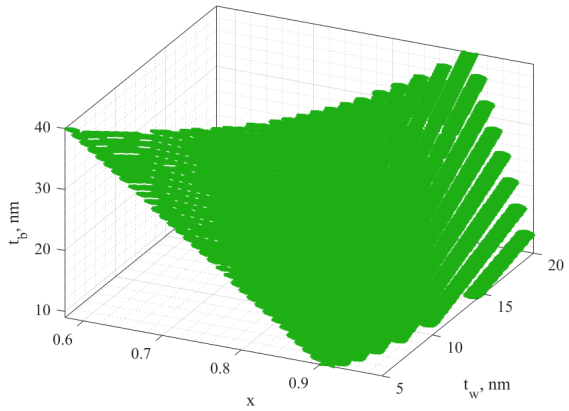

(c) $y = 0.9$

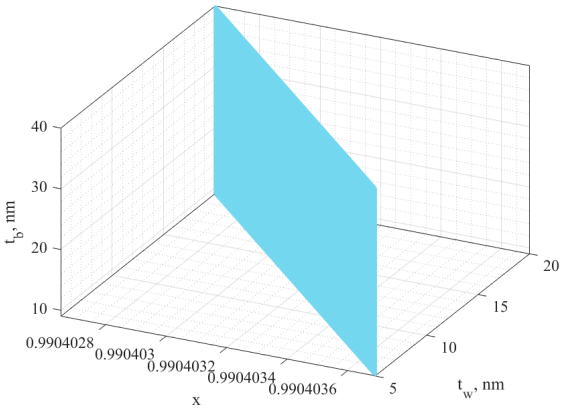

(d) $y \approx 1$

Figure 3.2: Surface of the solutions for different values of y.

3.2 Strain models

Usually a good description of the system starts with the definition of the band diagram. Since we are dealing with a strained quantum well, the conduction and valance band energies undergo a modification proportional to the amount of strain. From them it is possible to retrieve the so called band offset, which represent the difference between the final valance/conduction band of the well and barrier respectively that are needed not only for the $\boldsymbol{k} \cdot \boldsymbol{p}$ method and to construct the band diagram of the QW, but also in the other component of VENUS such as the drift diffusion solver. It usually depends on the composition of the the well and barrier together width the amount of strain in each part. More precisely it is defined as

$$\begin{aligned} \Delta E_c &= E_c^b - E_c^w \\ \Delta E_v &= E_v^w - E_v^b. \end{aligned} \tag{3.5}$$

Here the superscripts b and w correspond respectively to the barrier and well materials. To have them always positive we define the band offset of the conduction band as the difference of the higher conduction band which belongs to the barrier with the lower one of the well. while in the case of the valance band is the opposite. This concept is immediate since by definition a Quantum well requires the barrier material to have larger band gap in order to have carrier confinement in the well.
Lastly, the conduction band offset defined as

$$Q_c = \frac{\Delta E_c}{\Delta E_c + \Delta E_v} \tag{3.6}$$

is another important quantity, since it can be measured experimentally and so assure the out-coming of the model [13]. In this simplified scenario, the strain has only three non zero components: ϵ_{xx}, ϵ_{yy}, and ϵ_{zz}. Moreover we have that $\epsilon = \epsilon_{xx} = \epsilon_{yy}$ and

$$\epsilon_{zz} = -2\frac{C_{12}}{C_{11}}\epsilon. \tag{3.7}$$

where C_{12} and $C_{11}$are the elastic stiffness constants. So we see ϵ is the only quantity required to evaluate all the strain terms and so also the related effects on the bands by using the proper constants.
The new conduction and valance energies can be computed with two different models: The model solid theory and Harrison model [13],[18],[19], [20],[22]. The need of theoretical model is explained from the fact that experimental values for the band offsets often do not exist in the literature, or they may not cover the precise composition of the alloy.

3.2.1 Model solid theory

The principal feature of the model-solid theory consists in relating the average electrostatic potential of the to the vacuum level. This puts all calculated energies on an absolute

energy scale, and allows us to derive band lineups by simply subtracting values for each individual semiconductor of the QW. The common reference is accomplished by modelling the solid as a superposition of neutral atoms. In each atom, the electrostatic potential is rigorously defined with respect to the vacuum level. This average is introduced as a consequence of the splitting of the valence bands will due to shear strains and eventually spin-orbit splitting[19]. They can be expressed in formulas that refer the individual bands to the average.

So the starting point is to determine the position of $E_{v,av}$. Thus the different splitting listed before are in this way averaged out. When considering the effect of the strain, two contributions occur in the calculation. The first one comprehends the effect on the band structure when the solid is compressed: the bands shift with respect to the average potential in the solid. Secondly, the average electrostatic potential itself is shifted due to the hydrostatic component of the strain, which it is inversely proportional to the volume. The value used in this description are obtained from *ab initio* simulation and experimental validation.

As we expect the strain will act differently on heavy E_{hh} and light hole E_{lh} energies. In addition, we may also see no more degeneracy in these bands. The two quantities change in accord with

$$E_{hh} = E_{av} + E_{hv} - \frac{E_t}{2} + \frac{\Delta}{3}, \tag{3.8}$$

for what regards the heavy hole and

$$E_{lh} = E_{av} + E_{hv} + \frac{Et}{4} - \frac{\Delta}{6} + \sqrt{\Delta^2 + \Delta E_t + \frac{9}{4}E_t^2} \tag{3.9}$$

for light holes.

Here Δ is the spin orbit coupling energy. E_{hv} the contribution of the hydrostatic perturbation energy and E_t the tetragonal distortion energy[3]. They are defined as

$$\begin{aligned} E_{hv} &= a_v(\epsilon_{xx} + \epsilon_{yy} + \epsilon_{zz}) = 2a_v\left(1 - \frac{C_{12}}{C_{11}}\right)\epsilon \\ E_t &= -b(\epsilon_{xx} + \epsilon_{yy} - 2\epsilon_{zz}) = -2b\left(1 + 2\frac{C_{12}}{C_{11}}\right)\epsilon, \end{aligned} \tag{3.10}$$

where eq. 3.7 was used.

Lastly the strained conduction band is written as

$$\begin{aligned} E_c &= E_{av} + E_g + E_{hc} + \frac{\Delta}{3} \\ E_{hc} &= a_c(\epsilon_{xx} + \epsilon_{yy} + \epsilon_{zz}) = 2a_c\left(1 - \frac{C_{12}}{C_{11}}\right)\epsilon, \end{aligned} \tag{3.11}$$

[3]Here the terminology used is the one from [13], which however presents an error (here corrected) in the equation for E_{hh} by comparing it with [19] and [20]. The chosen notation is easier to use with respect to the other.

with E_g being the unstrained gap of the considered part of the QW and E_hc the hydrostatic deformation potential.a_c, a_v, b, C_{12}, and C_{11} are constants within the model that depends on the chosen material for the QW.

Figure 3.3 shows the conduction band offset for $In_{(1-x)}Ga_xAs$ with x varying from 0.5 to 1. We note that with increasing Ga concentration, and so decreasing In the ratio increases meaning that the effect of the strain on the valance band is lowers with respect to the valence band. Thus we expect to have a band diagram where the higher variations are reflected in the CB.

With increasing P concentration in the barrier (and so decreasing y) we see an overall shift of the assumed curve towards higher values. This means that the barrier strain as an important role on both the conduction and valance bands of the well, moreover its impact is is always larger in the CB.

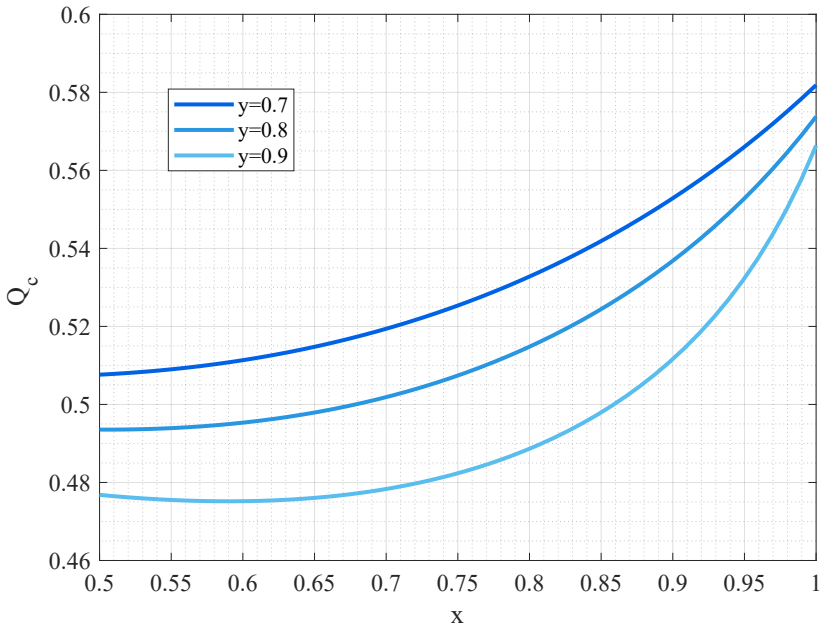

Figure 3.3: Qc for the QW with different concentration of Ga in $In_{(1-x)}Ga_xAs$, for three values of y; namely $GaAs_{0.7}P_{0.3}$, $GaAs_{0.8}P_{0.2}$, and $GaAs_{0.9}P_{0.1}$. The used constants are labelled in table 3.1 and 3.2

3.2.2 Harrison model

In the Harrison model the unstrained conduction and valance band are directly used. Thus we have for the valance band

$$\begin{aligned} E_{hh} &= E_v^0 + E_{hv} - \frac{E_t}{2} \\ E_{lh} &= E_v^0 + E_{hv} + \frac{E_t}{2}. \end{aligned} \tag{3.12}$$

While for conduction band

$$E_c = E_c^0 + E_{hc}. \tag{3.13}$$

All the used terms are the same of the Model Solid theory. Indeed by comparing the two models we see that the strain is included in the same way for the heavy hole and conduction band case. What changes is the inclusion of the spin orbit coupling energy and the absence of the average energy used as a reference.
Figure 3.4 shows a comparison between the Model Solid Theory and the Harrison model by looking at Q_c. For the barrier material the real used concentration was used.
We note that there is approximately a 9% difference up to $x \approx 0.8$, this difference impacts the QW in such a away that we may have, in the final structure, some energy levels confined when there should be none. For this reason the choice of the right model represents a key point.
Apart from this, a cross between the two curves happens close to the case of $InGaAs$ becoming $GaAs$. This point is of no interest to us since the used concentration of In for the well are higher.

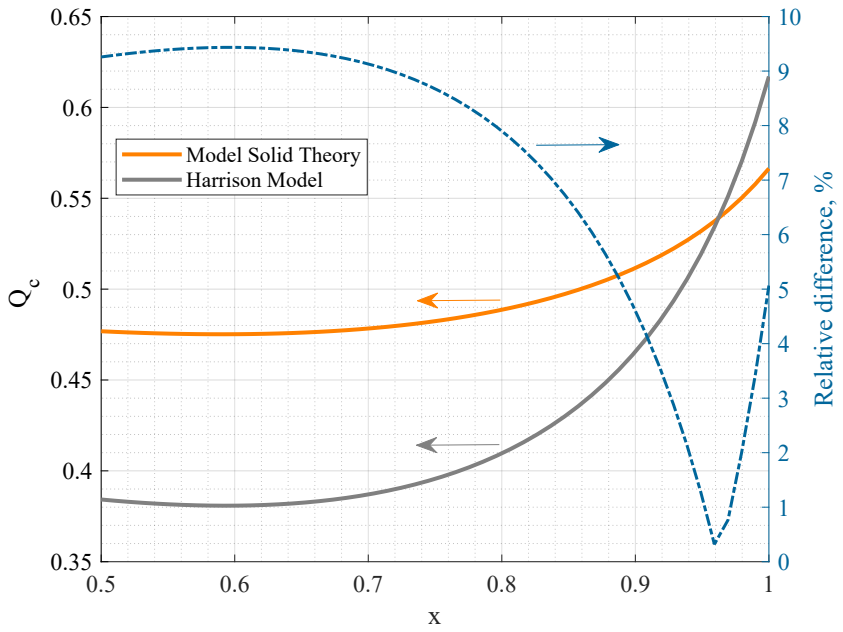

Figure 3.4: Qc (left axis) and relative difference(right) for $In_{(1-x)}Ga_xAs/GaAs_{0.9}P_{0.1}$ considering the Model Solid Theory and Harrison Model. The used constants are labelled in table 3.1 and 3.2

3.3 Band Diagram

The chosen model for the band diagram is the model solid theory in accord with [13] and [22]. Moreover the Harrison model cannot be used to retrieve the new band gap of the

material by performing the difference between the conduction and valance band [20]. It can only be used to retrieve the band discontinues, eq.3.5.
Since the involved semiconductors are ternary alloy, the parameter of the binary compounds are interpolated using

$$K(AB_xC_{1-x}) = xK(AB) + (1-x)K(AC) - x(1-x)b_{ABC}, \tag{3.14}$$

where K is a generic quantity of the alloy. Here b_{ABC} is the bowing parameter used to better describe the interpolation when the linear one is not good enough. Instead for the well and barrier the used expression for the gaps are not obtained with 3.14, but with the experimental composition dependent expression are used, namely [14]

$$\begin{aligned} E_{g,w} &= 0.36 + 0.629x + 0.426x^2 \\ E_{g,b} &= 2.776 - 1.469x + 0.108x^2, \end{aligned} \tag{3.15}$$

Then using equation 3.8,3.9, and 3.11 the new conduction and valance bands can be obtained. Table 3.1 contains the used constants [22] for the simulation for the compounds forming the QW: $GaAs$, $InAs$, and GaP.

Table 3.1: Model solid theory constants

Symbol	Parameter	$GaAs$	$InAs$	GaP
a_c, eV	Hydrostatic deformation potential (CB)	-7.17	-5.08	-7.14
a_v, eV	Hydrostatic deformation potential (VB)	1.16	1	1.7
b, eV	Shear deformation potential	-1.7	-1.8	-1.8
$C_{12}, \frac{dyn}{cm^2}$	Elastic stiffness constant	$5.376 \cdot 10^{11}$	$4.526 \cdot 10^{11}$	$6.203 \cdot 10^{11}$
$C_{11}, \frac{dyn}{cm^2}$	Elastic stiffness constant	$11.879 \cdot 10^{11}$	$8.329 \cdot 10^{11}$	$14.05 \cdot 10^{11}$
Δ, eV	Spin orbit coupling	0.34	0.38	0.08

While the bowing parameters are summarised in Table 3.2 [13], here we note that in the case of GaAsP the correction is zero except for the band gap.

Table 3.2: Bowing parameter constants

Material	b_{E_g}	b_{E_p}	b_Δ	b_{a_c}	b_{m_e}	b_{m_h}
$In_{(1-x)}Ga_xAs$	0.477	1.48	0.15	2.61	0.0091	0.145
$GaAs_yP_{(1-y)}$	0.19	-	-	-	-	-

Lastly the used x and y, together with the Quantum well dimensions are listed in 3.3.

These parameters are the most important, especially the concentration of Ga and In. In fact many properties, among which the peak emission wavelength heavily depends on such values. The length of the well and barrier are labelled L_w and L_b respectively. In this thesis the values are accurately selected to better compare the theory with the experiment[4]

Table 3.3: Quantum well parameters

Material	x	y	*Length*
$In_{(1-x)}Ga_xAs$	0.68	–	$6nm$
$GaAs_yP_{(1-y)}$	–	0.9	$17nm$

Figure 3.5 contains the unstrained band diagram (a) (by allowing $\epsilon = 0$) and the strained one (b). It is clear that the difference in lattice constants leads to a non negligible strain in the system. Here the conduction band is shown in blue and the valance band in red.

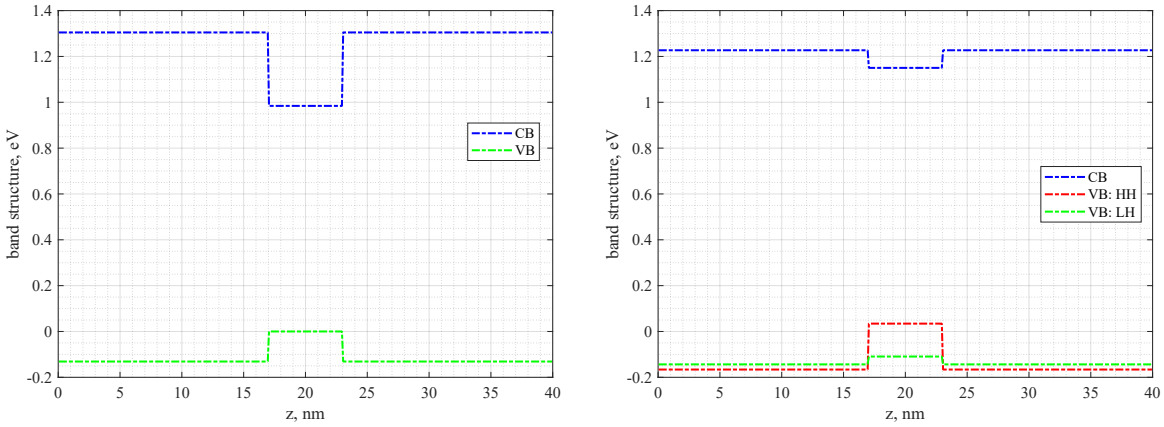

(a) $\epsilon_b = \epsilon_w = 0$ (b) $\epsilon_b = 0.0035, \epsilon_w = -0.022$

Figure 3.5: Single QW band diagram of the active region.

Upon strain application, the CB in the well becomes higher as a result of the compression. While the barrier CB decreases due to the enlargement of the lattice constant with respect tot he substrate as explained before. Nonetheless it is possible to notice the splitting in the Valance band due to the different effect of the strain as depicted also in eq. 3.9 and 3.8, nonetheless the true reason for this splitting will be understood in the next chapter. In fact another contribution is present here apart from the one of the model solid theory.

[4]From the specifications of the tested VCSEL at Chalmers, the value of y was the same as the one implemented here but x was higher. Indeed it is true that the peak of emission is adjusted by proper deposition through the fabrication, so the true composition sometimes is not specified. Knowing this our approach can be justified.

This is necessary in order to get a complete description of the system especially to link the aforementioned model with the **k·p** method.
By setting the reference for the energies to the unstrained VB, we note how in our case the HH VB is higher than zero. This means that we may find sub-bands between this value and $E = 0eV$, leading to an actual decrease of the true band gap.
To conclude figure 3.6, shows the band diagram in the real case of three QW, the external barrier thickness i chosen to be $30nm$, higher with respect to the internal one in order to isolate the active region. This geometry is introduced here since the **k·p** method will give some different results with respect to 1QW worthy to be discussed. Moreover in principle one should always use the true active region for the dimension, but this can be neglected by proper assumptions.

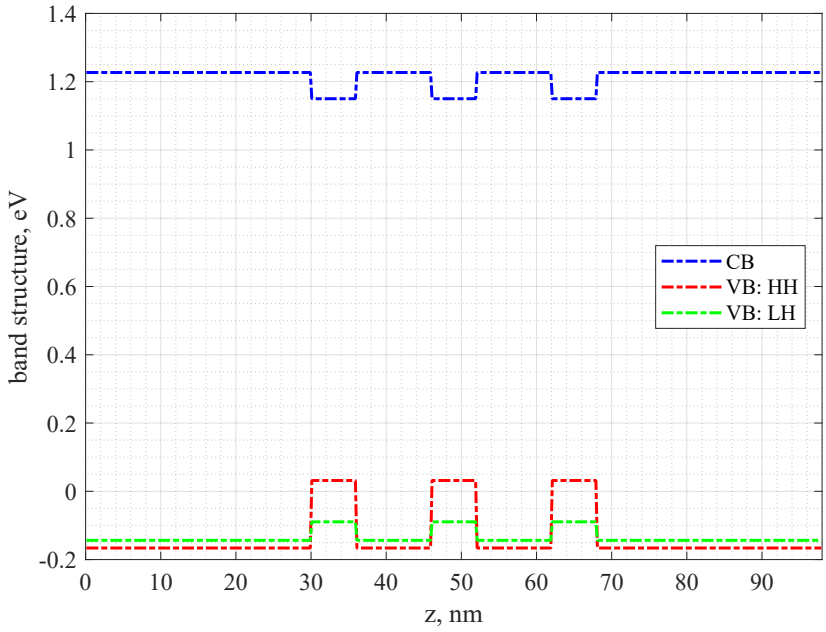

Figure 3.6: Three QW Band diagram of the active region.

Chapter 4

$\mathbf{k}\cdot\mathbf{p}$ method

4.1 Introduction

The optical properties of nano-structures are connected to the electronic states, such as the response of electrons within the atomic lattice to external perturbations that could be, as in our case, an external pump of electrons in the active region to turn on the VCSEL. It is clear that a precise knowledge of the electronic properties is required for a proper device analysis. In bulk semiconductors, the lattice periodicity and its symmetry leads to the formation of continuous electronic bands associating the crystal momentum k of an electron to its energy $E_n(k)$. However the introduction and combination of different materials within a nano-structure breaks the symmetry of the semiconductor crystal, leading to quantization effect, and so to the modifications of the electronic properties from their bulk properties. Thus the optical and electronic properties of the structures will be hugely affected: Gap re normalization, emission wavelength due to temperature shift, dipole momentum, sub-bands generation are among the different physical effect related to the nano-structured work. On top of that also the strain introduced in the previous chapter plays an important role in the description.
In this thesis the method to solve the Schrödinger equation and retrieve the band structure and energy in the QW is the famous $k \cdot p$ method [21],[22], [23].
The band structure near high-symmetry points (Γ, X, L) is solved through the perturbation theory, in other words the materials made by the heterostructures are threaten as a weak perturbation of a reference crystal. The output information is accurate enough[24] to be used for simulating optoelectronic processes near the semiconductor band gap. Here an 8x8 Hamiltonian is derived following Kane notation[26] which has been heavily explained in[21]. Then the obtained Hamiltonian is transformed to the notation used in [24] in order to implement the axial approximations and include strain effects. The discussion starts with a simple case of bulk material and then the actual structure is considered to give a general overview on the method upon which the main theoretical part of the thesis is based on.

4.2 Bulk case

We start the analysis from the simpler structure made of an homogeneous bulk case [21]. Eq. 4.1 represents the Schroedinger equation to be solved in order to obtain the allowed energy levels in the system under the form of eigenvalue electron[5] in the structure.

$$\left(-\frac{\hbar^2}{2m_0}\nabla^2 + U(\boldsymbol{x})\right)\psi = E\psi. \tag{4.1}$$

Here U is the potential energy acting on the electrons, while ψ is the wave function associated to the electron. It can be written as

$$\psi_{n\boldsymbol{k}}(\boldsymbol{x}) = u_{n\boldsymbol{k}}(\boldsymbol{x})e^{i\boldsymbol{k}\boldsymbol{x}}. \tag{4.2}$$

n is the band index and $\boldsymbol{k}$ is the related momentum, u is the Block function.
Both U and u satisfy the property $K(\boldsymbol{x}) = K(\boldsymbol{x} + \boldsymbol{R})$ thanks to lattice periodicity with $\boldsymbol{R}$ being a translation vector that satisfies the previous relation. In other words one could analyse the property of only the basic lattice and retrieve all the informations.
In this contest eq. 4.1 can be rewritten by substituting the expression for ψ and performing the derivatives in the compact form

$$H_{\mathbf{k}\cdot\mathbf{p}}(\boldsymbol{k})u_{n\boldsymbol{k}} = E_n(\boldsymbol{k})u_{n\boldsymbol{k}}(\boldsymbol{x}), \tag{4.3}$$

with the Hamiltonian being

$$H_{\mathbf{k}\cdot\mathbf{p}} = \left(-\frac{\hbar^2}{2m_0}\nabla^2 + \frac{\hbar}{m_0}\boldsymbol{k}\boldsymbol{p} + \frac{\hbar^2k^2}{2m_0} + U(\boldsymbol{x})\right), \tag{4.4}$$

where the definition $\boldsymbol{p} = -i\hbar\nabla$ was used.
Since we are in an easy configuration, the different plane waves varies slowly (this fact is expected to appear in this case where a continuous infinite bulk is considered and so no jumps in materials are present). As a consequence wave-function with different $\boldsymbol{k}$ will not interact one with the other.
Within the **k·p** method, the idea is to solve eq. 4.3 for point of the reciprocal lattice with high symmetry of the band structure, often the Γ point placed at $k = 0$ is a good choice. In this way eq 4.4 can be simplified leading to

$$\left(-\frac{\hbar^2}{2m_0}\nabla^2 + U(\boldsymbol{x})\right)u_{n0}(\boldsymbol{x}) = E_n(0)u_{n0}(\boldsymbol{x}). \tag{4.5}$$

The periodic function u_{n0} can be expressed as if containing also non-centred terms away from Γ point, in other words the non zone centred values are threaten in a perturbative way, namely

$$u_{m\boldsymbol{k}}(\boldsymbol{x}) = \sum_{n'} a_{m\boldsymbol{k},n'}(\boldsymbol{x}). \tag{4.6}$$

[5]Unless when stated otherwise, we will always consider the electron in our discussion.

This aspect is fundamental, in fact it makes the following model work for low values of $\boldsymbol{k}$. The unknown coefficients $a_{m\boldsymbol{k},n'}$ are obtained by inserting eq. 4.6 in eq. 4.5, leading to

$$\sum_{n'}\left[\left(E_{n'}(0)+\frac{\hbar^2k^2}{2m_0}\right)\delta_{nn'}+\frac{\hbar}{m_0}\boldsymbol{k}\boldsymbol{p}_{nn'}\right]a_{m\boldsymbol{k},n'}=E_m(\boldsymbol{k})a_{m\boldsymbol{k},n'}. \tag{4.7}$$

Here m denote the sub-band and n represent the crystal cell index along which the discretized integration in the left side is performed. $\delta_{nn'}$ is the Kronecker delta showing that the multiplied element will be present only in diagonal terms of the associated matrix Hamiltonian. This point is crucial, in fact the h_{ij} element, where $i->n, j->n'$ is then

$$h_{ij}=\left(E_j(0)+\frac{\hbar^2k^2}{2m_0}\right)\delta_{ij}+\frac{\hbar}{m_0}\boldsymbol{k}\boldsymbol{p}_{ij}. \tag{4.8}$$

In order to solve eq. 4.3, an explicit expression for u_{n0} should be known. This is not possible, so to overcome this the Group Theory is used [21] to construct the matrix and derive symmetry properties for u_{n0}. Moreover it should be stated that the matrix element h_{ij} has infinite elements. To overcome this usually we consider few conduction and valance bands close to the gap, in fact those are the bands that play a role in light emission. We will thus note these bands as S bands, and all the other as remote bands R. So the elements related to S bands are computed explicitly and inserted in the matrix at a specific row and column of the selected band, while remote contribution are included in each element by using perturbation theory.
Generally speaking , considering several S bands we may write the total Hamiltonian as sum of $\boldsymbol{k}$ dependent Hamiltonian based on their grade.

$$\sum_{i,j}\boldsymbol{H}_{ij}^{(2)}k_ik_j+\sum_i\boldsymbol{H}_i^{(1)}k_i+\boldsymbol{H}^{(0)}. \tag{4.9}$$

The second order terms $\boldsymbol{H}_{ij}^{(2)}$ are a result of the combination of the free carrier dispersion and the perturbation treatment of bands R, while first order terms $\boldsymbol{H}_i^{(1)}$ from the direct treatment of the k·p interaction and linear spin-orbit terms, while zero order terms $\boldsymbol{H}^{(0)}$, contain zone-centred energies.
This division is useful for when the FEM (finite element method)[6] is applied, since with increasing grade we have more derivatives, the resulting coefficient from the method will be differently.

4.3 QW case

In the previous section, the crystal was assumed to be homogeneous and infinite. In our case this assumption is no longer valid and the symmetry of the system is broken

[6]In this thesis the FEM is not treated. The FEM implemented may be retrieved from [21] or derived manually from equation 4.15 using the final 4x4 block diagonalized matrices.

in certain directions. As a consequence a carrier might be energetically confined within a lower-band gap material, but still free to propagate within the translational invariant direction. In the case of a quantum well, the symmetry is broken by the atoms of the other species in one direction, in other words the number of invariant directions is reduced to two. As a result, the Bloch function employing the plane wave approximation has to be modified

$$\Psi_{m\boldsymbol{k}_\parallel}(\boldsymbol{r}, z) = \sum_n u_n(\boldsymbol{r}, z) e^{i\boldsymbol{k}_\parallel \boldsymbol{r}} F_{n\boldsymbol{k},m}(z). \tag{4.10}$$

Here, $\boldsymbol{r}$ denotes the coordinate of translational invariant direction, z is the coordinate of the confined direction. $u_n(\boldsymbol{r}, z)$ i still a lattice-periodic function. The crystal momentum k is continuous within the translational invariant direction, while along the direction of broken symmetry is not defined. $F_{n\boldsymbol{k},m}(z)$ is referred to as slowly-varying envelope and denotes at every position in the direction z, how the lattice-periodic functions are mixed together. In a nanostructure, the decoupling of functions is only true for the translational invariant direction (as in the Bulk case), while in the symmetry broken direction, the states are mixed together. As a result of the symmetry breaking, the bands are split into sub-bands, depending on the transversal crystal momentum $k_\parallel = \sqrt{k_x^2 + k_y^2}$. Thus now the aim is to select a suitable set of lattice periodic functions $u_n(r, z)$ for eq. 4.10 and determine $F_{n\boldsymbol{k},m}(z)$.

In our discussion $1CB$ and $3VB$ are implemented, with the valance band made by HH (Heavy Holes), LH (Light Holes) and SO (Split Off) bands. Considering the conduction band, and placing ourself in the case $k_\parallel = 0$ we arrive to eq.4.5 can be generally written as

$$\left(-\frac{\hbar^2}{2m^*(z)}\frac{\partial^2}{\partial z^2} + E_c(z)\right) F_s(z) = E(0) F_s(z). \tag{4.11}$$

Here $E_c(z)$ is the bulk conduction band which depends on z and so changes along the different layers. It corresponds to the direct band gap semiconductors at γ. m labels the considered sub-band.

From the previous expression we may use $E_m(z) = E_m(0) + \frac{\hbar^2 k^2}{2m_Q}$ with m_Q being the dominant effective mass of the QW. But this expression may give imaginary values of energy.

Knowing this and in order to avoid jumps in the probability meaning of ψ, the second order differential operator in eq. 4.11 has been written as

$$-\frac{\hbar^2}{2m^*(z)}\nabla^2 -> -\nabla\frac{\partial}{\partial z}\frac{\hbar^2}{2m^*(z)}\nabla, \tag{4.12}$$

this operation is called operator ordering and can be formulated in different forms. The necessity to implement this operation is due to non-bulk structures where interfaces related to different nano-structures arise. Moreover the operator ordering consists in splitting all the contribution of the type Nk_ik_j in two components

$$Nk_ik_j -> -\partial_i N\partial_j - \partial_j N\partial_i, \tag{4.13}$$

where the derivatives come from the operators $k_{i,j}$. In normal Bulk crystal the operators would commute and this difference would not be present. While in the case of heterostructure the previous equation may not be symmetric[7]. As a consequence the type of ordering implemented here is the Burt-Foreman one[23].
With this implementation eq. 4.3 can be written, in analogy with the simple case zone-centred, as

$$\boldsymbol{H}_{\mathbf{k}\cdot\mathbf{p}}(z)\boldsymbol{F}(s) = E\boldsymbol{F}(z), \tag{4.14}$$

with $\boldsymbol{F}(z)$ being composed by all the sub-bands envelopes, i.e $\boldsymbol{F}(z) = (F_1(z), F_2(z), ... F_M(z))^T$. The transpose is need since it has to be a column vector to satisfy the previous equation. Here $\boldsymbol{H}_{\mathbf{k}\cdot\mathbf{p}}(z)$ is defined again by following the division of eq. 4.9.

$$\begin{aligned}\boldsymbol{H}_{\mathbf{k}\cdot\mathbf{p}} = &-\sum_{i,j}\partial_i \boldsymbol{H}^{(2)}_{ij}(\boldsymbol{x};\boldsymbol{k}_\parallel)\partial_j \\ &+\sum_i\left(\boldsymbol{H}^{(1)}_{i;L}(\boldsymbol{x};\boldsymbol{k}_\parallel)\partial_i + \partial_j \boldsymbol{H}^{(1)}_{i;R}(\boldsymbol{x};\boldsymbol{k}_\parallel)\right) + \boldsymbol{H}^{(0)}(\boldsymbol{x};\boldsymbol{k}_\parallel).\end{aligned} \tag{4.15}$$

Indexes L and R refer to left and right side of the first order Hamiltonian.
By using the operator ordering theory and following [23], we can get a more complex version of the terms given by eq. 4.15

$$\begin{aligned}&-\frac{\hbar^2}{2m_0}\sum_{s'}\nabla\left[\gamma^{(r)}_{ss'}(E,\boldsymbol{x})\nabla F'_s(\boldsymbol{x})\right] \\ &+\sum_{s'}\frac{-i\hbar}{m_0}\boldsymbol{p}_{ss'}\nabla F_{s'}(\boldsymbol{x}) + \sum_{s'}H^{(r)}_{ss'}(E,\boldsymbol{x})F_{s'}(\boldsymbol{x}) = EF_s(x),\end{aligned} \tag{4.16}$$

where the index s refers to the dominant contribution of the chosen band. While r is associated to the remote sub-bands effects on the various envelopes F_s. With the latter now related the wave-function of the considered band as

$$\psi_{T,s} = \sum_{n'}^{N_s} b_{s,n'}F'_{s,n'}. \tag{4.17}$$

Here the index s refers to CB, HH, LH and SO. In other words the total envelope wave-function is given by the contribution of all bound states of that type up to N_s (in which remote contributions from the interaction with other sub-bands are included). With such definition, now the exact total wave-function for one of the four generic band s is

$$\Psi_s = \psi_{T,s}u(\boldsymbol{r},z)e^{i\boldsymbol{k}_\parallel\boldsymbol{r}}. \tag{4.18}$$

Note that in eq. 4.16 also envelopes between remote bands with each other were present, but neglected since much more smaller than the single band ones. The effects of the

[7]For example the index j could refer to another material with respect to i, especially at the interface. Resulting in an error and some spurious effects such as bands in the band-gap.

operator ordering lies in the quantities γ and H, in fact they are defined as

$$\begin{aligned}\gamma^{(r)}_{ss'}(E,\boldsymbol{x}) &= \overbrace{\boldsymbol{I}\delta_{ss'}}^{dominant} + \overbrace{\frac{2}{m_0}\sum_r \boldsymbol{p}_{sr}\frac{1}{(E-H_{rr}(\boldsymbol{x}))}\boldsymbol{p}_{rs'}}^{remote} \\ H^{(r)}_{ss'}(E,\boldsymbol{x}) &= H_{ss'}(\boldsymbol{x}) + \sum_r H_{sr}(\boldsymbol{x})\frac{1}{(E-H_{rr}(\boldsymbol{x}))}H_{rs'}(\boldsymbol{x}),\end{aligned} \tag{4.19}$$

with $\boldsymbol{I}$ being the identity matrix. It is clear that eq. 4.16 is similar to eq. 4.15. Knowing this, the aim now is to find an analytical form for $\boldsymbol{H}_{\mathbf{k\cdot p}}$ by performing the different operation included in eq. 4.19 and 4.16. In the following the matrices for Zinc-blende are presented and briefly explained.

4.3.1 8x8 k·p formulation

Before starting, it is necessary to define the correct basis function that are used to obtain the different elements of the matrix. To do so, we have to consider the symmetry group of the Hamiltonian, in the case of zinc-blende crystal it is called T_d, tetrahedron group. T_d has in total five distinct irreducible representations, which are commonly labelled as Γ_1,Γ_2, Γ_{12}, Γ_{15}, and Γ_{25} [28]. Γ_1 and Γ_2 are one dimensional representations, Γ_{12} is a two dimensional and Γ_{15} and Γ_{25} are three dimensional. All irreducible representations can be associated to a combination of the basis function x, y, z . The one that are useful for our purpose is Γ_1 and Γ_{15}. The first one can be used to represent the conduction band in Γ point: it has a s symmetry, meaning that it undergoes no changes when any element of the group T_d acts on it. While Γ_{15} is used for the valance band. In this case, if we neglect the effect of the spin, the valance band becomes triple degenerate: heavy holes, light holes and split off sub-bands coincide. The basis function will then be given by x, y, z combination upon the application of a vector of coordinates [21]. The combination of all the previous listed bands will give zero and non zero values, in this way the element of the matrices are recovered by considering the associated wave function in that particular basis set.

We defined now the column $\langle s|$,$\langle x|$,$\langle y|$,$\langle z|$ and perform all the possible operations with row formed by $|s\rangle$,$|x\rangle$,$|y\rangle$,$|z\rangle$. In the case of direct interaction terms between the bands close to the gap, we have[28]

$$\boldsymbol{H}_{d4} = \begin{pmatrix} E_c & ik_xP_0 & ik_yP_0 & ik_zP_0 \\ -ik_xP_0 & E_v - \frac{\Delta}{3} & 0 & 0 \\ -ik_yP_0 & 0 & E_v - \frac{\Delta}{3} & 0 \\ -ik_zP_0 & 0 & 0 & E_v - \frac{\Delta}{3} \end{pmatrix}, \tag{4.20}$$

for example the combination $\langle s|\, H\, |s\rangle$ gives, as expected the conduction bands, being the basis state belonging to that by construction. Same for the combinations$\langle x|\, H\, |x\rangle$, $\langle y|\, H\, |y\rangle$, and $\langle z|\, H\, |z\rangle$ that always give E_v, the spin orbit term is included in all three in

order to shift the band gap in accord with experimental values. The other elements can be seen as the effect of inter-band transitions between the valance and conduction band, this transition represented by the momentum matrix element $P_0 = \sqrt{\frac{\hbar^2}{2m_0}Ep}$. Where E_p is the optical matrix parameter obtained experimentally. Lastly the zero value terms arise form the fact that we are considering degenerate bands and so the direct transitions of one state into itself is zero.
The next step is to include remote contributions, to do so the interactions between Γ_{15} and Γ_1 are calculated and included. In the first case the only contribution derives from the Γ_1 state, while for the second one, all representations play a role except for Γ_2. The remote 4x4 matrix is then

$$\boldsymbol{H}_{r4} = \begin{pmatrix} A(k_x^2+k_y^2+k_z^2) & 0 & 0 & 0 \\ 0 & k_x^2L+k_y^2M+k_z^2M & k_xN_Rk_y+k_yN_Lk_x & k_xN_Rk_z+k_zN_Lk_x \\ 0 & k_yN_Rk_x+k_xN_Lk_y & k_y^2L+k_x^2M+k_z^2M & k_yN_Rk_z+k_zN_Lk_y \\ 0 & k_zN_Rk_x+k_xN_Lk_z & k_zN_Rk_y+k_yN_Lk_z & k_z^2L+k_x^2M+k_y^2M \end{pmatrix}. \quad (4.21)$$

Here the interaction terms between $\langle s|$ and other basis function given by x, y, z has been neglected since the related coefficient is small[21]. Note that the different interaction terms between the representation of Γ may give rise to f orbitals aside the usual p and d. Such orbitals effects are completely neglected due to the fact that in semiconductors they are often not occupied and so do not take place in transition phenomena. The implemented order is the one of Burt-Foreman that allows to write two different N coefficient that otherwise would be equal[29], the value of all coefficients are:

- $A = \frac{\hbar^2}{2m_c'm_0}$.
- $L = -\frac{\hbar^2}{2m_0}(\gamma_1 + 4\gamma_2)$.
- $M = -\frac{\hbar^2}{2m_0}(\gamma_1 - 2\gamma_2)$.
- $N_L = M - \frac{\hbar^2}{2m_0}$.
- $N_R = -\frac{\hbar^2}{2m_0}6\gamma_3 - N_L$.

Where$\gamma_{1,2,3}$ are the modified Luttinger parameters which are based on the spin orbit coupling acting on the p orbitals. Normally they are defined only for VB bases[8]. However the introduction of the CB $s$type bands requires to subtract its contribution to the experimentally measured Luttinger parameters γ^{Lu}, so[24]

- $\gamma_1 = \gamma_1^{Lu} - \frac{E_p}{3E_g}$.
- $\gamma_2 = \gamma_2^{Lu} - \frac{E_p}{6E_g}$.

[8]The original Luttinger parameters are defined for the 6x6 kp method implementing only three VB with spin up and down for a total of six elements (Kane parameters). In our case, counting the CB we have $2(spin)\cdot(1(CB)+3(HH+LH+SO)) = 8bands$. In this way the modification is justified

- $\gamma_3 = \gamma_3^{Lu} - \frac{E_p}{6E_g}$.

Lastly in the term A also a corrected electron effective mass m_c' is introduced by including the effect of remote bands which counter-act free electron dispersion [30]

$$m_c' = \left(\frac{1}{m_c} + E_p \frac{E_p + \frac{2}{3}\Delta}{E_g(E_g + \Delta)} \right)^{-1}. \tag{4.22}$$

Considering the previous two Hamiltonian we have now the 4x4 matrix expressed as $\boldsymbol{H}_{d4} + \boldsymbol{H}_{r4}$. Nonetheless by including the spin, the discussion can be extended to the 8x8 matrix Hamiltonian. The total number of states is then

$$|s\uparrow\rangle, |x\uparrow\rangle, |y\uparrow\rangle, |z\uparrow\rangle, |s\downarrow\rangle, |x\downarrow\rangle, |y\downarrow\rangle, |z\downarrow\rangle. \tag{4.23}$$

As a property of the spin variable, all interactions between different spin, i.e $\langle\uparrow|\downarrow\rangle$ or vice-versa, are zero being the spin operator diagonal.
In the zone centred equation 4.5, no operators act on the spin variable. Thus the resulting 8x8 Hamiltonian is, at first approximation, diagonal by construction in the spin variable leading to

$$\boldsymbol{H}_{rd8} = \begin{pmatrix} \boldsymbol{H}_{d4} + \boldsymbol{H}_{r4} & 0 \\ 0 & \boldsymbol{H}_{d4} + \boldsymbol{H}_{r4} \end{pmatrix}. \tag{4.24}$$

A last adjustment is done by manually including the non-zero spin-orbit terms off the diagonal in $\boldsymbol{H}_{rd8}$. Such correction is required since, with the new basis of eight states of eq. 4.23, the spin-orbit operator is no more diagonal. As a result [31]

$$\boldsymbol{H}_{SO} = \frac{\Delta}{3} \begin{pmatrix} 0 & 0 & 0 & 0 & 0 & 0 & 0 & 0 \\ 0 & 0 & -i & 0 & 0 & 0 & 0 & 1 \\ 0 & i & 0 & 0 & 0 & 0 & 0 & -i \\ 0 & 0 & 0 & 0 & 0 & -1 & i & 0 \\ 0 & 0 & 0 & 0 & 0 & 0 & 0 & 0 \\ 0 & 0 & 0 & -1 & 0 & 0 & i & 0 \\ 0 & 0 & 0 & -i & 0 & -i & 0 & 0 \\ 0 & 1 & i & 0 & 0 & 0 & 0 & 1 \end{pmatrix}. \tag{4.25}$$

That has to be summed directly to $\boldsymbol{H}_{rd8}$ to reach the final 8x8 Hamiltonian denoted as $\boldsymbol{H}_{rd8,K}$ with the K index referring to the theory developed by Kane.

4.3.2 4x4 k·p Strain Hamiltonian

With the previous formalism a good description of the QW sub-bands has been achieved. The main advantage is the implementation of operator ordering with which the Burt Foreman ordering can be included avoiding spurious results in the band gap. However the strain, in the 8x8 model cannot be included in a common way as done in [21] and [32]

from the fact that the implemented Hamiltonian is of the type 6x6. But most importantly, it[21] requires an uniform strain, i.e or stress either tensile strain along the whole structure. Thus it is not viable in the present analysis due to the fact that in the QW we have both the type of strain. Moreover in that model the axial approximation is not valid, as a result sub-bands are not isotropic in terms of $k_{\|}$. This approximation is needed in order to simplify the calculation of the gain and be able to block diagonalize the Hamiltonian into 4x4 blocks, relieving the computational task of the sub-bands.
Thus the formulation needed is the one used in [24] and [33]. To reach this representation an inversion matrix is created so that a change in the basis representation is performed, namely

$$\boldsymbol{H}^{C}_{8x8} = \boldsymbol{U}'^{-1}_{KC}\boldsymbol{H}_{rd8,K}\boldsymbol{U}'_{KC}, \tag{4.26}$$

where $\boldsymbol{U}_{KC}$ stands for the matrix allowing the passage from Kane to Chuang formalism, it is defined as

$$\boldsymbol{U}_{KC} = \begin{pmatrix} i & 0 & 0 & 0 & 0 & 0 & 0 & 0 \\ 0 & -\frac{1}{\sqrt{2}} & -\frac{i}{\sqrt{2}} & 0 & 0 & 0 & 0 & 0 \\ 0 & 0 & 0 & \frac{2}{\sqrt{6}} & 0 & -\frac{1}{\sqrt{6}} & -\frac{i}{\sqrt{6}} & 0 \\ 0 & 0 & 0 & \frac{1}{\sqrt{3}} & 0 & \frac{1}{\sqrt{3}} & \frac{i}{\sqrt{3}} & 0 \\ 0 & 0 & 0 & 0 & i & 0 & 0 & 0 \\ 0 & 0 & 0 & 0 & 0 & \frac{1}{\sqrt{2}} & -\frac{i}{\sqrt{2}} & 0 \\ 0 & \frac{1}{\sqrt{6}} & -\frac{i}{\sqrt{6}} & 0 & 0 & 0 & 0 & \frac{2}{\sqrt{6}} \\ 0 & \frac{1}{\sqrt{3}} & -\frac{i}{\sqrt{3}} & 0 & 0 & 0 & 0 & -\frac{1}{\sqrt{3}} \end{pmatrix}. \tag{4.27}$$

Here the used coefficient are necessary to have the same factors in the new formulation. Thus by performing 4.26, using the axial approximations and separating the factors containing the operator ordering in two matrices $\boldsymbol{H}^{C}_{L}$ and $\boldsymbol{H}^{R}_{L}$ we get the final 8x8 matrices listed below.

$$\boldsymbol{H}^{C} = \begin{bmatrix} E_g + A & -\sqrt{3}V & \sqrt{2}U & U & 0 & 0 & V^* & \sqrt{2}V \\ -\sqrt{3}V^* & -P-Q & S & \frac{S}{\sqrt{2}} & 0 & 0 & -R & -\sqrt{2}R \\ \sqrt{2}U & S^* & -P+Q & \sqrt{2}Q & -V^* & -R & 0 & -\sqrt{\frac{3}{2}}S \\ U & \frac{S^*}{\sqrt{2}} & \sqrt{2}Q & -P-\Delta & \sqrt{2}V^* & \sqrt{2}R & -\frac{3}{2}S & 0 \\ 0 & 0 & -V & \sqrt{2}V & E_g + A & \sqrt{3}V^* & \sqrt{2}U & -U \\ 0 & 0 & -R^* & \sqrt{2}R^* & \sqrt{3} & -P-Q & -S^* & \frac{S^*}{\sqrt{2}} \\ V & -R^* & 0 & -\frac{3}{2}S^* & \sqrt{2}U & -S & -P+Q & -\sqrt{2}Q \\ \sqrt{2}V & -\sqrt{2}R^* & -\sqrt{\frac{3}{2}}S^* & 0 & -U & \frac{S}{\sqrt{2}} & -\sqrt{2}Q & -P-\Delta \end{bmatrix}. \tag{4.28}$$

$$\boldsymbol{H}^{C}_{L} = \begin{bmatrix} 0 & 0 & 0 & 0 & 0 & 0 & 0 & 0 \\ 0 & 0 & -\frac{N_L k_z (k_x - ik_y)}{\sqrt{3}} & -\frac{N_L k_z (k_x - ik_y)}{\sqrt{6}} & 0 & 0 & 0 & 0 \\ \sqrt{\frac{2}{3}}P_0 k_z & -\frac{N_R k_z (k_x + ik_y)}{\sqrt{3}} & 0 & 0 & 0 & 0 & \frac{k_z (N_L - N_R)(k_y + ik_x)i}{3} & \frac{\sqrt{2}}{6}(k_z (k_y + ik_x)(N_L + 2N_R)i) \\ \sqrt{3}P_0 k_z & -\frac{N_R k_z (k_x + ik_y)}{\sqrt{6}} & 0 & 0 & 0 & 0 & \frac{\sqrt{2}}{6}(k_z (k_y + ik_x (N_R + 2N_L)i) & \frac{k_z (N_L - N_R)(k_y + ik_x)i}{3} \\ 0 & 0 & 0 & 0 & 0 & 0 & 0 & 0 \\ 0 & 0 & 0 & 0 & 0 & 0 & \frac{N_L k_z (k_x + ik_y)}{\sqrt{3}} & -\frac{N_L k_z (k_x + ik_y)}{\sqrt{6}} \\ 0 & 0 & \frac{k_z (N_L - N_R)(k_x + ik_y)i}{3} & \frac{\sqrt{2}}{6}(k_z (k_x + ik_y)(N_L + 2N_R)i) & \sqrt{\frac{2}{3}}P_0 k_z & \frac{N_L k_z (k_x - ik_y)}{\sqrt{3}} & 0 & 0 \\ 0 & 0 & \frac{\sqrt{2}}{6}(k_z (k_x + ik_y)(N_R + 2N_L)i) & \frac{k_z (N_L - N_R)(k_x + ik_y)i}{3} & -\sqrt{3}P_0 k_z & -\frac{N_R k_z (k_x - ik_y)}{\sqrt{6}} & 0 & 0 \end{bmatrix}. \tag{4.29}$$

$$\boldsymbol{H}_R^C = \begin{bmatrix} 0 & 0 & \sqrt{\frac{2}{3}}P_0k_z & \sqrt{3}P_0k_z & 0 & 0 & 0 & 0 \\ 0 & 0 & -\frac{N_Rk_z(k_x-ik_y)}{\sqrt{3}} & -\frac{N_Rk_z(k_x-ik_y)}{\sqrt{6}} & 0 & 0 & 0 & 0 \\ 0 & -\frac{N_Lk_z(k_x+ik_y)}{\sqrt{3}} & 0 & 0 & 0 & 0 & -\frac{k_z(N_L-N_R)(k_y+ik_x)i}{3} & -\frac{\sqrt{2}}{6}(k_z(k_y+ik_x)(N_R+2N_L)i) \\ 0 & -\frac{N_Lk_z(k_x+ik_y)}{\sqrt{6}} & 0 & 0 & 0 & 0 & -\frac{\sqrt{2}}{6}(k_z(k_y+ik_x)(N_L+2N_R)i) & -\frac{k_z(N_L-N_R)(k_y+ik_x)i}{3} \\ 0 & 0 & 0 & 0 & 0 & 0 & \sqrt{\frac{2}{3}}P_0k_z & -\sqrt{3}P_0k_z \\ 0 & 0 & 0 & 0 & 0 & 0 & \frac{N_Rk_z(k_x+ik_y)}{\sqrt{3}} & -\frac{N_Rk_z(k_x+ik_y)}{\sqrt{6}} \\ 0 & 0 & -\frac{k_z(N_L-N_R)(k_x+ik_y)i}{3} & \frac{\sqrt{2}}{6}(k_z(k_x+ik_y)(N_R+2N_L)i) & 0 & \frac{N_Lk_z(k_x-ik_y)}{\sqrt{3}} & 0 & 0 \\ 0 & 0 & \frac{\sqrt{2}}{6}(k_z(k_x+ik_y)(N_L+2N_R)i) & -\frac{k_z(N_L-N_R)(k_x+ik_y)i}{3} & 0 & -\frac{N_Lk_z(k_x+ik_y)}{\sqrt{6}} & 0 & 0 \end{bmatrix}. \tag{4.30}$$

Where new used parameters are

- $A = \frac{\hbar^2}{2m_0m_c'}(k_\parallel^2 + k_z^2)$.
- $P = \frac{\hbar^2}{2m_0}\gamma_1(k_\parallel^2 + k_z^2)$.
- $Q = \frac{\hbar^2}{2m_0}\gamma_2(k_\parallel^2 - 2k_z^2)$.
- $R = \frac{\sqrt{3}\hbar^2}{2m_0}(-\bar{\gamma}(k_x^2 - k_y^2) + 2i\bar{\gamma}k_xk_y)$.
- $S = \frac{\hbar^2}{2m_0}\frac{2\gamma_3(k_x-ik_y)k_z}{\sqrt{3}}$.
- $V = \frac{P_0(k_x+ik_y)}{\sqrt{6}}$.
- $U = \frac{P_0k_z}{\sqrt{3}}$.

And $\bar{\gamma} = \frac{\gamma_2+\gamma_3}{2}$. The matrix $\boldsymbol{H}^C$ is exactly equal to the one formulated by [33], what is more here is the presence of $\boldsymbol{H}_R^C$ and $\boldsymbol{H}_L^C$. The strain is thus included by direct comparison[9] of the matrix terms A,P and Q with the addition of the strain terms[33], resulting in the addition of the terms

- $A_{str} = a_c(\epsilon_{xx} + \epsilon_{yy} + \epsilon_{zz})$.
- $P_{str} = -a_v(\epsilon_{xx} + \epsilon_{yy} + \epsilon_{zz})$.
- $Q_{str} = -\frac{b}{2}(\epsilon_{xx} + \epsilon_{yy} - 2\epsilon_{zz})$.

With the constants a_c,a_v and b defined in Chapter 3.
And finally by applying the axial approximation, the matrix $\boldsymbol{U}_{8->4}$ can be defined as

[9]This way of proceeding is justified by the fact that the matrix from [33]is equal to the present case, so we can consider the theory used to arrive to the strained Hamiltonian valid here too. Although it is important to notice that the operator ordering terms does not take part in the strain, any additional terms resulting from the strain are here neglected (even if present, the addition from [21] should be avoided due to the fact that, in that theory, the strain must be uniform, which it is not the present case)

$$\boldsymbol{U}_{8->4} = \begin{pmatrix} e^{-i\frac{\phi}{2}} & 0 & 0 & 0 & ie^{i\frac{\phi}{2}} & 0 & 0 & 0 \\ 0 & e^{-i\frac{3\phi}{2}} & 0 & 0 & 0 & -ie^{i\frac{3\phi}{2}} & 0 & 0 \\ 0 & 0 & ie^{-i\frac{\phi}{2}} & 0 & 0 & 0 & -e^{i\frac{\phi}{2}} & 0 \\ 0 & 0 & 0 & -ie^{-i\frac{\phi}{2}} & 0 & 0 & 0 & -e^{i\frac{\phi}{2}} \\ e^{-i\frac{\phi}{2}} & 0 & 0 & 0 & -ie^{i\frac{\phi}{2}} & 0 & 0 & 0 \\ 0 & e^{-i\frac{3\phi}{2}} & 0 & 0 & 0 & ie^{i\frac{3\phi}{2}} & 0 & 0 \\ 0 & 0 & -ie^{-i\frac{\phi}{2}} & 0 & 0 & 0 & -e^{i\frac{\phi}{2}} & 0 \\ 0 & 0 & 0 & ie^{-i\frac{\phi}{2}} & 0 & 0 & 0 & -e^{i\frac{\phi}{2}} \end{pmatrix}, \tag{4.31}$$

where ϕ is the azimuthal angle formed by k_x and k_y, it can be obtained as $\phi = tan^{-1}(\frac{k_y}{k_x})$. By putting ourself in the case where one of the two between k_x and k_y is zero and performing the same operation has done in eq. 4.26 we get

$$\boldsymbol{H}^C = \begin{pmatrix} \boldsymbol{H}^U_{4x4} + \boldsymbol{H}^U_{R,4x4} + \boldsymbol{H}^U_{L,4x4} & 0 \\ 0 & \boldsymbol{H}^L_{4x4} + \boldsymbol{H}^L_{R,4x4} + \boldsymbol{H}^L_{L,4x4} \end{pmatrix}, \tag{4.32}$$

with each matrix is listed below. This is the final result and contains all the implemented matrix through which the Schroedinger equation. As cited earlier a FEM of eq.4.9 is performed. The left and right matrices implementing the operator ordering are all related to first order term for k_z. While the zero and second order terms are generally extrapolated from $\boldsymbol{H}^{U/L}_{4x4}$.

The upper and lower matrices are not implemented at the same time, rather only the upper version of each matrix are considered. This hugely speeds up the computational time still maintaining a fair good result, but gives the necessity to double the obtained gain. An important note should be done in order to fully understand the next section. These matrices are constructed in such a way that from the solver each solution will give all the contributions from the other bands. This means that when looking at the VB, also the contribution related to the interaction with the CB and other VBs are included (if they are not degenerate, otherwise it would be zero) and vice-versa. Moreover the order of these contribution is always the same by construction of the matrix: from row one to the fourth, the bands are respectively CB, HH (heavy holes) VB, LH (hight Holes) VB and SO (split off) VB.

$$\boldsymbol{H}^U_{4x4} = \begin{pmatrix} E_c + A & -\sqrt{3}V & -V + i\sqrt{2}U & -\sqrt{2}V - iU \\ -\sqrt{3}V & -P - Q & R + iS & \sqrt{2}R - \frac{i}{\sqrt{2}S} \\ -V - i\sqrt{2}U & R - iS & -P + Q & -\sqrt{2}Q - i\sqrt{\frac{3}{2}}S \\ -\sqrt{2}V + iU & \sqrt{2}R + \frac{i}{\sqrt{2}}S & \sqrt{2}Q + i\sqrt{\frac{3}{2}}S & -P - \Delta \end{pmatrix} \tag{4.33}$$

$$\boldsymbol{H}^{L}_{4x4} = \begin{pmatrix} E_c + A & -\sqrt{3}V & -V - i\sqrt{2}U & -\sqrt{2}V + iU \\ -\sqrt{3}V & -P - Q & R - iS & \sqrt{2}R + \frac{i}{\sqrt{2}S} \\ -V + i\sqrt{2}U & R + iS & -P + Q & -\sqrt{2}Q + i\sqrt{\frac{3}{2}}S \\ -\sqrt{2}V - iU & \sqrt{2}R + \frac{i}{\sqrt{2}}S & \sqrt{2}Q - i\sqrt{\frac{3}{2}}S & -P - \Delta \end{pmatrix} \tag{4.34}$$

$$\boldsymbol{H}^{U}_{R,4x4} = \begin{pmatrix} 0 & 0 & ik_z\sqrt{\frac{3}{2}}P_0 & -ik_z\frac{P_0}{\sqrt{3}} \\ 0 & 0 & -ik_zk_x\frac{N_R}{\sqrt{3}} & ik_zk_x\frac{N_R}{\sqrt{6}} \\ 0 & ik_zk_x\frac{N_L}{\sqrt{3}} & ik_zk_x\frac{N_L-N_R}{3} & \sqrt{2}ik_zk_x\frac{2N_L+N_R}{6} \\ 0 & -ik_zk_x\frac{N_L}{\sqrt{6}} & -\sqrt{2}ik_zk_x\frac{N_L+2N_R}{6} & -ik_zk_x\frac{N_L-N_R}{3} \end{pmatrix} \tag{4.35}$$

$$\boldsymbol{H}^{L}_{R,4x4} = \begin{pmatrix} 0 & 0 & -ik_z\sqrt{\frac{3}{2}}P_0 & ik_z\frac{P_0}{\sqrt{3}} \\ 0 & 0 & ik_zk_x\frac{N_R}{\sqrt{3}} & -ik_zk_x\frac{N_R}{\sqrt{6}} \\ 0 & -ik_zk_x\frac{N_L}{\sqrt{3}} & -ik_zk_x\frac{N_L-N_R}{3} & -\sqrt{2}ik_zk_x\frac{2N_L+N_R}{6} \\ 0 & ik_zk_x\frac{N_L}{\sqrt{6}} & \sqrt{2}ik_zk_x\frac{N_L+2N_R}{6} & ik_zk_x\frac{N_L-N_R}{3} \end{pmatrix} \tag{4.36}$$

$$\boldsymbol{H}^{U}_{L,4x4} = \begin{pmatrix} 0 & 0 & 0 & 0 \\ 0 & 0 & -ik_zk_x\frac{N_L}{\sqrt{3}} & ik_zk_x\frac{N_L}{\sqrt{6}} \\ -ik_z\sqrt{\frac{3}{2}}P_0 & ik_zk_x\frac{N_R}{\sqrt{3}} & -ik_zk_x\frac{N_L-N_R}{\sqrt{3}} & \sqrt{2}ik_zk_x\frac{N_L+2N_R}{6} \\ ik_zk_x\frac{P_0}{\sqrt{3}} & -ik_z\sqrt{\frac{3}{2}}P_0 & -\sqrt{2}ik_zk_x\frac{2N_L+N_R}{6} & ik_zk_x\frac{N_L-N_R}{3} \end{pmatrix} \tag{4.37}$$

$$\boldsymbol{H}^{L}_{L,4x4} = \begin{pmatrix} 0 & 0 & 0 & 0 \\ 0 & 0 & ik_zk_x\frac{N_L}{\sqrt{3}} & -ik_zk_x\frac{N_L}{\sqrt{6}} \\ ik_z\sqrt{\frac{3}{2}}P_0 & -ik_zk_x\frac{N_R}{\sqrt{3}} & ik_zk_x\frac{N_L-N_R}{\sqrt{3}} & -\sqrt{2}ik_zk_x\frac{N_L+2N_R}{6} \\ -ik_zk_x\frac{P_0}{\sqrt{3}} & ik_z\sqrt{\frac{3}{2}}P_0 & \sqrt{2}ik_zk_x\frac{2N_L+N_R}{6} & -ik_zk_x\frac{N_L-N_R}{3} \end{pmatrix} \tag{4.38}$$

4.4 QW sub-bands

With the previously defined formalism, the Schrödinger equation can be solved by forming the related matrices and using the FEM. The used constants are reported in Appendix B. The Eigenvalue equation given by eq. 4.14 is computed along the whole z axis by using the band structure calculated in Chapter 3 with the only difference that the VB is set to zero. The splitting depicted in fig (b) 3.5 uses the additional term related to the strain from A_{str},P_{str}, andQ_{str}, while here these terms are not included as a requirement of the model [24]. They are used in order to check the validity of the correct implementation by comparing the wave-functions $\psi_{T,s}$ and eigenvalues $E^{lc,lv}_{c,v}$ from the **k·p** method with a simple 1D FEM static Schrödinger equation at $\boldsymbol{k}_{\parallel} = 0$. In the latter effects such as

remote bands or VB influence on the CB are not included together with no strain terms, so some differences should be present. In this contest the strained band diagram with the additional terms explained before is used e in order to include the strain directly in the potential V acting on the electron[10]
Lastly the solver computes, for the well and the barrier, first the Hamiltonian related to the bulk cases and then they are combined linearly one with the other using the molar concentration of dopants.
For example, for the well $\boldsymbol{H}_{tot} = \boldsymbol{H}_{GaAs}x + (1-x)\boldsymbol{H}_{InAs}$. The barrier is threaten in the similar way but with GaP instead of InAs. The maximum $\boldsymbol{k}_{\parallel}$ is set to $0.18\mathring{A}^{-1}$, higher values may give wrong results, such as band crossing, due to the fact that the model starts to lose validity with increasing magnitude of transversal crystal momentum. Nonetheless at those high energies the sub-bands are most likely not populated, thus we can in principle use higher k. This is important, especially for the gain computation where the maximum value is $0.28\mathring{A}^{-1}$.

Table 4.1: Constants for sub-bands calculation, from [22]. While the Luttinger parameters for InAs comes for [25].

Symbol	Parameter	*GaAs*	*InAs*	*GaP*
γ_1^{Lu}, eV	Luttinger paramater	6.85	16.5	4.05
γ_2^{Lu}, eV	Luttinger paramater	2.10	6.77	0.49
γ_3^{Lu}, eV	Luttinger paramater	2.9	7.64	1.25
E_g, eV	Energy gap	1.412	0.354	2.776
E_p, eV	Optical matrix parameter	25.7	22.2	22.2
m_c/m_0	Electron effective mass	0.067	0.0224	0.08

1QW

Considering only one Quantum Well, figure 4.1 shows the obtained sub-bands in the case of strain set to zero (a) and the real case (b). The first thing to be noticed is that the allowed energies increase with increasing $\boldsymbol{k}_{\parallel}$ as expected from the theory, also for low values the CBs can be approximated as parabolic bands.

The effect of the strain is clear, in fact by looking at the unstrained and strained band diagrams in figure 3.5 the Conduction band offset decreases, as a result less CB states are confined in the system. With only one CB, the number of possible transitions is decreased

[10]In other words three different potential are defined according to the diagonals entry of matrix 4.33,with the first term corresponding to the CB, the second to the HH VB and the third to LH VB. The SO is not taken in consideration due to the fact that no sub-bands of that kind are present in the analyzed QW (unconfined state with energies higher than the barrier).

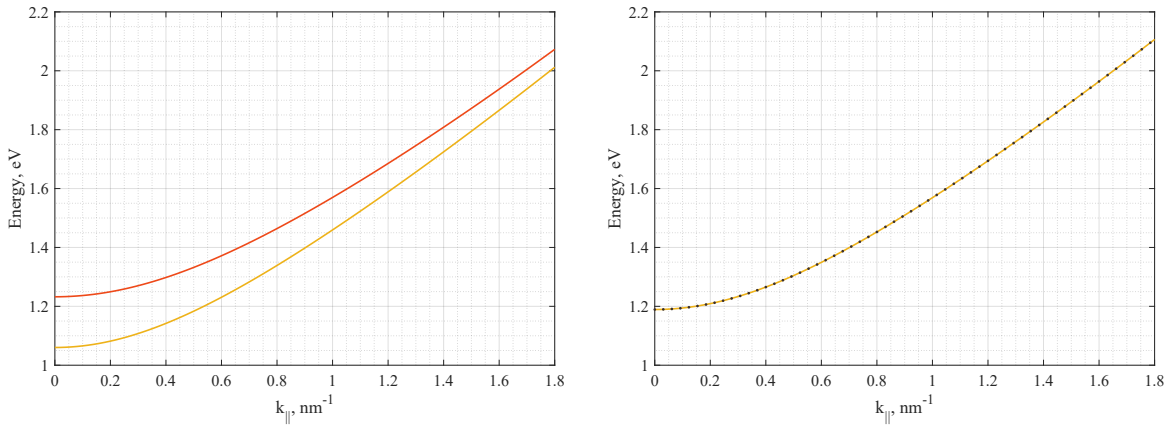

(a) *Unstrained* (b) *Strained*

Figure 4.1: CB sub-bands, single QW here, dotted line from the lower matrix implementation.

and so also the gain will be lower[11]
Moreover the dotted line in (b) represent the sub-band obtained by using the lower block of $\boldsymbol{H}^C$ in eq. 4.32. From which we see that the difference between the upper and low matrices is totally negligible. Considering only the strained case and focusing on the wave-function at $\boldsymbol{k}_{\parallel} = 0$, figure 4.2 collects the different contribution from the 4x4 matrix to the first CB. What is summed here is the probability meaning of each contribution, here we see that the main factor comes from the CB, while other are much more lower (LH and SO are multiplied by 40 to make them evident in the figure). With the HH contribution practically zero. The very low impact of the HH band is due to the fact that the effective mass on those bands is higher than the other. In fact, for an HH band generally it is $m_{hh} = \frac{1}{\gamma_1 - 2\gamma_2}$ while for LH $m_{lh} = \frac{1}{\gamma_1 + 2\gamma_2}$. These values can be obtained directly from the definition of P and Q and looking at the entrance $-P-Q$ and $-P+Q$ in matrix 4.33. Thus the contribution of energy is lower.
A last attention should be given to the shape of the CB wave-function, since it is the first CB the number of zero of the function within the domain is zero. IT is expected , also for the VB, that upon increasing the grade of the wave-function, the number of zero grows accordingly.
In the case of the VB sub-bands, figure 4.3 shows the outcome of the simulation. In opposition with the CB, the application of the strain leads to an additional VB in the well. Indeed the valance band offset ΔE_V increases from the unstrained to the strained case.

Another important aspect is the first vB sub-bands which starts before $0eV$, this is correct since the reference energy here is the unstrained valance band which is set to zero.

[11] Although the transitions from VB to CB are by large measure involving only the first CB, thus the lost of a second CB is not so much detrimental.

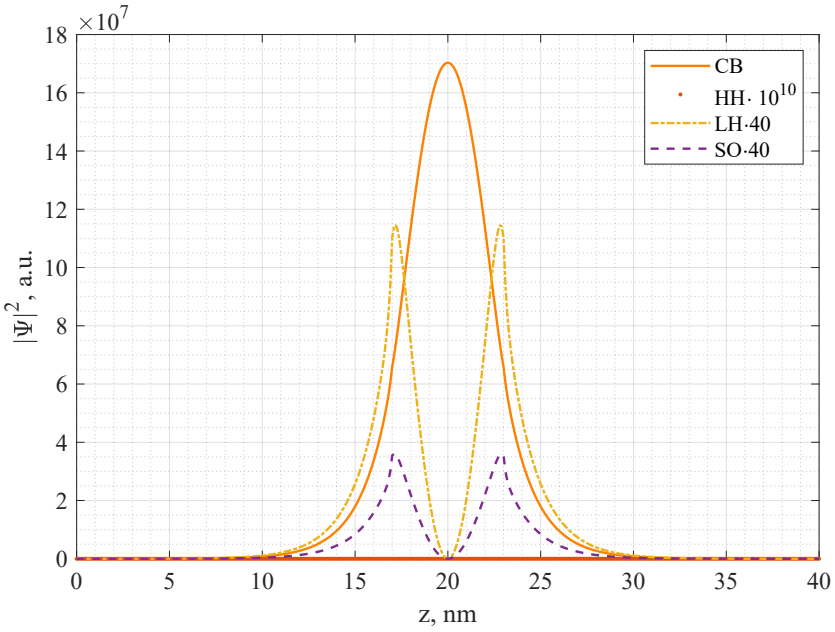

Figure 4.2: Square modulus of the wave-function of the first CB at $\boldsymbol{k}_{\parallel} = 0$ with all contributions from other sub-bands.

The decision of such notation is to compare the results with [13] [33],and [34], confirming the veracity of this shift to energies higher than zero. Nonetheless if one desires to avoid having sub-bands within the forbidden band-gap, the reference energy can be set to the VB:HH of the strained band diagram, fig 4.3.
Again the usage of the lower matrix gives the same result in terms of sub-bands energies compared with the upper matrix case.
In the case of VB it is interesting to note that the behaviour cannot be threaten with parabolic approximations, even at low $\boldsymbol{k}_{\parallel}$ and especially for the third VB which is related to LH. The coupling with the CB makes the sub-band hugely non parabolic. A confirmation of this assumptions is given by the wave-functions at $\boldsymbol{k}_{\parallel} = 0$ for the four sub-bands in fig. 4.4. In fact for the Light holes band, the 1D Schrödinger model fails and gives not only a wrong, less confined, wave function probability, but most importantly a different eigenvalue. This does not happen for the three HH sub-bands which the Schrödinger model predicts perfectly. Also the light holes wave-function is less confined with respect to HH ones, which is another reflections of the difference in effective masses.
Lastly with increasing order of the HH sub-band more peaks appear, they are related to the increase of the zeros of the wave-function (Being the modulus square plotted this information is lost). As a consequence the denotation of $HH_{1,2,3}$ is well posed. Figure 4.5 shows the aforementioned concept.

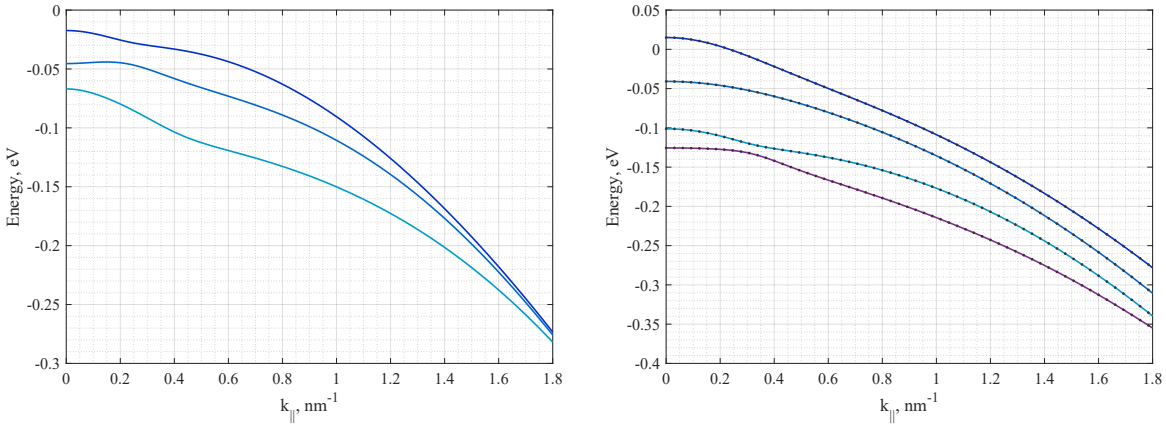

(a) *Unstrained* (b) *Strained*

Figure 4.3: VB sub-bands, single QW., dotted line from the lower matrix implementation.

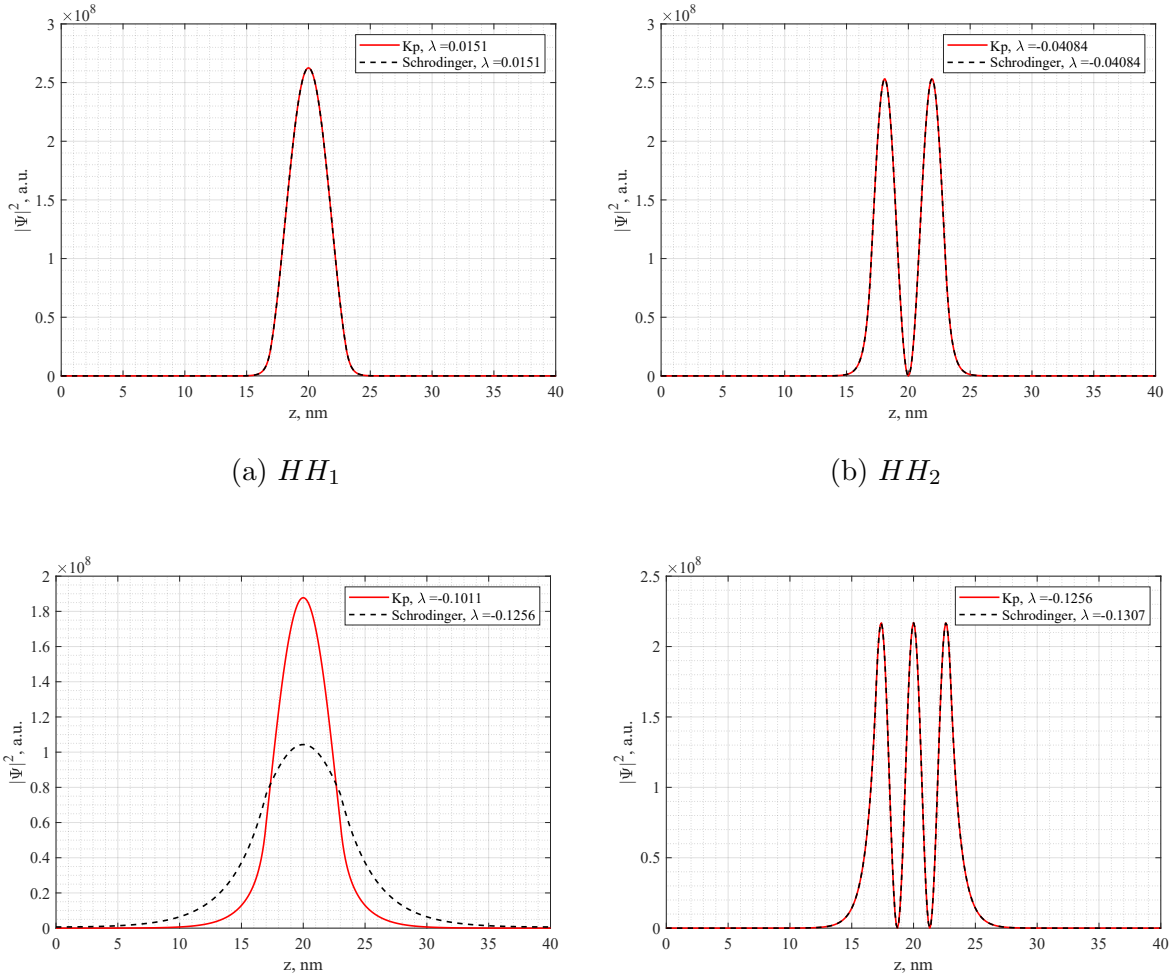

(a) HH_1 (b) HH_2

(c) LH_1 (d) HH_3

Figure 4.4: Square modulus wave-functions for the four confined VB sub-bands.

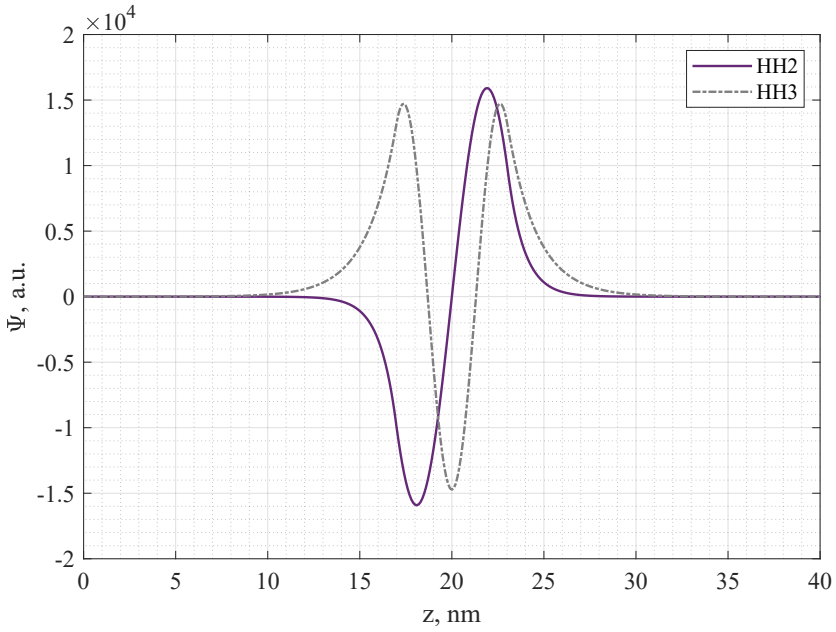

Figure 4.5: Wave-functions of HH_2 and HH_3 at $k_{\|} = 0$.

3QWs

Now the true effective active region is briefly analysed, no change of the previous formulated **k·p** model is required due to generality of the assumptions made. What changes thus is the band structure used, figure 3.6, while all the constants remains the same for the barriers and well. Figure 4.6 collects the results. Here by comparing with fig. 4.3

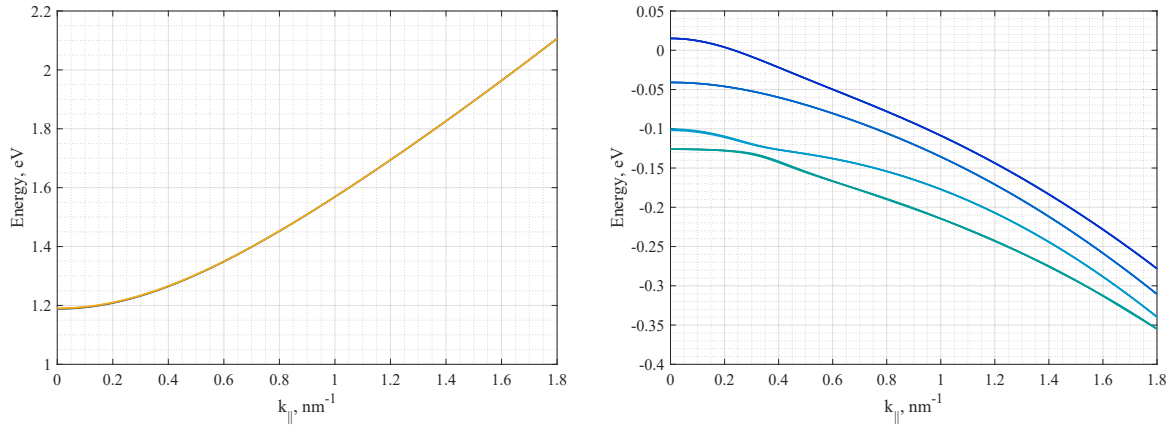

(a) CB sub-bands (b) VB sub-bands

Figure 4.6: Surface of the solutions for different values of y.

we note very few differences. Nonetheless now the sub-bands are in total 3 for CB and 12 for the VB, in other words for each CB and VB from the 1QW case now other two very similar sub-bands arise. For each triplet, the eigenvalues are almost the same, what

changes are the related wave-functions. The reason for this division should be looked at the fact that there are three QW, each one of them will present its own sub-bands. Figure 4.7 shows the three $|\psi_{T,CB}|^2$ related to the triplet of the first CB. It is clear how the three QW contributes and also interacting one with the other. In fact between the first/second and the second/third QW the probability of finding the electron in the case of CB' is not zero. This interaction is inversely proportional to the distance between the QW, if they were distant, no interactions between them will be present.
Although not shown for the 1QW case, here it is possible to notice that the Schrödinger model doesn't not predict perfectly the result, again the reason has to be searched in the interaction with the LH sub-bands belonging to the VB.

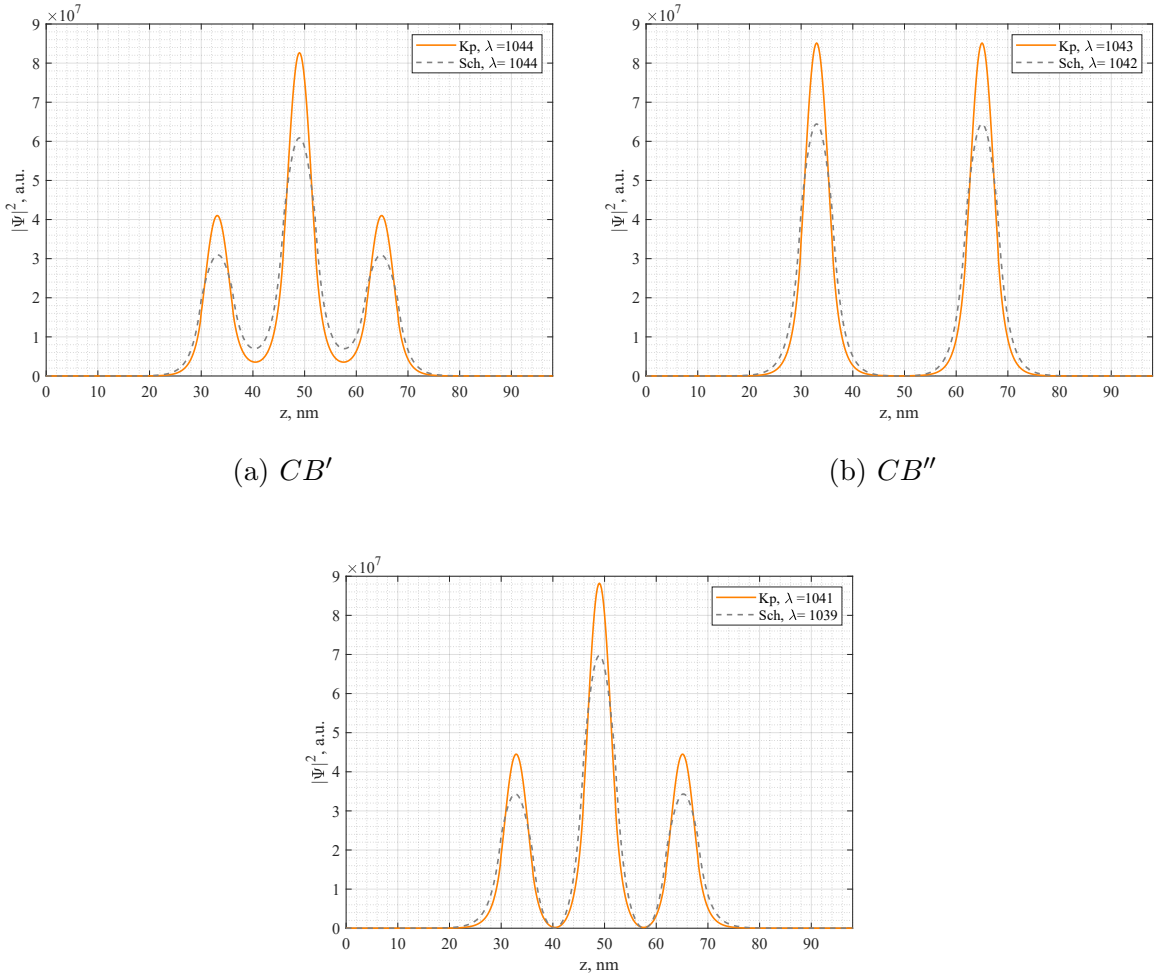

(a) CB' (b) CB''

(c) CB'''

Figure 4.7: Surface of the solutions for different values of y.

To conclude figure 4.8 complete the description of the wave-functions for the 3QWs case. The same description that has been made in the case of 1QW holds here too, the only difference is that here the 1D Schrödinger eigenvalues are in all the cases not equal to the results of the **k·p** model. Comparing the eigenvalues in this case, with those from 1QW case in fig. 4.4, we note that the results are very similar concerning the **k·p** model. So

the problem lies in the 1D static Schrödinger model that has troubles to work properly with such a complex structure.

Drawing the conclusion, since the 3QWs give sub-bands almost equal to the case of a single well, from now one the simpler one will be used in the simulation. In this way the computational time is hugely decreased.

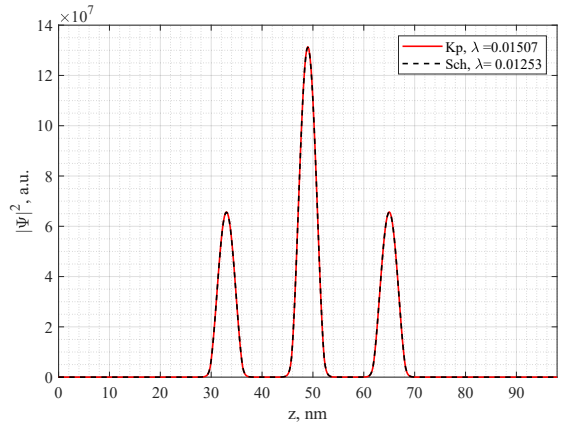

(a) HH_1

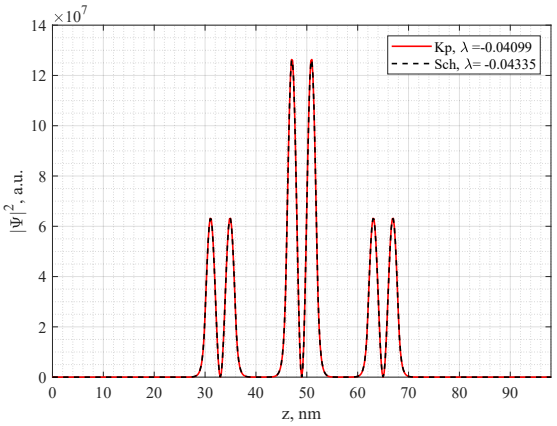

(b) HH_2

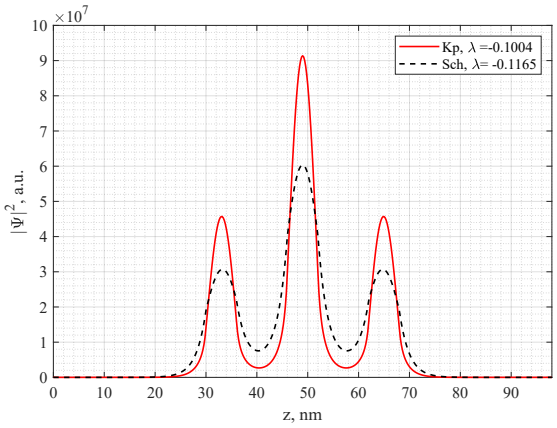

(c) LH_1

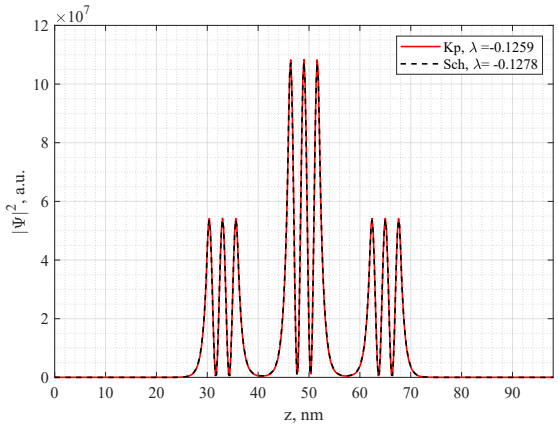

(d) HH_3

Figure 4.8: Surface of the solutions for different values of y.

Chapter 5

Optical processes

In this last theoretic part all the quantities needed for the effective linewidth calculation are retrieved. The whole description is based on the sub-bands obtained in the chapter before, more precisely both the wave-function and the associated sub-band energies are used.
The first step is to compute the gain of VCSEL, i.e amplification reached though stimulated emission of photons in the active medium. To do so the dielectric constant of the active region must be computed and then used to obtain the different needed quantities for linewidth calculation.

5.1 Dielectric constant

The dielectric constant of the material undergoes changes due to the transitions from valance band to conduction band and vice-versa. By not including the effect of exactions[12], bound electron-hole pairs generated from photons with energy higher than E_g, the change in dielectric constants is[34][35] [21]

$$\Delta\epsilon(T,\omega,n) = \frac{1}{V}\sum_{\sigma,\eta}\sum_{lc,lv}\sum_{\boldsymbol{k}_\parallel}\left|\hat{\varepsilon}\cdot\boldsymbol{M}^{\sigma\eta}_{lc,lv}(\boldsymbol{k}_\parallel)\right|^2 f_{c,v}L(\hbar\omega - E^{lc,lv}_{c,v}). \tag{5.1}$$

The involved quantities are:

- η is the electron spin.
- σ stands for the upper and lower blocks of the 4x4 matrices found in the previous chapter.

[12]This approximations is justified by the fact that the working temperature of the tested VCSELs is at room temperature or higher, thus far from the low temperature regime in which the effect of excitons is relevant.

- $\boldsymbol{M}$ is the optical dipole matrix element between a conduction sub-band lc and valance sub-bands lv.
- $f_{c,v}$ is the composition of the distributions functions of electrons and holes in the related sub-bands, here they are approximated with Fermi statistic with related Fermi energy levels. The factor depends on the choice between stimulated emission (Gain) and spontaneous emission.
- L is called lineshape and represents the broadening of the sub-bands energies when considering scattering mechanism.
- $\hat{\varepsilon}$ is the versor giving the polarization direction of the incoming optical field, in this discussion we focus only on TE (transverse mode of the electromagnetic field) so the vectors lays in the xy plane[13]
- V is the volume of the cavity, it is useful to write it as $A \cdot W$ where W is the thickness of the well.

Since in the chapter before it was clear that the upper and lower blocks gives almost the same result, to save time only the contribution to the dielectric constant from the upper matrix is computed. Then an additional 2 factor multiplying the final result. The energy $E_{cv}^{lc,lv}$ is equal to

$$E_{cv}^{lc,lv} = E_c^{lc} - E_v^{lv} + E_g, \tag{5.2}$$

where E_g is the strained band gap, which is summed to the strained sub-bands energies obtained before.
At this point the different terms composing eq. 5.1 are computed separately and a description for them is delineated to understand their role in the total expression

Dipole matrix element

The dipole matrix element is strictly related to the transition from one sub-band to another one, in quantum mechanics these are possible depending on the overlap integral of the wave-functions related to the two sub-bands. The higher it is the most probable is the transition and thus the contribution of that sub-bands to the dielectric response. By recalling eq. 4.17, we have

$$\begin{aligned} s_{hh} &= \langle \psi_{T,lc} | \psi_{T,lh} \rangle | = \sum_{i=1}^{N_{cb}} \sum_{j=1}^{N_{hh}} b_{cb,i}^* b_{hh,j} \int_z F_{cb,i}^{*\prime} F_{hh,j}^{\prime} dz \\ s_{lh} &= \langle \psi_{T,lc} | \psi_{T,hh} \rangle | = \sum_{i=1}^{N_{cb}} \sum_{j=1}^{N_{lh}} b_{cb,i}^* b_{lh,j} \int_z F_{cb,i}^{*\prime} F_{lh,j}^{\prime} dz \end{aligned} \tag{5.3}$$

[13] In the TM case it would be $\hat{\varepsilon} -> \hat{z}$ as a property of the two modes to have the versor one perpendicular to the other.

So when considering both the general type of bands, there will be contributions from the the other VB sub-bands too, due to the remote and direct contributions explained earlier. The matrix dipole element is then [35] [35]

$$\left|\hat{x}\cdot M^{\eta}_{lc,lv}(k_{\parallel})\right|^2 = R^2\left(|s_{hh}|^2+\frac{1}{3}|s_{lh}|^2-\frac{2}{\sqrt{3}}s_{hh}s_{lh}cos(2\phi)\right), \tag{5.4}$$

where R results from the spin related contribution multiplying the overlap integral and it is equal to

$$R^2 = \left(\frac{q\hbar}{2E^{lc,lv}_{cv}}\right)^2\left(E_g\frac{E_g+\Delta}{E_g+\frac{2}{3}\Delta}\right)\left(\frac{1}{m_c}-\frac{1}{m_0}\right), \tag{5.5}$$

here the 2 term form the upper and lower block approximations is included. Eq. 5.4 can be simplified by neglecting the third term where the azimuthal angle ϕ is involved. In fact its contribution to the sum over $\boldsymbol{k}_{\parallel}$ is null in case of isotropic material[14]. The final expression for the matrix dipole is different when considering spontaneous and stimulated emission.
In the case of stimulated emission it holds

$$\left|\hat{x}\cdot M^{\eta}_{lc,lv}(k_{\parallel})\right|^2 = \frac{R^2}{2}\left(|s_{hh}|^2+\frac{1}{3}|s_{lh}|^2\right), \tag{5.6}$$

whereas for spontaneous emission

$$\left|\hat{x}\cdot M^{\eta}_{lc,lv}(k_{\parallel})\right|^2_s = \frac{R^2}{2}\frac{(2|s_{hh}|^2+|s_{lh}|^2)}{3}. \tag{5.7}$$

The squared overlap integrals from eq. 5.3 are plotted in figure 5.1. For the two overlaps, the contribution to the whole HH VB from all sub-bands is plotted too. As expected for s_{hh} and s_{lh} the main effect comes from the respective, closer to the CB sub-band, sub-bands HH and LH. In the first case we note how, for the HH case, only the first sub-band takes part in the transitions, as a reflection of the fact that Heavy Holes sub-bands are not influenced so much by other sub-bands. While for the light hole case, the influence from the other sub-bands is present. Indeed it should be pointed out that the HH_1 sub-band gives the same contribution of s_{hh} for high $k_{\parallel}$, meaning that at those values the light holes sub-bands plays no role in the overlap integral with the conduction band.

The overlap integrals are naturally normalized to one due to the fact that the normalization constant b are involved in the calculation, eq. 5.3. In the figure also the contribution form the lower block (dashed line) is present. About this point again we see that the differences are totally negligible (order of magnitude of 10^{-12}). Thus, having proved that

[14]It should be remarked the fact that at the interface this statement does not hold, nonetheless in the flat band approximation this aspect is in the best scenario included by constants fitted with the experiment, otherwise neglected.

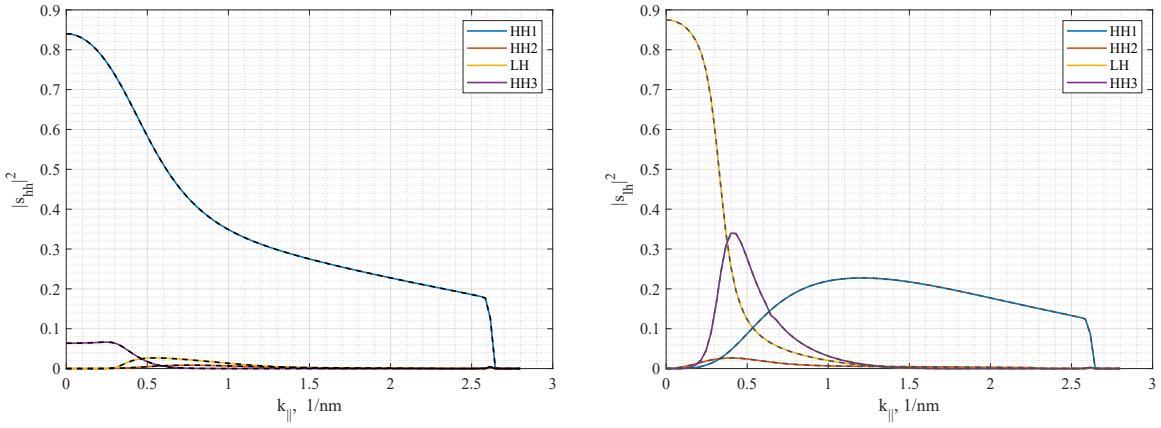

(a) Heavy hole contribution

(b) Light hole contributions

Figure 5.1: Contributions to HH and LH overlap integral s with the conduction band.

the energies (see fig. 4.1 and 4.3), and also the eigenfunction[15] does not change significantly upon choosing one matrix or the other, from now on only the upper matrix will be always considered.

Fermi factor

The term $f_{c,h}$ in eq. 5.1 is generally written as, for stimulated emission,

$$f_{c,h} = f_c + f_v - 1 \tag{5.8}$$

assuming then the distributions to be Fermi function, the expressions for the electrons and holes distributions become

$$\begin{aligned} f_c^{lc} &= \frac{1}{1 + e^{\frac{E_c^{lc} - E_{fc}}{k_b T}}} \\ f_v^{lv} &= \frac{1}{1 + e^{\frac{E_v^{lv} - E_{fv}}{k_b T}}}, \end{aligned} \tag{5.9}$$

where E_{fc} and E_{fv} are the Fermi energies respectively for the selected conduction and valance band. To compute these values it is important to recall, considering for example the conduction band, that the total density of electrons is given by

$$n = \sum_{k_{\parallel},\eta,lc} f_c^{lc}. \tag{5.10}$$

[15] By seeing that that the overlap integrals for the lower and upper case are equal, the similarity between the wave-functions is thus proven by induction being s obtained by the combinations of such quantities.

In the continuum limit the sum over $k_\parallel$ becomes an integral and previous equation can be expressed as

$$n = \sum_{lc} \frac{2}{(2\pi)^2} \int_{k_\parallel} f_c^{lc} k_\parallel dk_\parallel, \tag{5.11}$$

that is computed over the all sub-bands, in the case of conduction band, only one sub-bands is present and so the sum is not important.
E_{fc} is then computed by choosing an appropriate electron density[16], and finding the value for E_{fc} that minimizes the difference $n - \sum_{k_\parallel,\eta,lc} f_c^{lc}$. The same procedure is followed in the case of holes using the related VB sub-bands and holes densities.
For the following simulation, the chosen electron density is equal for both holes and electrons, $n = p = \frac{4{\cdot}10^{12}}{cm^2}$[17]. Figure 5.2 shows the sum of the conduction and valance band Fermi function. Again the four contributions from the VB sub-bands are displayed. It is clear that HH_1 has the largest impact on the final result, being the band closer to CB, it is where most of the transitions will be possible. All other transitions for f_v are negligible, as it is possible to see from the f_c curve representing only the Fermi function of the CB. In fact to have the curve coincident to f_v means that f_v from HH_2, but especially LH and HH_3 is zero.

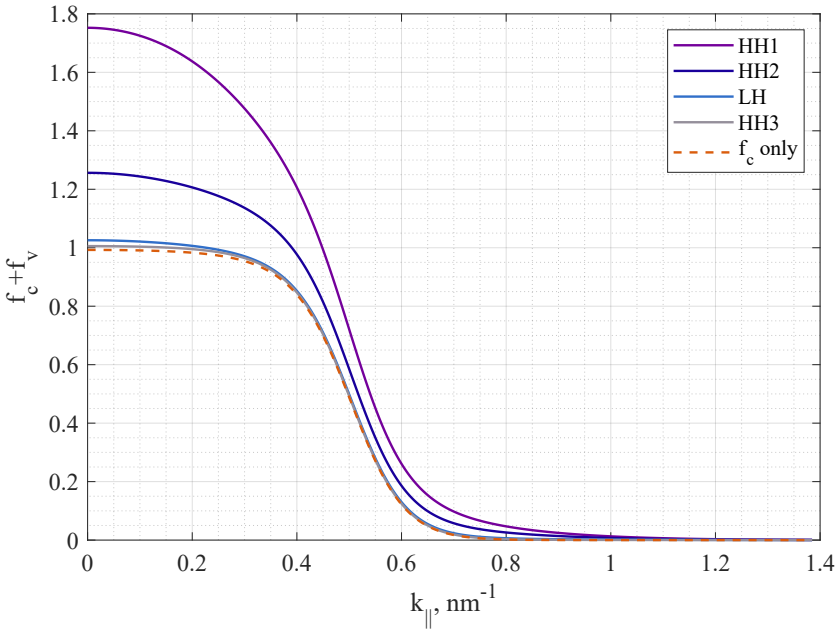

Figure 5.2: Sum of Fermi functions for electron and holes.

On the other for spontaneous emission the expression for $f_{c,v}$ is

$$f_{c,v,spo} = f_c \cdot f_v, \tag{5.12}$$

[16]This is one of the input that are given to the program in order to compute the gain and other quantities.

[17]Thus the carrier density N defined in Chapter 2, is now referred as n

which can be retrieved by manipulating eq. 5.8 in order to isolate the term related to a photon emission. Namely,

$$f_{c,h} = f_c + f_v - 1 = f_c \cdot f_v - (1 - f_c)(1 - f_v), \tag{5.13}$$

where the first term gives a non zero value when both conduction and valance band are occupied (a photon must be emitted and not absorbed to have spontaneous emission).

Lineshape

Lastly the term L from eq. 5.1 is defined as Lineshape and takes into account the broadening of energies due to intraband relaxation time τ_{in} and non-Markovian scattering eventτ_{nm} . Generally it is defined as[36]

$$L(\hbar\omega - E_{c,v}) = \int_{-\infty}^{\infty} D_c(E) D_v(\hbar\omega - E - E_g) dE, \tag{5.14}$$

where D_c and D_v are the energy spectra of electrons and holes in conduction and valance sub-bands, thus with energy $E_{c,v}^{lc,lv}$.Eq. 5.14 can be approximated in different ways. The easier one has a the Lorentzian shape in which the scattering is threaten only has a constant term τ_{in}. By doing so the integral is easily solved giving

$$L_{lor}(\hbar\omega - E_{c,v}^{lc,lv}) = \frac{1}{E_{c,v}^{lc,lv} - \hbar\omega - i\gamma_0}. \tag{5.15}$$

The previous expression is useful to understand that $\Delta\epsilon(T, \omega, n)$ is ca complex number. If this would not be possible, the total gain of the system would be zero since both Gain and spontaneous emission are related to the imaginary part of the dielectric constant.
Apart from this, the used [1] lineshape is based on including also non-Markovian [37] effects, i.e those processes with a finite time actions and not instantaneous. Here eq. 5.14 can be solved by expanding in continued fraction. In other words fixing a maximum number of expanded fractions N_{nMk}, the broadening function is constructed by following the algorithm

$$L_{nMk,j-1} = \frac{1 - \frac{\gamma_0}{\gamma_{nm} L_{nMk,j}}}{\frac{1}{\gamma_{nm}}(E_{c,v}^{lc,lv} - \hbar\omega - i\gamma_0) + j} \tag{5.16}$$

meaning that, starting from the maximum element

$$L_{nMk,N_{nMk}} = \frac{1}{\frac{1}{\gamma_{nm}}(E_{c,v}^{lc,lv} - \hbar\omega - i\gamma_0) + N_{nMk}}, \tag{5.17}$$

the final one is retrieved by descending down to $j-1 = 0$. γ_{nm} refers to the non Markovian scattering rate.
Lastly the final Lineshape is thus written as $L = \frac{L_{nMk,N_{nMk}}}{\gamma_{nm}}$.
Figure 5.3 shows a comparison between the real and imaginary part of the lineshape considering again HH and LH bands, where the energy axis refers to. Here, for both

case, the different contributions from the sub-bands are clear: with increasing energy the deeper sub-bands will start giving contributions, although at very high energies the value of the lineshape is very small. The dotted line represent the lineshape retrieved by using eq. 5.15. In the real part case the decreasing is, as expected exponential and the non Markovian and Lorentzian lineshape coincide. While they differ for lower energies.

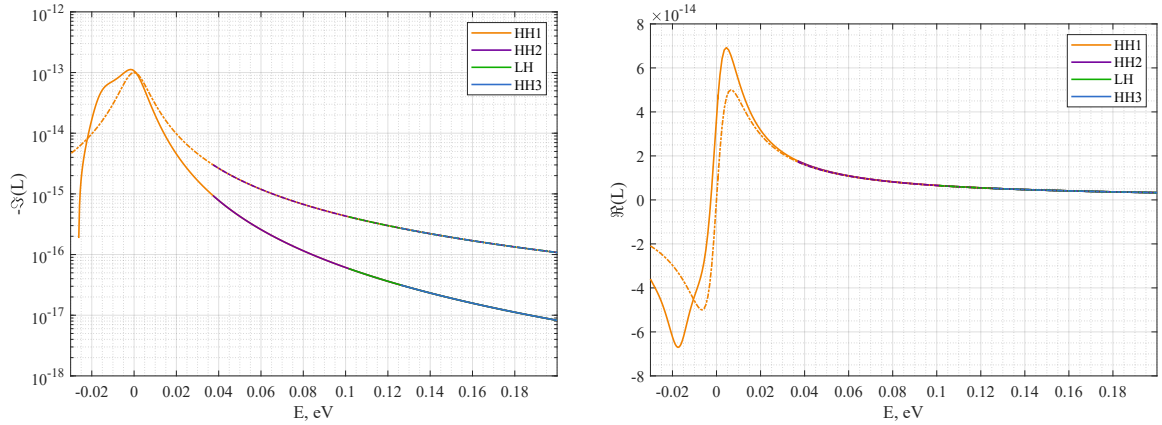

(a) Imaginary part

(b) Real part

Figure 5.3: Real and imaginary part of lineshape with non Markovian and Lorentzian (dotted line) formulation. Here $\gamma_0 = 10^{13} s^{-1}$ and $\frac{1}{\gamma_{nm}} = \tau_{nm} = 40 \cdot 10^{-15} s$.

The inequality between the two formulation is very clear from the imaginary part where the non Markovian lineshape is, at maximum, two order of magnitude lower than the Lorentzian one.
Nonetheless, considering that the overlap integrals and Fermi distributions give the most contribution at lower energy (low $k_{\|}$), the huge difference at high energy can be neglected when discussing about the two shapes.
Now that all the terms of eq. 5.1 are known, we can directly compute the gain,spontaneous emission and the refractive index variation. However, it should be noted that in the previous expression the so called Coulomb interaction between carriers (Many body effect) has been included.

5.2 Many body effects

The Coulomb interaction between carriers leads to the formation of electron-hole pairs, called excitons. Due to their bound nature, the actual transition energy from CB to VB is lowered, leading to the beginning of absorption below the strained E_g[18]. At the same time the correlated movement of the electron-hole pair increases the transition probability from one band to the other. As a result such effect cannot be neglected, and in fact it has a very high impact on the laser gain. The reader is refereed to [21] for the full theory

[18] In reality below the 2D gap, i.e. the distance between the first CB sub-band and first VB sub-band.

regarding this effect.
The coulomb interaction can be included by defining a screening mechanism of charges in the well, in this way, especially at high carrier density, the actual Coulomb energy in the system is reduced and so the band gap changes. To account for this effect, first it is necessary to defined the valance and conduction unscreened potentials[19], under diagonal Coulomb approximation

$$\begin{aligned} V_c^{lc}(\boldsymbol{q}) &= \frac{e^2}{2\epsilon_0\epsilon_s \boldsymbol{q}} \int\int dz dz' |\psi_{T,lc}|^2 e^{\boldsymbol{q}|z-z'|} |\psi_{T,lc}|^{2^T} \\ V_v^{lv}(\boldsymbol{q}) &= \frac{e^2}{2\epsilon_0\epsilon_s \boldsymbol{q}} \int\int dz dz' |\psi_{T,lv}|^2 e^{\boldsymbol{q}|z-z'|} |\psi_{T,lv}|^{2^T} \end{aligned} \tag{5.18}$$

with $\boldsymbol{q} = \boldsymbol{k} - \boldsymbol{k}'$, where $\boldsymbol{k} = \boldsymbol{k}_{\parallel}$, the index is dropped here for clarity. ϵ_s, is the static semiconductor background permittivity. It takes into account all the electrons that are not included in the states of the sub-bands (core electrons) and that actually contribute in screening the Coulomb interaction too, the value of it depends on the concentration of In in the well[14]

$$\epsilon_s = 15.1 - 2.87x + 0.67x^2. \tag{5.19}$$

The double integral is carried along the whole QW structure where the break of symmetry s present (z direction).
The introduction of q factor is needed when speaking about potential since the Coulomb force itself between carriers depends on the distance between the two, in the present case the two considered electrons occupy have crystal momentum $\boldsymbol{k}$ and $\boldsymbol{k}'$.
Once the potential for each sub-band is known, the screened potential is obtained by performing

$$W_{c,v}^{lc,lv}(\boldsymbol{q}) = \frac{V_{c,v}^{lc,lv}(\boldsymbol{q})}{\epsilon_d(\boldsymbol{q})}. \tag{5.20}$$

$\epsilon_d(\boldsymbol{q})V_{c,v}^{lc,lv}$ is the dynamic dielectric constant built from Lindhard formulation,

$$\epsilon_{D,c,v}^{lc,lv}(\boldsymbol{q}) = 1 - V_{c,v}^{lc,lv} \sum_q \frac{f_{c,v}^{lc,lv}(\boldsymbol{k}-\boldsymbol{q}) - f_{c,v}^{lc,lv}(\boldsymbol{k})}{E_{c,v}^{lc,lv}(\boldsymbol{k}-\boldsymbol{q}) - E_{c,v}^{lc,lv}(\boldsymbol{k})}, \tag{5.21}$$

where all the quantities are defined in the previous sections. The introduction of the screening makes the divergence for $q = 0$ presents in the unscreened potential disappear, thus avoiding infinite value in the numerical calculation. For such purpose eq. 5.21 is re-written through the radial approximation of the integrals involved (the sum over k can be extended to the continuous limit as shown in eq. 5.11) and solved for each sub-bands of the valance and conduction band. Figure 5.4 collects the result with the unscreened potential. It is evident that, upon the application of the screening, the actual potential

[19]To follow the same notation of [21], here we denote with V the potential energy related to the electrons and holes in the system. Moreover the indexes,m and n from Veprek are here neglected in order to simplify the notation (the physics is the same) and reduced at minimum the number of new used equations.

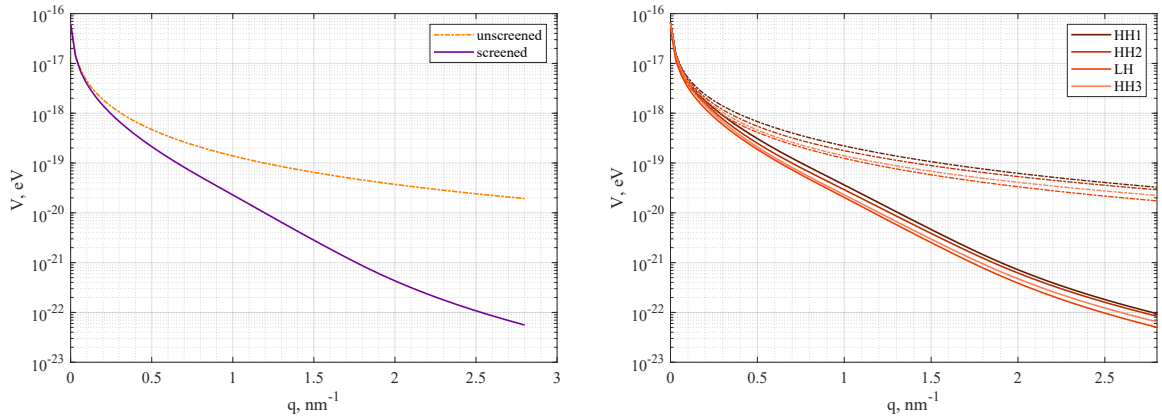

(a) Conduction band (b) Valance band

Figure 5.4: Conduction and valance band screened and un-screened (dotted line) Coulomb potential.

felt by electrons decreases. For very low $\boldsymbol{q}$ the screening is lower due to the divergent nature of the Coulomb interaction.
Now that the screened value is known, the energies from the sub-bands are corrected leading to an additional energy to be added to valance and conduction band. The shift is given by

$$\begin{aligned} \Delta E_c^{lc}(\boldsymbol{k}) &= \sum_{\boldsymbol{k}'} W_c^{lc}(\boldsymbol{k}-\boldsymbol{k}') f_c^{lc}(\boldsymbol{k}') \\ \Delta E_v^{lv}(\boldsymbol{k}) &= \sum_{\boldsymbol{k}'} W_v^{lv}(\boldsymbol{k}-\boldsymbol{k}') f_v^{lv}(\boldsymbol{k}') \end{aligned} \tag{5.22}$$

which can be solved again with radial approximation. It should be remarked that to solve this integral and the one of eq. 5.21, the Gauss–Legendre quadrature method is used [21]. Figure 5.5 shows the values of the shift. It is evident that for the CB and first sub-band the entity of the screened energy is not negligible, while for the other VB sub-bands the effect is lower due to the Fermi function $f_{v,c}^{lv,lc}$ being close to zero, see fig.5.2. The current simulation is performed for a relative high carrier density. Nonetheless a range of densities is required especially for the computation of the linewidth enhancement factor. Beside this, one expect the effect of Coulomb screening to be higher at higher densities due to the large number of charges able to screen the potentials. Figure 5.6 shows the CB sub-band (left) and first VB- sub-band (right), proves this assumptions. At low carrier density the effect of band-gap re-normalization is negligible, while for very high the shift hugely affects the sub-band energies.

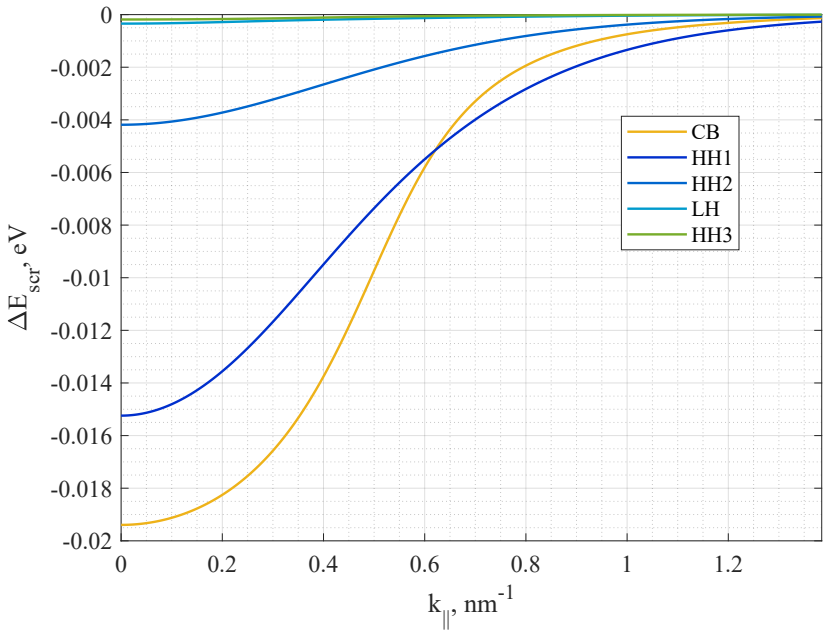

Figure 5.5: Energies shift from screened potential for CB and first VB.

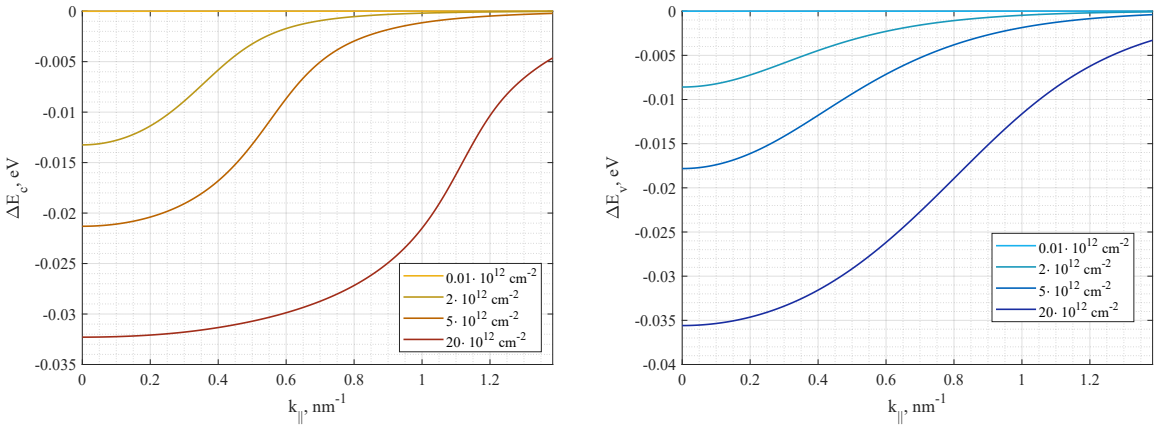

(a) Conduction band

(b) Valance band, HH_1

Figure 5.6: Energies shift from screened potential for CB and first VB sub-band for different carrier densities.

Summarising the previous result, the two shift are directly summed to all the previous energies $E^{lc,lv}c, v$[20], moreover such energies are also included in the determination of the Fermi energies E_{fc} and E_{fv}.
At this point all the physics necessary to reach results compared with the experiments [1] has been presented.

[20]Note that the simulation results of previous section has the many body effect included. This inclusion is especially relevant for the Fermi factors and Lineshape, which otherwise would look different.

5.3 Linewidth parameters

In this last section the physical quantities needed for linewidth computation are derived. The dependence on the temperature is included[21] in the energies, as done with the many body effect, through an empirical formula valid for the active region, so related to the $In_{1-x}Ga_xAs$ compound. It is written as [14] [1]

$$\Delta E_T(T) = \frac{\alpha_G T^2}{\beta_G + T} - \frac{\alpha_G T_{room}^2}{\beta_G + T_{room}}, \tag{5.23}$$

with $T_{room} = 300K$ and α_G and β_G are dimensionless constants depending on the Ga composition in the well, namely [14]

$$\begin{aligned} \alpha_G &= 6((1-x)^2 - 8.6(1-x) + 5.2)10^{-4} \\ \beta_G &= 337(1-x)^2 - 455(1-x) + 196 \end{aligned} \tag{5.24}$$

Being referred to 300 K, the effect of the temperature in this way is incorporated only when moving far from the reference temperature. Lastly $\Delta E_T(T)$ is subtracted to the conduction band energies and so included in the simulation. In addition, the value of λ is used as external input together with the carrier density. This term appears also in the $\hbar\omega$ which enters the total energy, eq. 5.14.

Gain

The first one is the gain of the Quantum well. Using the previously calculated $\Delta\epsilon(T, \omega, n)$ in the specific case of stimulated emission, we get to [34] [21] [33] [21]

$$G(T, \omega, n) = Y_{pp} k_0 \,\mathrm{Im}(\Delta\epsilon(T, \omega, n)), \tag{5.25}$$

where $Y_{pp} = \frac{4}{\epsilon_0 \epsilon_s 2\pi L_w \hbar}$ and $k_0 = 2\pi\sqrt{\epsilon_s}/\lambda$.

Figure 5.7 shows the obtained gain for different values of carrier density as a function of the wavelength, a wide range of wavelength is selected to show the behaviour which is consistent with [34][24][21][5] [4] and other.
The first thing to notice is the Coulomb screening in the system (dotted lines). By including it all the curves shift to higher wavelength as expected. In fact the actual band gap of the active region decreases due to screening effects and so the material starts lasing at larger wavelength since $\lambda \propto \nu^-1$ and $E \propto \nu$. As a result the maximum peak gain is very close to 1060 nm which is a very good result since poses the theoretical model in an environment close to the experimental case of emission at 1060nm. From the plot it is clear that the stimulated emission is not always permitted. For low frequencies

[21] Note that the temperature enters in the Fermi factors, so its effect is not trivial, here the correction to the energies is related again to the change in the band structure due to crystal lattice change with increasing or decreasing temperature.

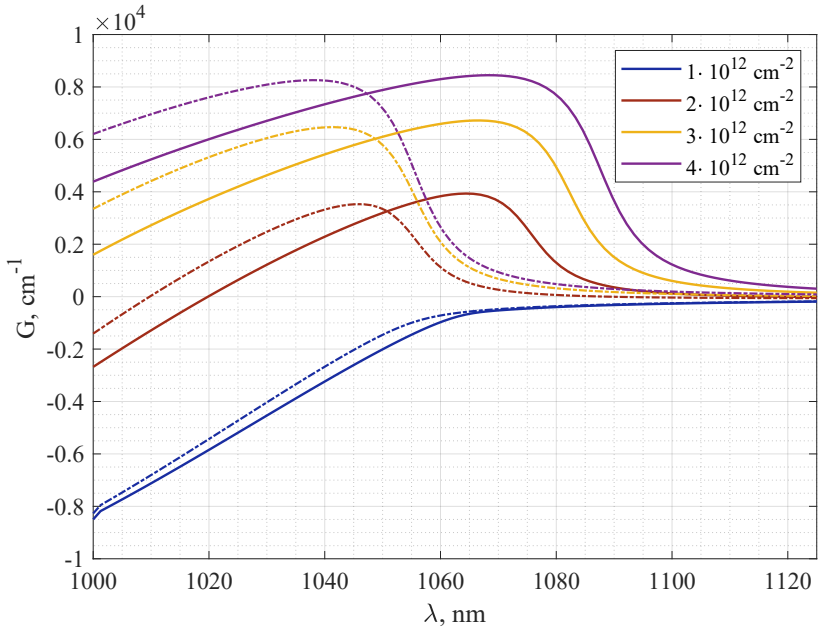

Figure 5.7: Gain vs wavelength for $T = 25°$ for different carrier density. The dotted lines are the simulation result without the inclusion of many body effects.

(high lambda) the energy given by the photons is not high enough for an electron to be promoted to the band gap. While for too low values of λ, the excess energy is lost through heat and light causing an overall decrease in the gain performances. Lastly the carrier density must be sufficiency high in order to have enough electrons (and holes) to participate to the stimulated emission process .[22] The effect of the temperature can be seen in figure 5.8. Here the gain is plotted as a function of the wavelength by fixing the carrier density to $n = 2 \cdot 10^{12} cm^{-2}$. It is clear that with increasing temperature the overall gain decreases and shift towards right. A very simple explanation is that the band gap shrinks due to the dilatation of the crystal lattice and so the active region starts lasing earlier. This statement is also proven experimentally as it will be possible to see in the experimental part. Lastly figure 5.9 shows the gain versus carrier density for two different wavelengths. These are the minimum and maximum chosen wavelength, namely 1060 and 1069. The two values are chosen considering that from the experimental results the maximum and minimum wavelength shifts fall in this range. In this contest we clearly see that an increasing carrier density leads to an increasing gain as expected. The higher wavelength gives higher gains as expected by looking at figure 5.8.

[22] In particular it must be high enough to counter act the losses from radiative and non radiative recombination as explained in the rate equations 2.2 and 2.3.

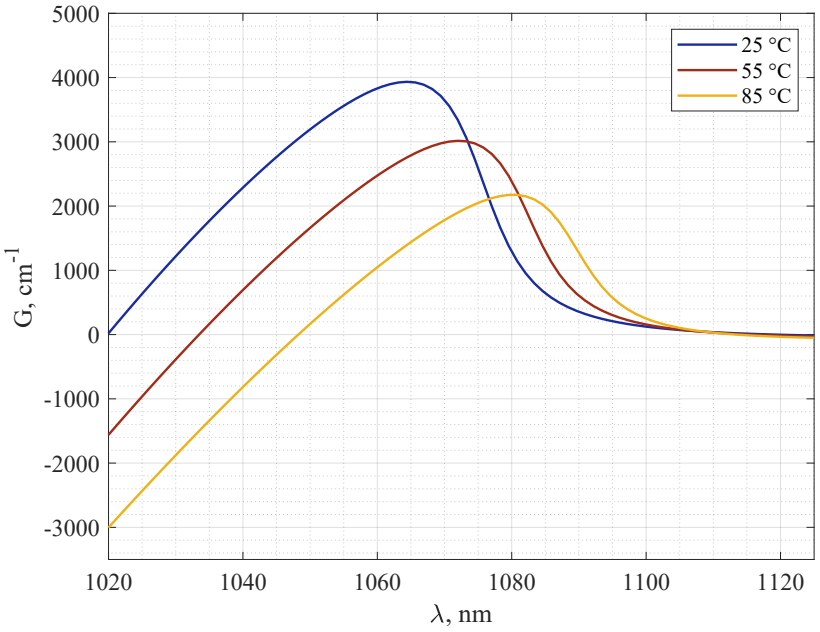

Figure 5.8: Gain vs wavelength for three different temperature, $n = 2 \cdot 10^{12} cm^{-2}$

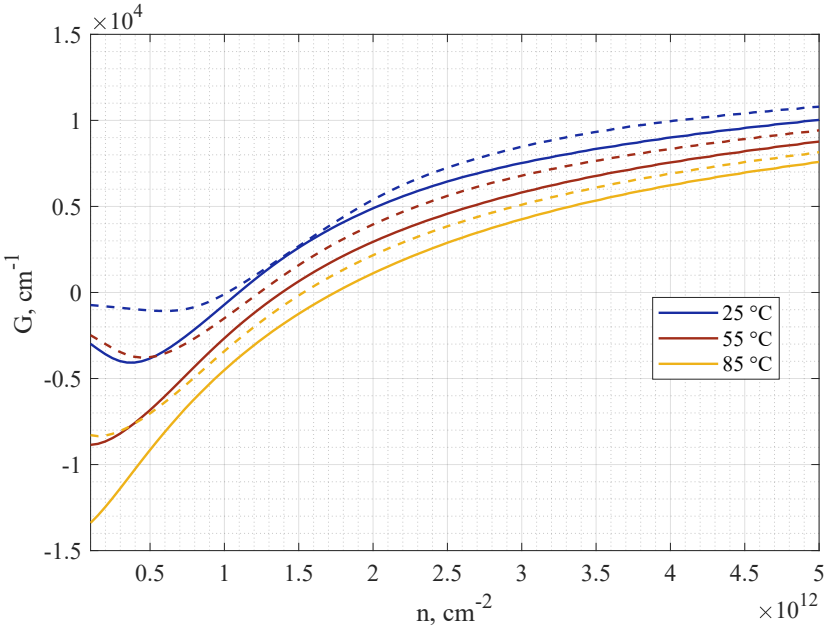

Figure 5.9: Gain vs carrier density for $\lambda = 1060nm$ and $\lambda = 1069nm$ (dotted line) for different temperatures.

Spontaneous emission

The spontaneous emission is obtained by using the related terms developed in the previous chapters, namely eq. 5.12 for the Fermi distributions, and eq. 5.7. Inserted in the dielectric constants 5.1 and labelling it as$\Delta\epsilon_s$. Using this the spontaneous emission is obtained as

$$E_s(T,\omega,n) = Y_{pp}k_0\frac{c}{\sqrt{\epsilon_s}}\,\mathrm{Im}(\Delta\epsilon_s(T,\omega,n)). \tag{5.26}$$

It is interesting to plot the spontaneous emission versus wavelength for low carrier density. Figure 5.10 shows this aspect for $n = 1\cdot 10^9 cm^{-2}$. The obtained figure is what is called

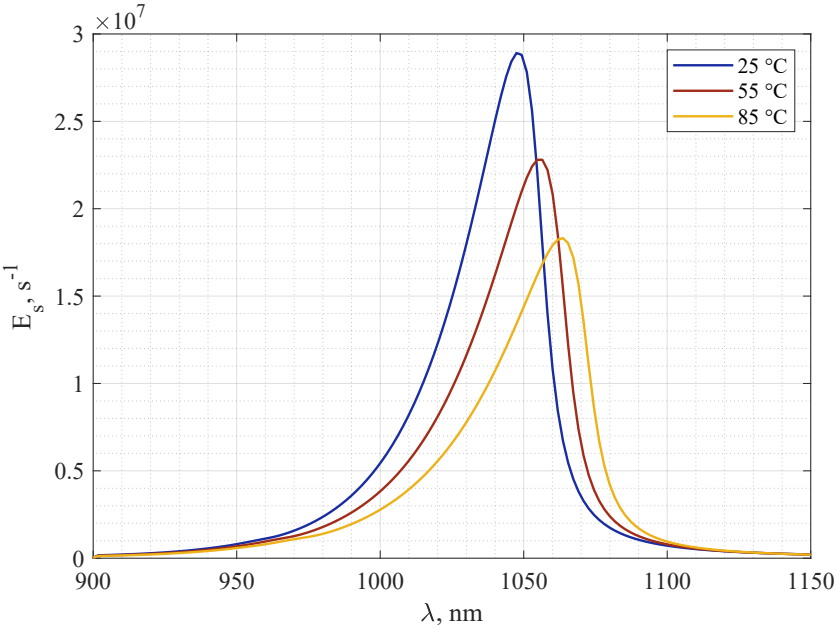

Figure 5.10: Spontaneous emission vs wavelength for different temperatures,$n = 1\cdot 10^9 cm^{-2}$.

as photoluminescence peak. At low densities it is dominated by the ground states and the influence from other deeper sub-bands is not present. The plot is thus useful to detect the the peak light intensity at which the material is able to emit for a certain wavelength. Indeed this quantity in particular is what has been chosen in order to find a proper quantity for the concentration of Ga in $\mathrm{In}_{(1-x)}\mathrm{Ga}_x\mathrm{As}$. From the figure in fact we note how the peak wavelength is approximately 1050 nm at $25°C$. It increases again with increasing temperature. Additional peaks from higher sub-bands transitions may appear as the carrier density or lattice temperature are increased as these states get more and more populated. Indeed from the $85°C$ it is possible to notice that the curve is wider.
The effect of increased Temperature and carrier density can be clearly seen in figure 5.11. The dotted line representing the maximum frequency as in the case of the gain. The behaviour again is expected as an higher carrier density will likely contributes more to the spontaneous emission rate. Higher wavelength is related to higher emission as it

happens with the gain. Nonetheless it is interesting to notice the crossing between 1060 and 1069nm, with increasing temperature it appears more evident. Such effect is related to the non-linearity in the spontaneous emission when the peaks in figure 5.10 gets wider.

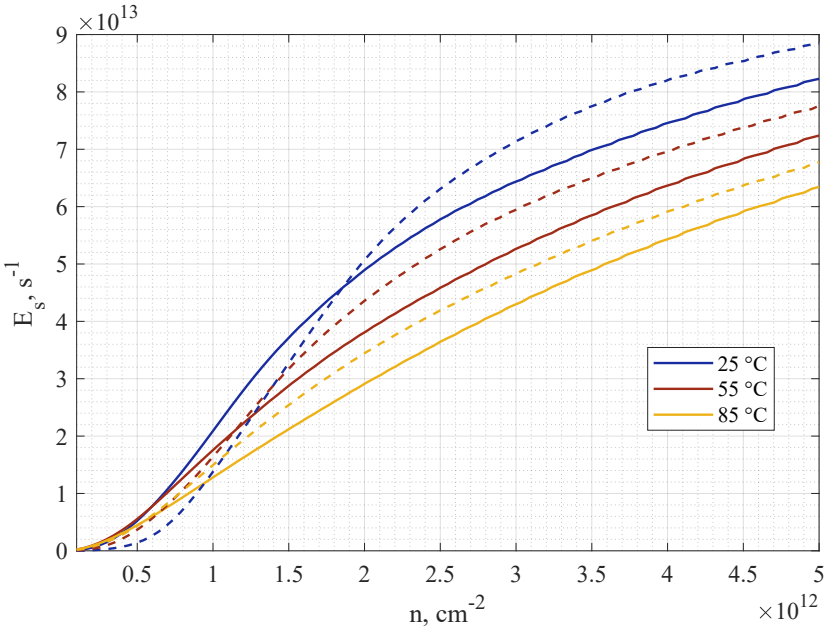

Figure 5.11: Spontaneous emission vs carrier density for wavelengths $\lambda = 1060nm$ and $\lambda = 1069nm$ (dotted line) for different temperatures.

Refractive index

The refractive index change in the active region due to carrier density, Temperature and wavelength changes is computed in a relative way as

$$\frac{\Delta n_r(T,\omega,n)}{n_r} = -\operatorname{Re}(\Delta\epsilon_s(T,\omega,n)), \tag{5.27}$$

whose expression can explained easily considering that the complex permittivity can be divided in a real and imaginary part. While the latter is related to absorption (and thus gain and spontaneous emission), the real part is commonly referred to the refractive index of the material.

Figure 5.12 shows the relative refractive index for different carrier densities and temperature. The order of magnitude is similar to [34], here the range of wavelength makes it possible to notice different effects in the overall shape. For low wavelength (very high energies) the refractive index variation is positive, while after around 100 nm it becomes negative. With increasing carrier density a second minima appears and is shifted towards right as the density grows. Lastly the values return towards zero for increasing values. Such a complex behaviour is probably related to the real part of the lineshape which

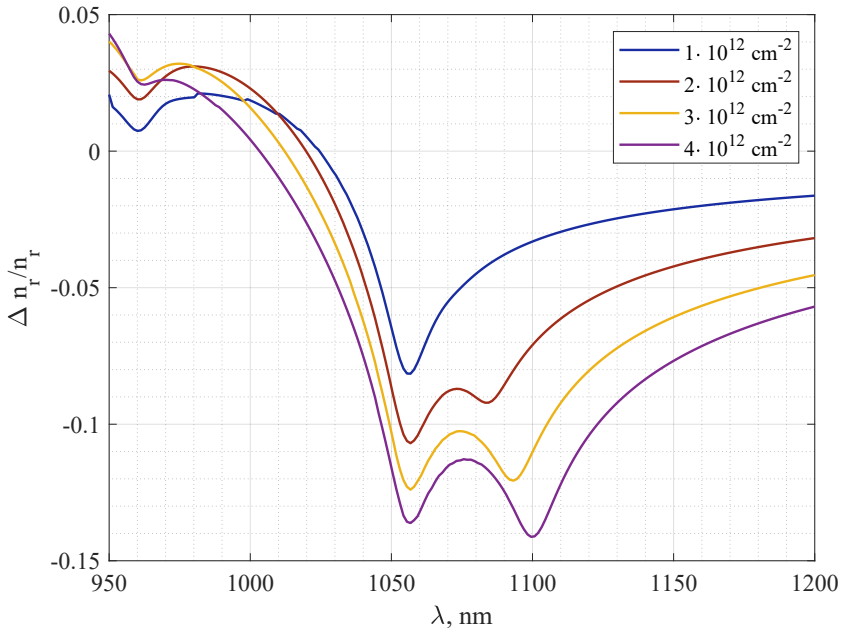

Figure 5.12: Relative refractive index vs wavelength for different carrier density at $T = 25°$.

exhibits a non linear behaviour, see figure 5.3. Even in this case we see that higher densities increase the magnitude of the change in refractive index. With the above statement clearly visible in figure 5.13. What is peculiar in this case is that, mainly for the higher temperature, the two different wavelength gives a non-negligible difference. Such a result is related to the fact that in the range of the chosen wavelength, the relative refractive experiences fast changes.
This effect is so relevant that, for high carrier densities, at $1060nm$ the curve is always lower with respect to the one at lower temperatures: while for $1069nm$ it has the higher values (in modulus).

Linewidth enhancement factor

The last needed quantity for linewidth computation is the linewidth enhancement factor α, to retrieve it the most general definition is used:

$$\alpha(T, \omega, n) = \frac{4\pi}{\lambda} \frac{\frac{dn_r}{dn}}{\frac{dG}{dn}} \tag{5.28}$$

with $\frac{dn_r}{dn} = \frac{d\Delta n_r}{dn} \cdot 2\sqrt{\epsilon_s}$. Since both gain and refractive index are highly non linear, the expected outcome will share this propriety. Figure 5.14 shows $|\alpha|^2$ for different wavelength at different n. The first to notice to notice is that for the lower carrier density, after $1070nm$ α is constant as a reflection of the low-changing behaviour of the refractive index (see figure 5.12) and the gain close to zero (5.7). On the other hand for the remaining densities, $|\alpha|^2$ shows peaks whose reciprocal distance is proportional to the increase in

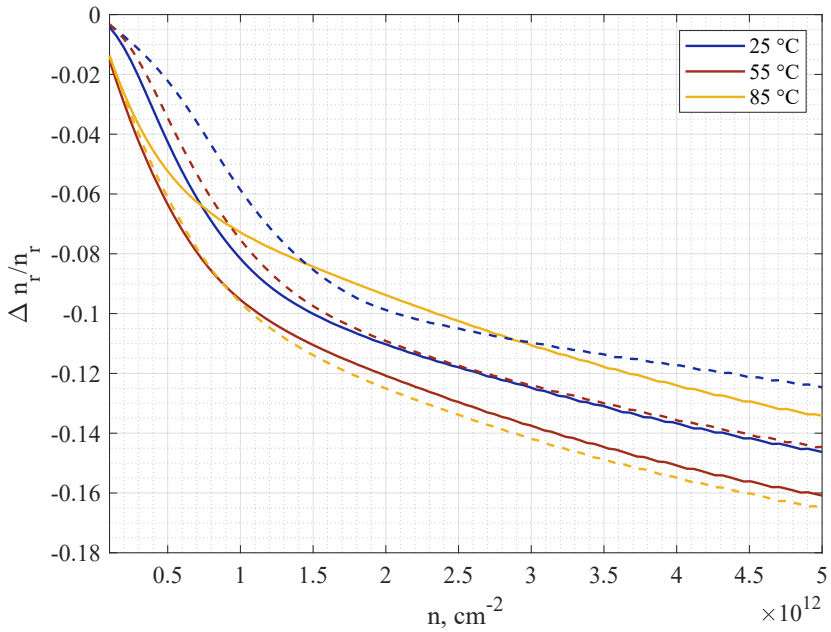

Figure 5.13: Relative refractive index vs carrier density for wavelengths $\lambda = 1060nm$ and $\lambda = 1069nm$ (dotted line) for different temperatures.

carrier density. These peaks take very high numbers that could cause an increase of the final linewidth of more than 100 times.

The latter especially relevant for intermediate carrier densities as depicted in figure 5.15. To explain this we may relate it to the fact that at those values os carrier densities, detrimental effects such as scattering and non-Markovian effects plays a huge role in the system noise. Such effects are not accounted in the spontaneous emission rate, but particular of laser semiconductor as explained in Chapter 2.

The effect of the temperature here makes $|\alpha|^2$ shifts towards right, this is actually a detrimental effect for our work since the involved carrier densities are usually not too low.

Lastly , for high densities it is clear that $|\alpha|^2$ plays almost no role in defining the linewidth of the laser, since the relevant term, eq. 2.18 is $1 + |\alpha|^2$.

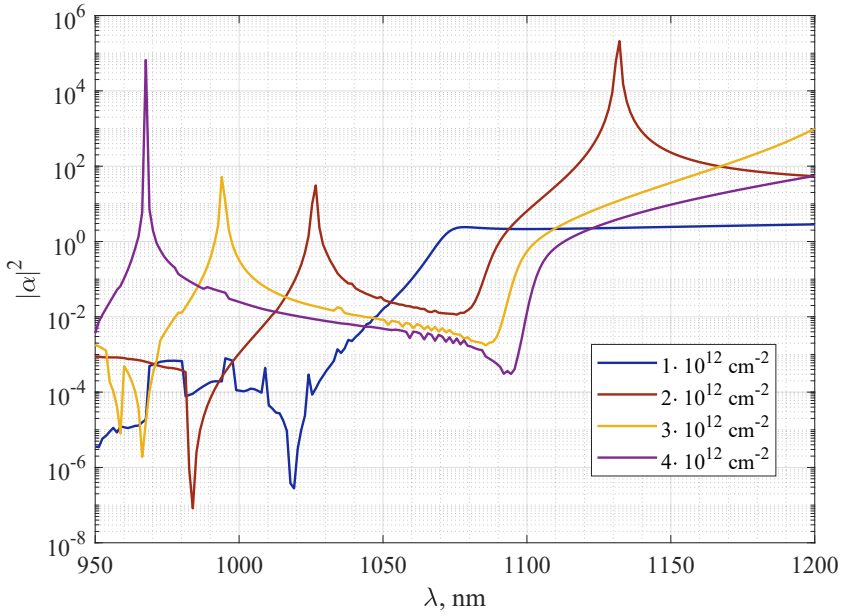

Figure 5.14: $|\alpha|^2$ vs wavelength for different carrier density at $T = 25°$.

5.4 Theoretical part: conclusion

With the inclusion of the strain in the **k·p** method and the Model Solid Theory for the strained band diagram, the QW active region has been successfully analysed. Many non-linear effects were thus added to better describe the physical processes involved. Many figures where included to give different hints on even more accurate description of the physics behind the simulations. Lastly all the needed quantities for the normalized linewidth coefficient where obtained in a large range of values of carrier densities, wavelength and for the three working temperatures.

The model is thus ready to be compared with the measurement performed at Chalmers by proper fitting of the operating wavelength and other constants such as the mirror losses and threshold gain.

The next experimental part is devoted not only to this aspect, but also to a more general description of the VCSELs in order to give a complete view of the device different designs impacts on the linewidth and output powers.

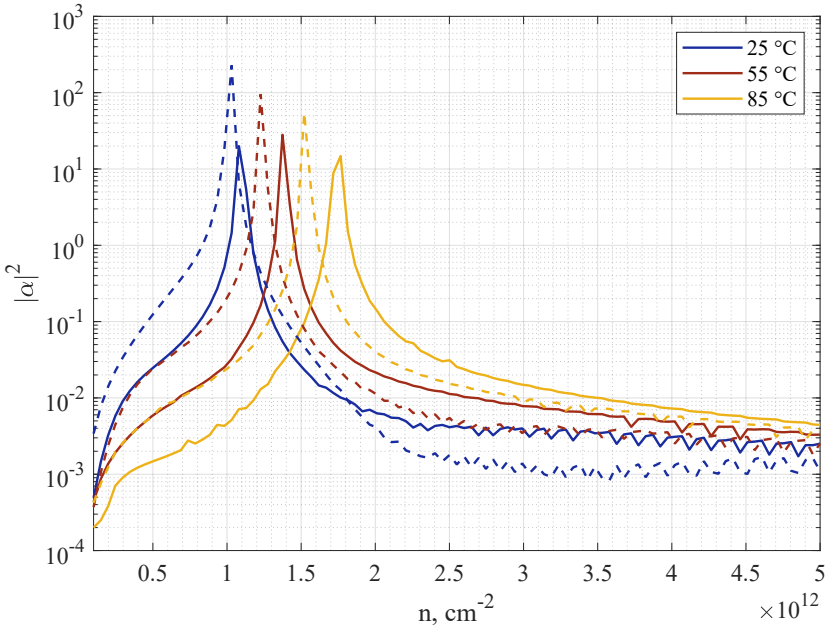

Figure 5.15: $|\alpha|^2$ vs carrier density for wavelengths $\lambda = 1060nm$ and $\lambda = 1069nm$ (dotted line) for different temperatures.

Part II

Experimental part

Chapter 6

IPV and spectrum

6.1 Introduction

The experimental part has been carried out in the Photonics Laboratory at Chalmers. Here the first main task was to select the VCSELs upon which performing linewidth measurement. To do so the spectrum and IPV characterization were performed. In this chapter the studied VCSELs are presented and the related measurements included.
Nonetheless before starting, it is necessary to describe the basic VCSEL top view in order to understand components such as the probe used to inject current.

Top view

Figure 6.1 shows the top view of a VCSEL seen through a microscope. The two numbers on the top are used to denote where the selected VCSEL is located. In fact when realized, VCSELs are growth starting from a common substrate, so a single chip may contain hundred of these lasers organised as a matrix. For this reason the number on the left indicates the column, while the one on the right the row the VCSEL belongs to.
Another important aspect is given by the three pads. The central one is connected to the top ring and so we refer to it as S (signal) pad. while the other two are ground pads connected to the n-contact and collect the current, therefore they are labelled as G (ground). The usage of pads are required in order to bias the VCSEL without damaging the small structure.

6.2 VCSELs category

The studied VCSELs are all single-mode 1060nm VCSELs and can be divide in two main categories: D1 and D2 VCSELS. All the studied lasers have an anti-phase design, the SR was not implemented since the Ion milling used to etch the circle part is difficult to control. Rather a total etching of the mesa surface is performed to reach better performances

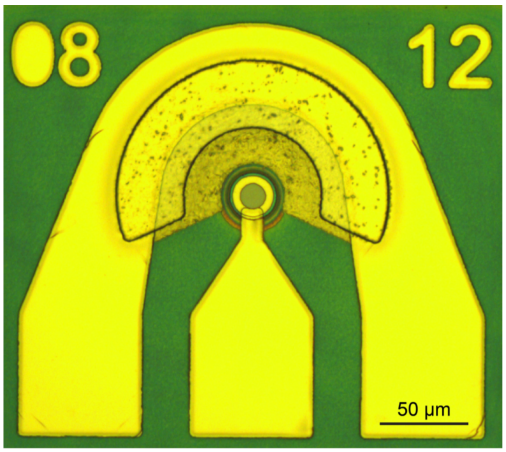

Figure 6.1: General VCSEL top view obtained with a microscope, from [41].

(different slope efficiency), figure 2.2 resembles how the general structure of the VCSELs are when probing.

D1

The first one refers to small oxide aperture VCSELs where the diameter of oxide aperture usually ranges from 2.1 to $3\mu m$. A peculiarity of this kind of devices is that the oxides are not placed close to the quantum well, rather additional layers are present. Such design is said to be weakly carrier confined, which means that the injected current from above the VCSEL is more subjected to spreading below the oxides.

D2

The D2 VCSELs are the commonly used VCSELs for communication operations [10][42]. Here the oxide aperture is usually around $4\mu m$, thus the structure is larger and presents more layers than D1. Here the oxide aperture layers are placed very close to the active region leading to an higher confinement of the current in the QWs avoiding lateral spreading[43]. Such design is called strong carrier confinement, which leads to a gain being more mode selective with the main contributions coming manly from the fundamental mode. The oxides forming this type of VCSELs are thinner with respect to D1, this,in conjunction with putting the oxide apertures at optical field nodes[10], reduces the strength of the transverse index guiding. Making it possible to have the so called weak transverse optical guiding, which is used to reduce the number of active transverse modes, thus decreasing the spectral width and beam divergence. Thanks to this , single-mode VCSELs with large oxide apertures($> 4\mu m$) can also be fabricated.

D2: higher slope efficiency

The last third group of devices is devices almost equal to D2 design. The only thing that is different is the top layer etching. In these devices the etching depth is very low, this

makes it possible to have high slope efficiency, SE. The latter is defined as the slope of the curve obtained by plotting the output power from the VCSEL versus the current used to bias it. Figure 6.2 shows the slope efficiency vs etch depth for different devices. Here 91 refers to the D1 devices while 92 to D2. The orange lines indicates the tolerance in the chosen interval of values, this uncertainty is necessary since during the fabrication the epitaxial deposition of the layers is not completely precise. In addition different materials are deposited on the last layer of GaAs to protect the device, upon their removal some nm of GaAs layer is inevitable lost.

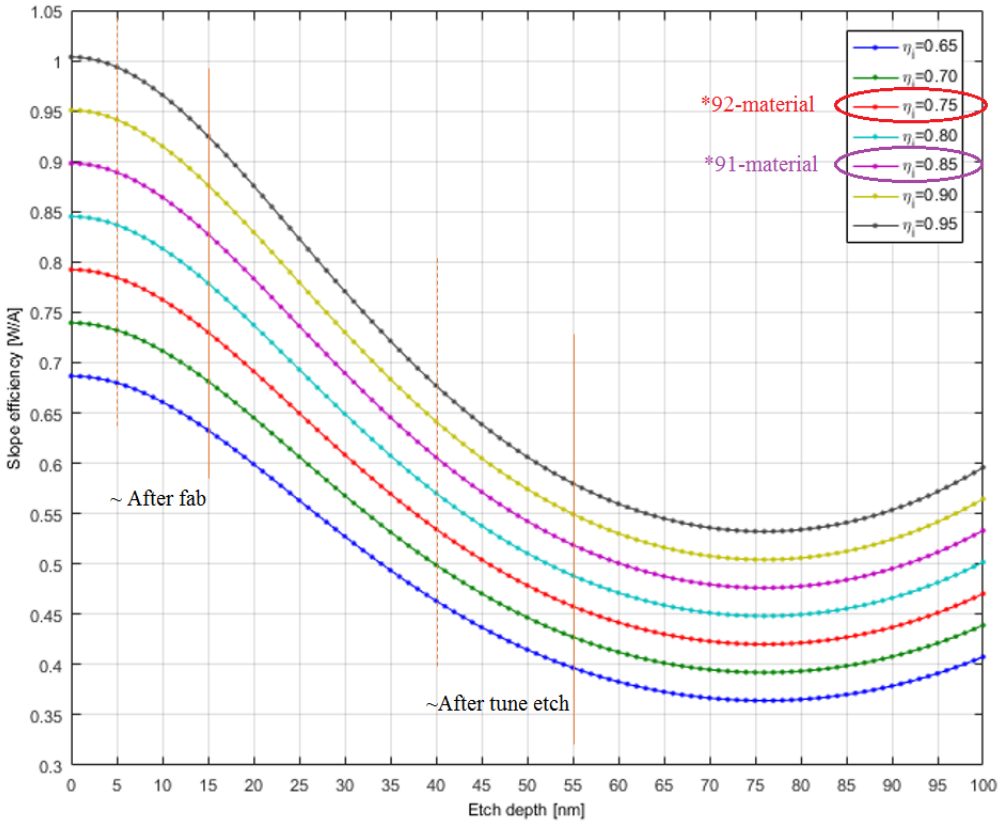

Figure 6.2: SE vs etch depth of the top layer, obtained with an effective index model used to compute the VCSEL optical losses [38][39], by courtesy of Johan Gustavsson.

Usually VCSELs are fabricated with a slope efficiency around $0.5\frac{W}{A}$ because this assures less reflection loss in the top DBR. So the mirror lets out less optical power and the photons stay longer in the cavity. Such design is also chosen since in small signal characterization the modulation response becomes more damped and the maximum 3dB bandwidth increases [10], which is a desired result in order to have the larger possible bandwidth for communication purpose. Thus by using an higher SE, the photon density in the centre of the cavity is lower with respect to the 0.5 case. This particular condition has been studied to see how and in what ways the performances of the VCSELs, especially the linewidth, are affected in comparison with D2 with the best SE. Thus the third type of devices is labelled as D2SE07, where the selected η is $0.75\frac{W}{A}$.

To summarise then three type of devices analysed in this experimental part are:

- D1: weak carrier confinement $\eta \approx 0.5\frac{W}{A}$.
- D2: strong carrier confinement with $\eta = 0.5\frac{W}{A}$
- D2SE07: D2 with $\eta = 0.75\frac{W}{A}$

Note that D1 has a η similar to D2 in order to see mainly the effects related to the different oxides and type of carrier confinements.

6.3 IPV

The IPV is often used as a static characterization tool for VCSELs. For a given injected current the voltage and output power are detected. In this way different important physical quantities of the VCSELs can be retrieved such as the threshold current and maximum output power.

IPV: set-up

Figure 6.3 shows the set-up used to measure the voltage and power from the selected VSCELs in red. All the used components are briefly explained here. The arrow in the figure shows if the related block is an input (arrow towards the experiment set-up) or output.

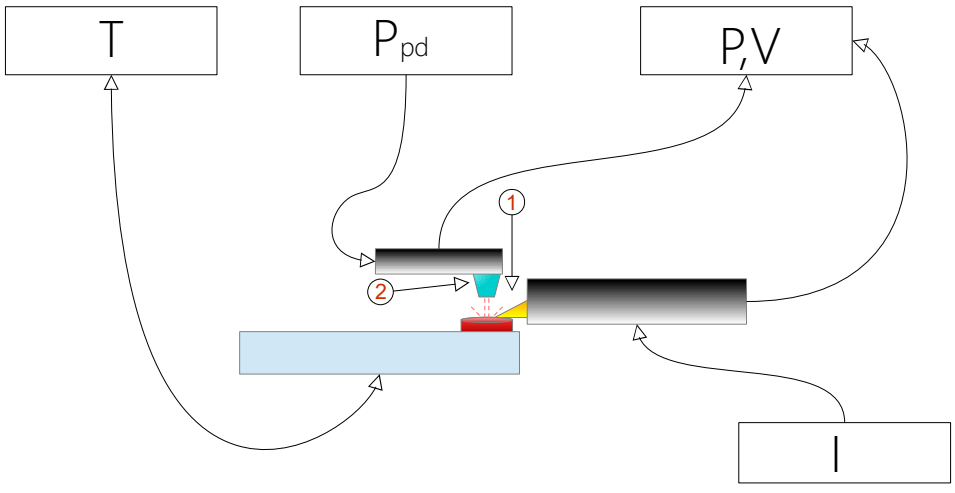

Figure 6.3: Simple sketch of the set-up for IPV measurements

- (1) is the probe used to inject current in the VCSEL and collect the output voltage from it. Two different type of probes are available in the laboratory: a GS (two contacts: ground-signal) and GSG (three contacts: signal-ground-signal) probe.

The main difference between the two is that with the second probe the positioning over the VCSELs's metal contacts is easier with respect to the GS case, which however can be used for smaller device. Another advantage of SGS probes is that the two ground extremities allows for precise field control of the central part[40]. For IPV measurements a GS probe is used.

- **I** denotes the current generator (*Yokogawa 7651 DC source*) used to bias the VCSEL. So for each injected current a value of voltage and power is retrieved. Here a fulfils this role.
- (2) is a large area silicon detector with diameter of the order of $1cm$ able to work at $1060nm$. Its position should be close to the VCSEL in order to capture the majority of the emitted light, which is then converted to electrical power.
- **Ppd** (photodiode) related the device used to turn on the detector generator used to bias the VCSEL. The voltage required is $0.24V$ and is provided by a voltage generator *Agilent E3631A*.
- **P,V** refers to the multimeter *Agilent HP 34970* used to collect output voltage and power of the VCSEL. To perform this task two different channels are involved.
- Lastly **T** stands for the temperature controller, its role is to select the desired temperature of the holder (copper) where the VCSEL lays. Thermocouples are present in order to measure and regulate the temperature and reaching a stable value, for this reason the temperature controller acts as an input/ouput block since the feedback from the holder is needed. The used component is a *Keithley 2510-AT*. It is useful to note that its stability in maintaining the temperature decreases with increasing temperature, at $T = 85°C$ a change of $1°C$ is usual present. While for room temperature[23] the oscillations are negligible.

Thus by sweeping through different currents the output voltage and power are recorded for each device belonging to the D1, D2 and D2SE07 categories. This task is performed with MATLAB thanks to the GPIB (general purpose interface bus) connection between all the instruments.

IPV: results

Figure 6.4 contains the approximated points where some physical parameters are calculated when the measurement is complete. The current generator stops increasing the injected current soon after the roll-over is reached, i.e. the point at which the power reaches its maximum, since above this limit the VCSEL could suffer irreversible damage due to to high currents.

[23]From now on the room temperature is set to $25°C$ which is not 300K. Such change of notification is considered in the simulations.

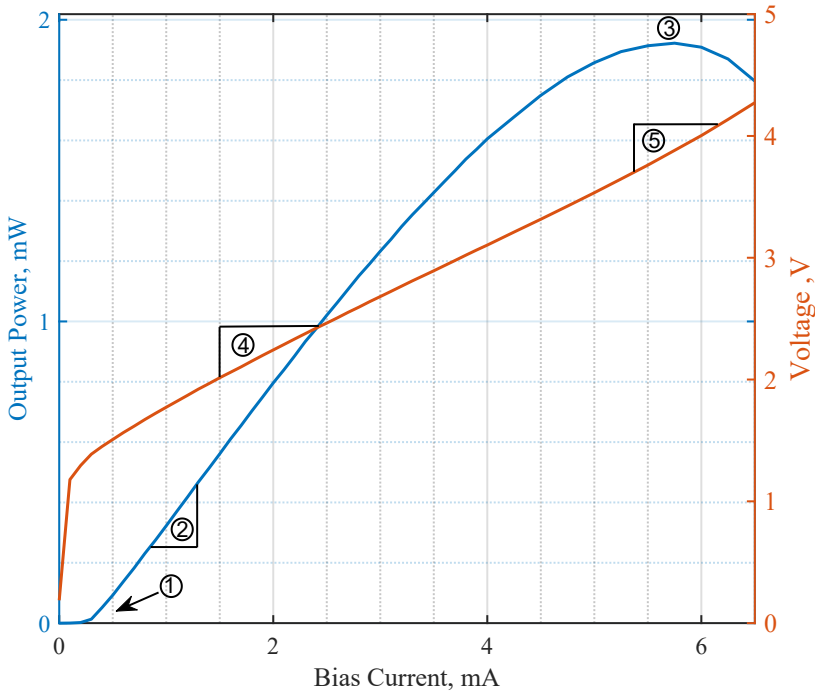

Figure 6.4: General IPV plot with marks on important figure of merit.

1. Threshold current (I_{th}). It is the current at which gain and losses in the system are almost equal, thus above this limits[24] the VCSELS starts lasing. It is clear that its value depends on the VCSEL design together with the temperature on the system. In fact if I grows, then also the losses that contribute to heat will increase, see rate equations and figure 2.3.

2. Slope efficiency (η). This quantity is obtained taking the ratio $\frac{dP_{out}}{dI_{bias}}$ close to the threshold current in order to limit the thermal effects being more relevant at higher T.

3. Roll-over (maximum) current, voltage and power. The point at which the power reaches its maximum. Here the maximum current and voltage are extrapolated as well. After this position the power decreases due to saturation and to high thermal effects.

4. Differential resistance (R_{diff1}). First differential resistance obtained by the slope of the straight line approximating a close range of output voltages values at half the maximum current, so generally $R_d = \frac{dV}{dI_b}$. As a first principle such resistance should contain the sum of all VCSELS resistances: DBR, oxide layers and also

[24] A numerical value is defined although the lasing does not starts exactly at this point, but the transition is continuous, i. e. when stimulated emission begins to overcome the spontaneous emission processes

active region.This however is not completely true since the resistances of the pads, probe and internal and external capacitance related respectively to the VCSEL and contacts makes the picture much more complex. Nonetheless the resistance can still be used to compare different VCSELs.

5. Differential resistance at roll-over (R_{diff2}). Second resistance calculated as the first one but this time at roll-over. Such difference is performed to see the effect of temperature and saturation on the output voltage.

Having established all the terms for IPV characterization. In the next pages the results form the measurement are collected for three different temperatures. Figure 6.5 refers to D1 VCSELs, 6.6 to D2, and 6.7 to D2SE07. In each plot the previously explained quantities are listed for a direct and easy comparison between all the cases.

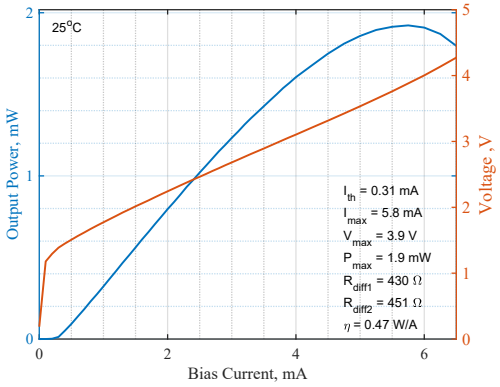

(a) $T = 25°C$.

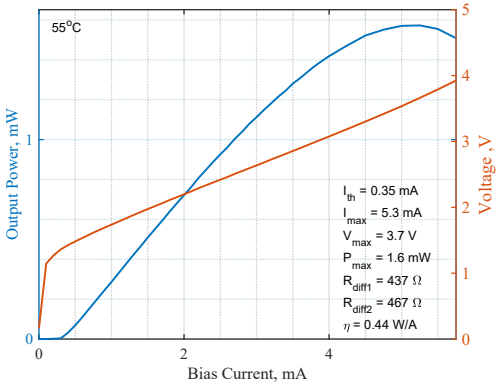

(b) $T = 55°C$.

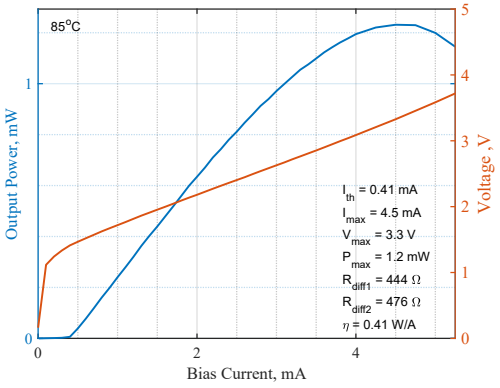

(c) $T = 85°C$.

Figure 6.5: IPV for D1 for three different temperatures.

Starting with D1, the chosen device has aηclose to 0.5. On the whole with increasing temperature all the different parameter get worse, due to higher losses by thermal effects. In

fact the threshold current increases and so the maximum current and voltage and power decreases. The trend is especially evident at $T = 85°C$ which represents a very harsh condition for the VCSEL working point. Having a lower I_{th} has consequences also on ηwhich decreases. Lastly the two resistances slightly increase meaning that the thermal effect plays a side role in the contribution to their value[25].

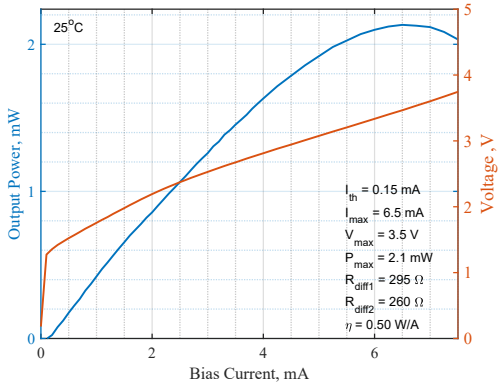

(a) $T = 25°C$.

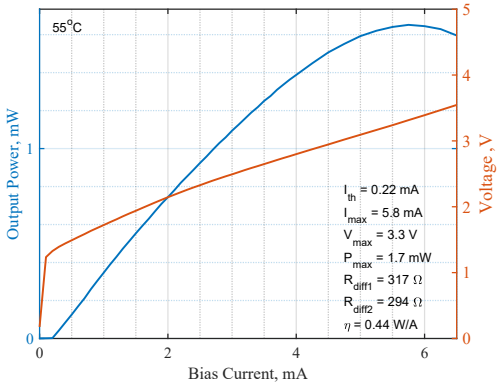

(b) $T = 55°C$.

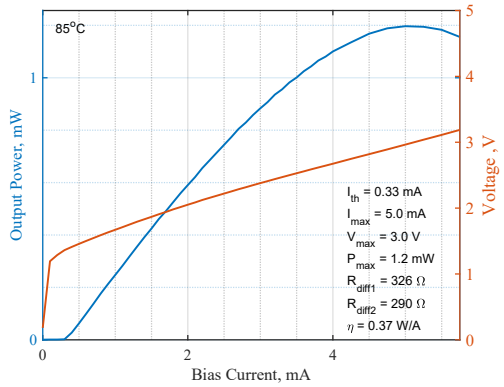

(c) $T = 85°C$.

Figure 6.6: IPV for D2 for three different temperatures.

Regarding D2, the first thing to be noticed is the overall better behaviour with respect to D1. In fact comparing figure 6.5 (a) with fig. 6.6 (a), the maximum power and current are larger. Moreover the maximum voltage is lower meaning that the VCSEL is capable of reaching better performances with almost the same output voltage of D1.
Continuing in the comparison, the differential resistances in D2 case are lower, in fact the oxides in the structure are thinner[43] (as a side effect the capacitance gets higher), but more importantly the D2 VCSEL has a bigger size, thus it has naturally a lower resistance

[25]In this contest the resistivity of the pads together with the probe increases with temperature being they made of metals, so also this contribution is present in the final measured resistance.

(banally since $R = \frac{L\rho}{A}$, with ρ being the resistivity and A the area, a larger oxide aperture can be associated to a lower resistance). Lastly the threshold current in the case of D2 is lower than in D1 meaning that the VCSEL is able to be turned on more easily. By this comparison it is already possible to know that we expect the overall linewidth of D2 VCSEL to be lower than in D1. In fact, with almost the same SE, the strong carrier confinement should make the active region more efficient in terms of stored carriers for stimulate emission process, while in the opposite case (D1) the spreading in the carriers cause more easily to have a return of an electron from an excited state to the VB without interacting with the sustained field in the cavity, in other words a spontaneous emission process becomes more probable.
Regarding the D2 behaviour with temperature, here we note also a decrease in the overall maximum parameters. While the threshold current at maximum temperature is more than twice the one at room temperature. Thus D2 devices behaves worst in term of relative change in the threshold current than D1. Likewise, η decrease in D2 is higher than in D1 .

Lastly in figure 6.7 the D2SE07 case is shown. Here the slope efficiency at room tem-

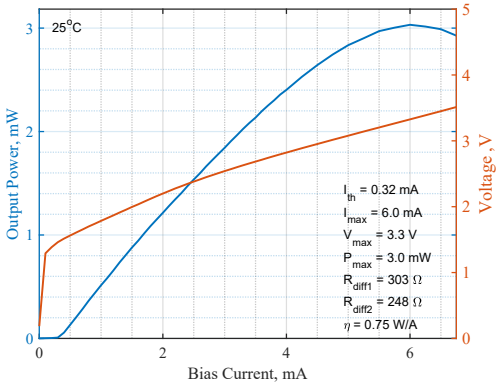

(a) $T = 25°C$.

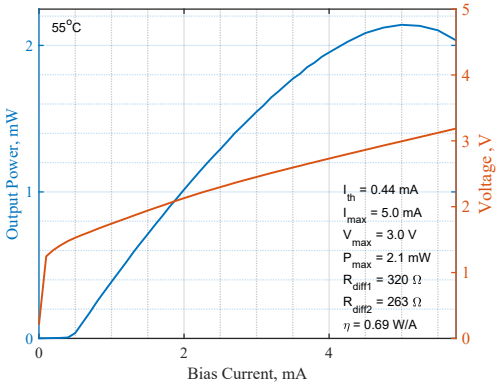

(b) $T = 55°C$.

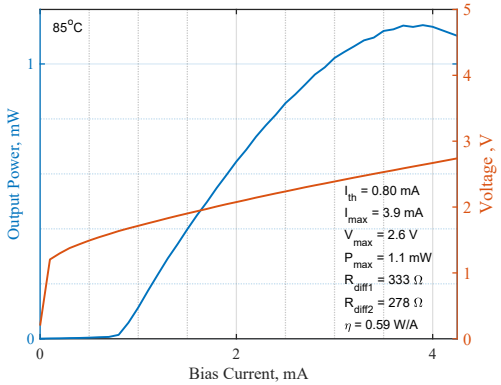

(c) $T = 85°C$.

Figure 6.7: IPV for D2SE07 for three different temperatures.

perature is very high as expected for this type of device. Comparing, for $T = 25°C$ with the D2, it is clear that the threshold current is higher together with the maximum power. This because with higher η, photons escapes from the cavity easier, thus the output power form the mirrors is higher than D2. But at the same time the threshold current, and so the injected carriers, needs to be higher to compensate the 'losses'[26] from the photons escaping the cavity. D2SE07 changes with temperature shows the largest increase in threshold current compared to the other two devices. Also the maximum power shares this record with a decrease of around $\frac{1}{3}$ the room temperature value. While the two differential resistance are similar to D2 confirming the similarities in the designs. On the whole both D2 and D2SE07 have a lower resistance with respect to D1, confirming what said about their dimensions. Figure 4.2 summarises the previous discussions on the different parameters dependences on temperature for each device.

[26]This type of loss is the one referred to stimulated emitted photons which contributes to the output power. The term loss is used to refer to them as no more present in the cavity.

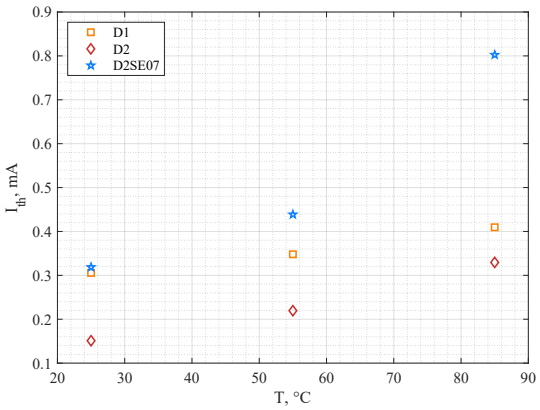

(a) I_{th}.

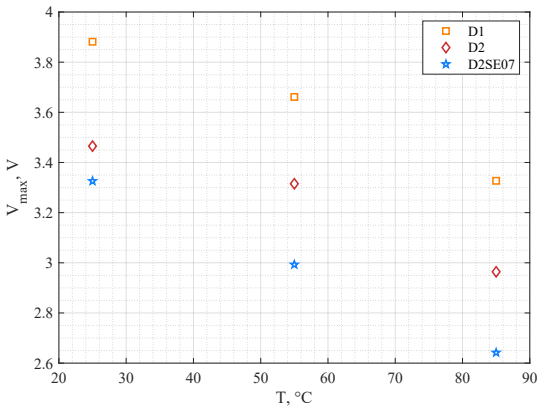

(b) V_{max}.

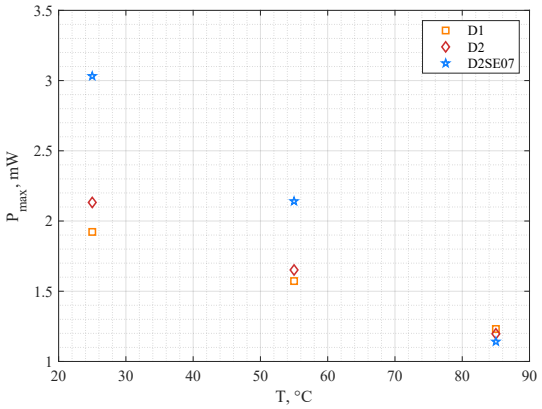

(c) P_{max}.

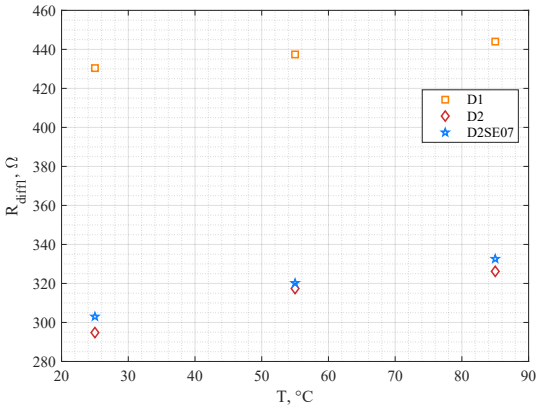

(d) R_{diff1}.

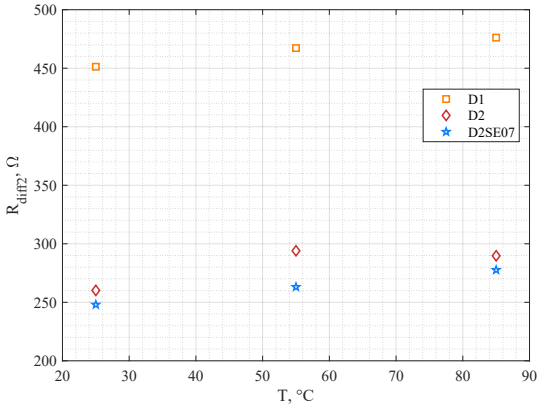

(e) R_{diff2}.

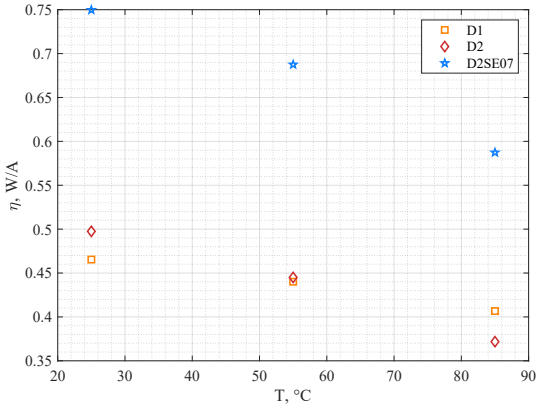

(f) η.

Figure 6.8: Measured physical quantites for $T = 25, 55$ and $85°C$ for all the three devices.

6.4 Spectrum

The second and fundamental way to characterize a VCSEL is by detecting its spectrum,i.e the range of wavelength in which the laser operates. This is important for two main reasons. The first one is to actually see if the VCSEL is single mode or not, while the second to see at what wavelength the fundamental mode lases and how it changes for different temperature and devices.

Spectrum: set-up

The set-up for spectrum measurements is quite similar to the one used for the IPV case. The probe, temperature controller, holder, current generator are exactly the same. Whereas the detector is replaced with a bare fiber connected with a *ANDO AQ6317 optical spectrum analyser* whose resolution is $0.02nm$. The usage of a fiber is allowed thanks to the great coherence of the laser output typical of a VCSEL [2] which, with the fiber close enough, couples with it and it is transmitted to the analyser. Figure 6.9 contains the set-up for the spectrum measurement, indeed this same configuration, except for the bare fiber, is the one that figure 6.3 derives on. A photo of configuration is included here for a complete description of the workbench used also for IPV measurement.

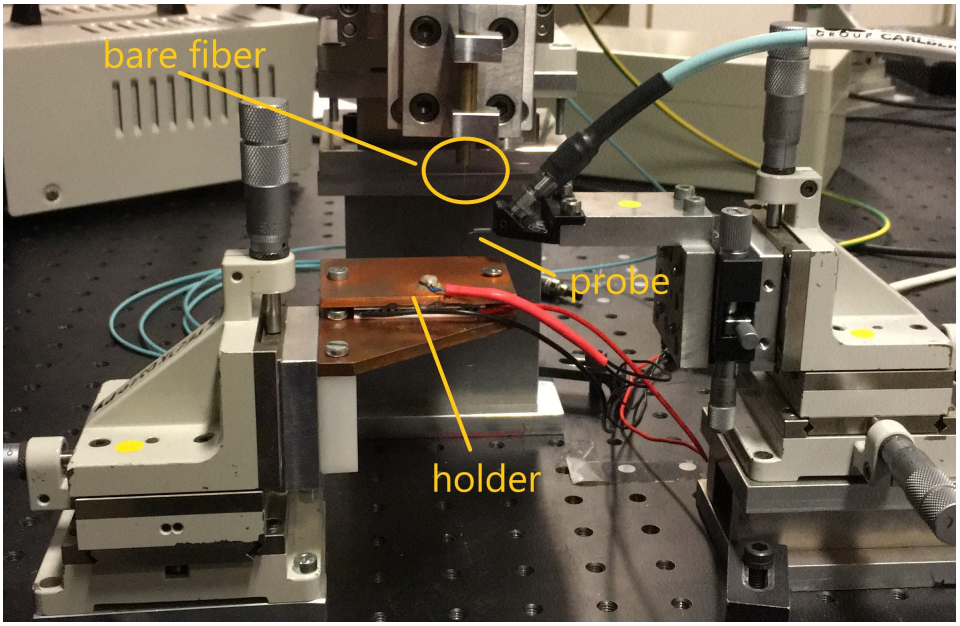

Figure 6.9: Photo of the set-up for spectrum measurement.

Spectrum: results

As done in the case of LIV, figure 6.10, 6.11, and 6.12 collects the spectra for respectively D1, D2, and D2SE07 for three different temperatures. In all the cases the bias current was fixed at $3mA$ in order to stay far from roll-over but with a reasonable high output power. In all figures the spectrum is plotted by considering the relative intensity with respect

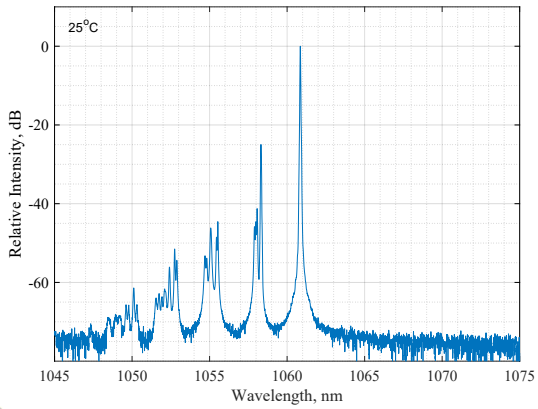

(a) $T = 25°C$.

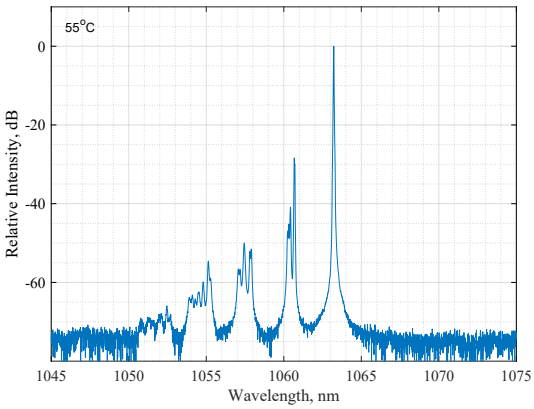

(b) $T = 55°C$.

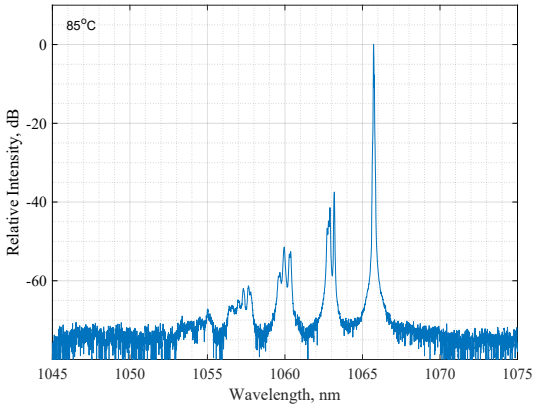

(c) $T = 85°C$.

Figure 6.10: Spectra for D1 obtained with $I_b = 3mA$ for three different temperatures.

to the maximum value. This correspond always to the fundamental mode, the closest sustained mode should often exhibits a relative intensity greater than $40dB$ (in modulus) to be considered sufficiently suppressed. In this way the device could be named as single mode. Unfortunately for D1, the suppression of the closest mode is around $-25dB$. Nonetheless for linewidth measurement this obstacle is partially surpassed thanks to the high precision of the chosen technique. For this reason D1 is considered to be single mode even if in reality it is not entirely true.

Considering (a) the higher peak is located as expected near 1061 nm. It is interesting to note the peak as a finite linewidth, however the instrument used for the measurement of the spectrum is not accurate enough to measure it, since it is supposed to be in the order

of magnitude of MHz[27]. In addition, considering for example $T = 25°C$, it is clear that

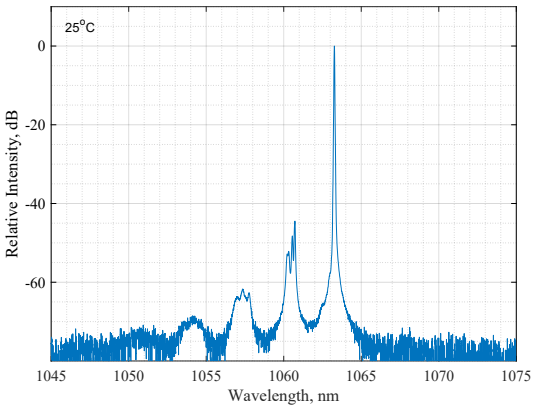

(a) $T = 25°C$.

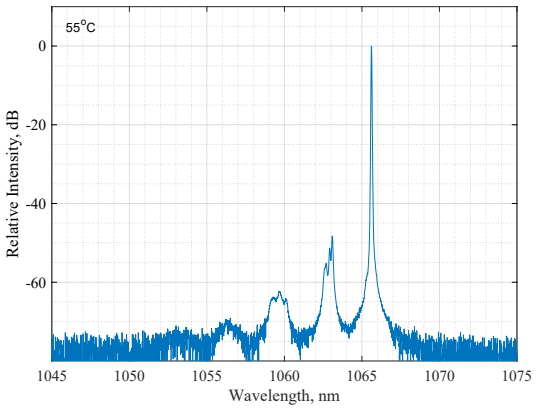

(b) $T = 55°C$.

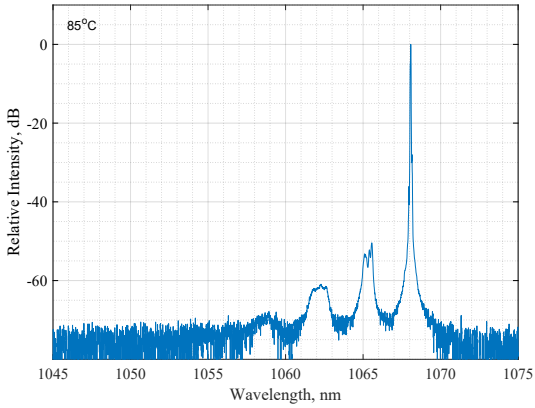

(c) $T = 85°C$.

Figure 6.11: Spectra for D2 obtained with $I_b = 3mA$ for three different temperatures.

above 1061 nm no peak is present since those values correspond to energies lower than the band gap and so it is natural to not have emission of light. In this region what is measured is said to be the background noise that includes noises from the environments, fibers and connections between fibers and device[28]. Indeed such noise is present also in the transitions zone between one peak to another. Usually it takes some trials to get a spectrum with the background noise attenuated of more than $60dB$ as done in this thesis. With increasing temperature three effects can be seen. The first two have also been analysed in the theoretical gain, see figure 5.8: the shift of the wavelength peak towards

[27] From previous work at Chalmers on 850 nm VCSEL.

[28] In most of time the used fiber is a single-mode fiber working around 1060 nm, however in some cases a multi-mode fiber is needed. This comes from the fact that some components require a multi-mode fiber to work, es. the bare fiber ends that souhld be connected to the spectrum analyzer is by construction a multi-mode fiber. Being that the shapes of these two type of fibers ends is different, the coupling efficiency between the two is lower with respect to a case of cables of the same type. And so additional losses are present.

higher wavelength and the decrease of the output optical power (which depends on the gain of the active region). It is interesting to note that the entire spectrum shifts towards right, confirming that the implemented equation 5.23 for the temperature shift in Chapter 5 is consistent with the experiment. The third effect is an increase of the noise in the transitions between the different peaks which are now more attenuated. In fact now the closest mode is attenuated around $40dB$ making the VCSEL actually truly single-mode. D2 and D2SE07, figure 6.11 and 6.12 respectively, shows how the temperature acts similar also on different designs as expected. In fact, being the effect mainly related to the active region, no big difference should arise since the three chosen VCSEL have the same QWs. Nonetheless here the peak wavelength takes higher value with respect to D1 meaning that the detuning due to the DBR mirrors is higher in the second design. What's more is that both D2 and D2SE07 are single modes, with D2 being the best one among the three, since the non fundamental modes are more suppressed.

Thus the difference in spectrum between the two lies in the aforementioned peaks number

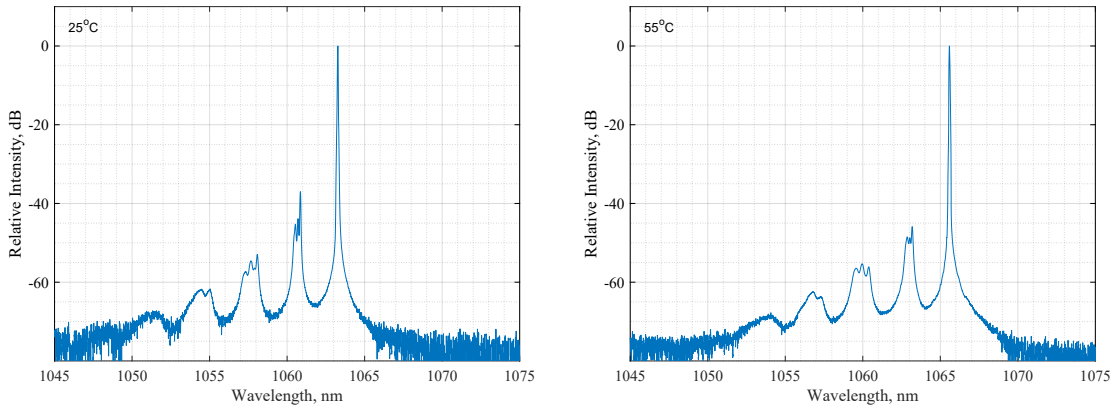

(a) $T = 25°C$. (b) $T = 55°C$.

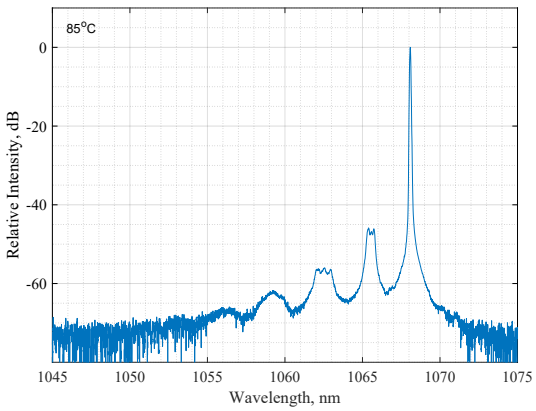

(c) $T = 85°C$.

Figure 6.12: Spectra for D2SE07 obtained with $I_b = 3mA$ for three different temperatures.

mismatch. Table 6.1 contains the measured peak wavelength. It is clear that D2 and

D2SE07 are almost equal with difference near the resolution of the spectrum analyzer thus negligible.

Also it is interesting to note that the changes of the peak wavelength with temperature

Table 6.1: Peak wavelength position for different temperatures.

Device	$25°C$	$55°C$	$85°C$
$D1$	1060.85	$1063,22$	1065.71
$D2$	1063.26	$1065,61$	1068.07
$D2SE07$	1063.27	1065.58	1068.08

is similar in all three devices: in fact from $25°C$ to $55°C$ the increase is of $2.3°C$ for approximately all of them, while from $55°C$ to the maximum temperature for D1 $2.49°C$, D2 $2.46°C$,and D2SE07 $2.5°C$. Such small differences can be related not only to the designs itself, but also to the measurements condition, i.e. spectrum analyzer accuracy (0.02nm), temperature oscillations, and the bare fiber positioned in the optimal position to have the maximum coupling with the VCSEL output light. At this point that all the data about spectrum and IPV are available, the linewidth can be calculated in all the cases. It is important to remark that, since the emission at higher wavelength is lower, we expect the overall measurements of the linewidth to be higher in value due to the lower output power and the increased noise in the system. Before doing that a discussion about the near field spontaneous emission of the VCSELs is done in the next Chapter.

Chapter 7

Near field spontaneous emission

A last static characterization performed is the imaging of the near field spontaneous emission. This is done in order to better see the difference between the different carrier confinements in D1 and D2.
Such task must be performed by biasing the VCSEL with a current lower than the threshold current, in this way the majority of the output power comes from spontaneous emission events rather than stimulated emission (too low carrier density). The near field is a required characteristic since in lasers the output field will tend to spread itself in space making it necessary to have the microscope as close as possible to the VCSEL in order to capture the output field[29]. To visualise it thus a new set-up based on a microscope is used .

7.1 Set-up

The VCSEL's holder, which is moved very close to the microscope, does not allow for a temperature control restricting this characterization only at room temperature. The maximum theoretical distance at which the VCSEL can be placed is given by the Fraunhofer distance

$$d_F = \frac{2d^2}{\lambda}, \tag{7.1}$$

where d is the diameter of the radiator, assumed to be the oxide aperture. Since the whole VCSEL acts as an antenna, such expression is used here to get the order of magnitude of the output electric field. Considering the worst case for D1, $d_1 = 2.1\mu m$ and for D2 $d_2 = 4\mu m$, using the obtained values of wavelength at $25°C$ from table 6.1, the maximum distance are: $d_{D1,F} = 8.4\mu m$ and $d_{D2,F} = 30\mu m$. Meaning that for D2 the near field is obtained more easily.
This set-up does not have a placeholder for the previously used probes SG and GSG, instead two sharp metallic tips are controlled from the left and right side of the holder

[29]The theory behind the propagation of an electromagnetic field in the near and far regimes is not treated here since far from the topic of this thesis.

and placed on the G and S pads of the VCSEL. It is evident that such operation is more difficult to perform and can also damage the VCSEL more easily due to the tips being sharps. Then a $20x$ lens is used to magnify the image from the VCSEL directly in the microscopy. A *Spiricon SP928 CCD camera* is placed on the top of it to detect the incoming field from the microscope. Nonetheless, since the camera is highly sensitive, an optical filter is placed just before to attenuate the incoming field and avoid damages. Lastly the CCD camera is connected to a computer and the data is retrieved using the related software: *Beam Gage Professional*. The processed data was then imported and loaded into MATLAB.

7.2 Results

A good criteria to limit stimulated emission is to bias the laser with a current being half the threshold current. Thus from IPV measurements, figure 6.5(a) for D1 and 6.6(a) for D2, the bias currents used are $I_{b,D1} = 0.15mA$ and $I_{b,D2} = 0.075mA$.
The key point is to have the central part of the oxide aperture settled in the middle of the microscope, to do so the VCSEL is seen through the interface of *Beam Gage*, upon normal illumination from the microscope and recorded in figure 7.1

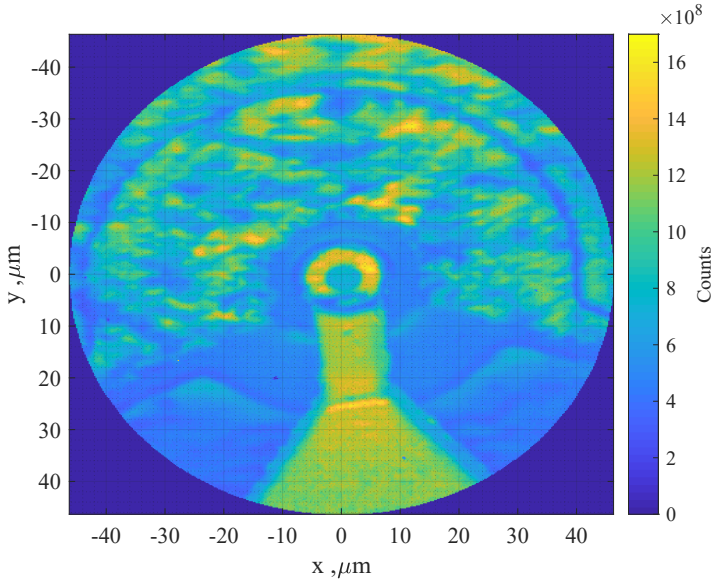

Figure 7.1: CCD camera view of the VCSEL.

Here the top ring and the related contact can be seen clearly since reflects more light (illumination from the top) also the mesa surrounding the upper part of the image is present. Such image is useful to retrieve the actual dimensions of the system with a diameter of the ring of the order of $10\mu m$.
The focus of the microscope is another aspect to be considered when preparing the system, in fact the real image seen here and the spontaneous emission need to be focused

differently. Otherwise the latter would be distorted into an oval geometry. Such problem arises also when switching from D1 to D2. Accounting for that effect and adjusting the focus figure 7.2 shows the final result.

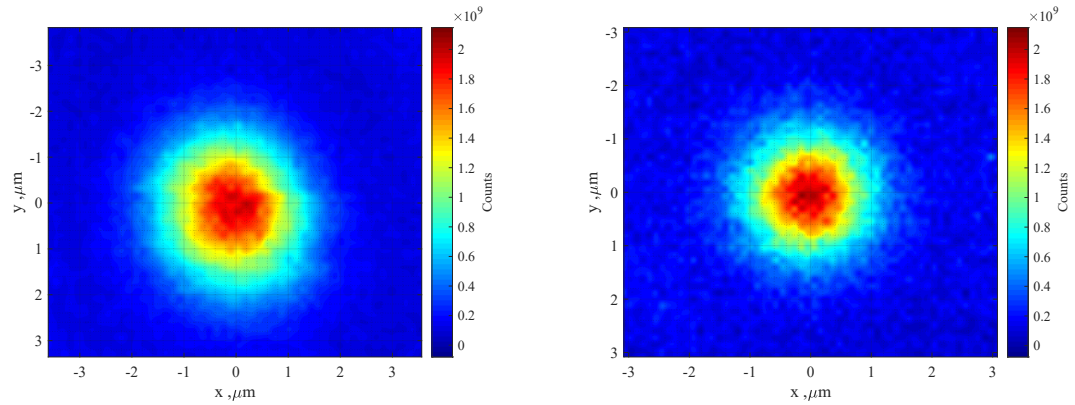

(a) D1. (b) D2.

Figure 7.2: CCD camera view of the output power.

To obtain these images the CCD camera options needs to be brought near the limit of detection (high exposition and resolution), due to the low intensity emission below threshold. From the comparison it is clear that D2 overall field intensity is more restricted and circular than D1. In fact a non-circular shape is usually referred to a multi-mode emission and imprecision in the oxide aperture geometry (not perfectly circular). Considering the nature of the two designs for D1 and D2, such result is in accord with [42]. In fact the strong carrier confinement device (D2) allows for an higher confinement transverse carrier distribution in the QWs that is reflected on the profile of the spontaneous emission being more restricted within the oxide aperture. Moreover this leads to a carrier distribution with a good overlap with the optical mode, increasing the stimulated recombination efficiency. While in the other case the lower confinement of carriers makes the output field spread more. A consequence of this unwanted effect is the increment of lateral leakages currents, which is one of the reason the strong carrier confinement was developed.
It is important to notice that the measured spontaneous emission is the total spontaneous emission of the system. For this reason relating it directly to the linewidth is not completely consistent with eq. 2.18. Nonetheless this gives us a good hint on the effect of the different confinements of the carriers on the system. Lastly a comparison between $D2SE07$ and $D2$ do not give satisfying results in terms of difference between the recorded emissions.

Chapter 8

Linewidth

In this last Chapter the linewidth is finally measured and compared with the theory. The method used to obtain it has been chosen between a variety of different set-ups, each one with its limitations and advantages. Two methods have been implemented: the Heterodyne and Scanning Fabry Pérot Interferometer (SFPI) method. In the end, however, the latter has proved to be more successful than the first one[30]. For this reason here the SFP is described. Nonetheless in the Appendix the Heterodyne and other methods are presented for a complete overview on the best possibilities currently available for linewidth detection.
The related measurements are presented in conjugation with the problems obtained.

8.1 Linewidth set-up: SFPI

The last used workplace is different with respect to IPV and spontaneous emission. Figure 8.1 contains the scheme of the set-up. The temperature controller implemented here is a *TED 350 temperature controller* which is more stable in maintaining an higher temperature with respect to the *Keithley* used for IPV and spectrum. While the current generator is of the same type of the previous ones.

Similarly to the spectrum case, here the goal of the first part of the set-up is to collect the light from the VCSEL. In this case two lenses are adopted to focus the light on an holder with an hole in the centre where a normal single-mode fiber is inserted. Both the lenses and the holder can be moved in three dimensions in order to optimize the coupling of the incoming light with the fiber input. This operation is the hardest to perform (due to the high precision needed in order to have a good coupling) and is probably the main drawback of this configuration with respect of using a bare fiber as done in the case of the spectrum. Nonetheless with the usage of lenses the focus in the fiber is much grater with respect to the other configuration.

[30] Two different set-ups where chosen in order to compare the results of one method with the other.

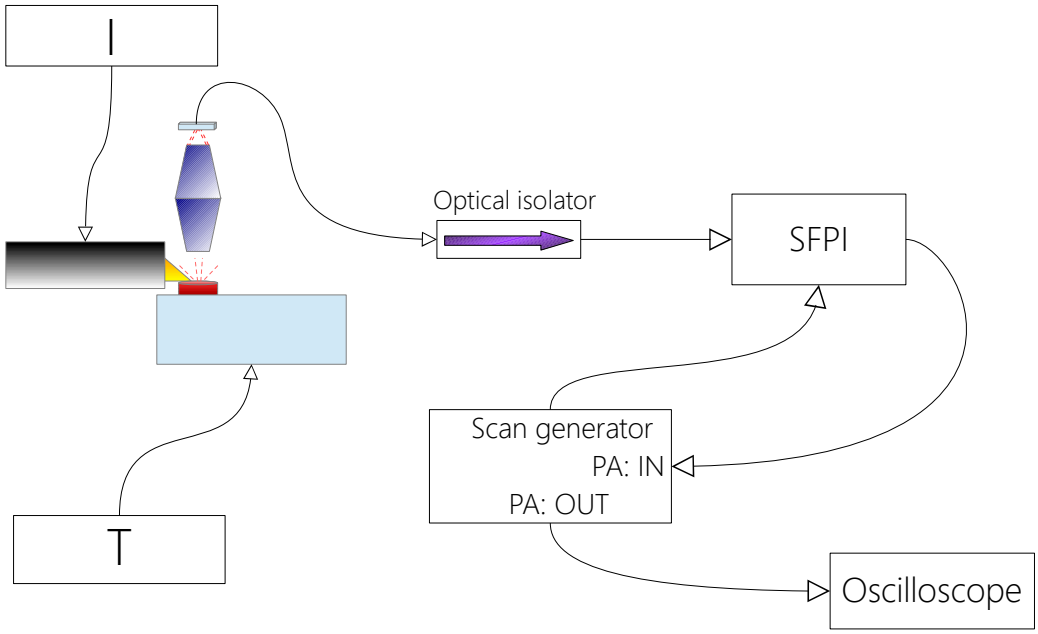

Figure 8.1: Simple sketch of the set-up for IPV measurements

At this point an optical isolator is used in order to avoid back reflection from the successive devices; in addition to this, also the holder introduced before presents a small tilting to further reduce unwanted light in the VCSEL.
At this point the light enters the SCFI itself. The device, a *Toptica FPI 100-980-3V0*, is composed in principle by two parallel spherical mirrors, which present a very high reflectivity (with the one of the input almost close to 1) so that the entered light undergoes multiple reflections within the cavity. A small displacement is applied to one of the cavity mirror mounted on a piezoelectric transducer. This operation is done by tuning the ramp voltage applied to the piezoelectric elements using a *MINISCAN 102 scan generator controller*. When the mirror spacing becomes equal to an integral number of half the wavelength of the laser, constructive interferences occur leading to an output signal (the light passing the mirror is measured and converted to an electrical signal with a photodiode placed in the SFPI).
The signal from the scan generator is usually a triangle or saw-tooth wave with an adjustable frequency, amplitude, and offset. It is used to repetitively scan the length of the cavity by $\frac{\lambda}{4}$ in order to sweep through one FSR (Free spectral range) of the interferometer. With the latter being defined as the distance in frequency between consecutive output peaks. For this interferometer the FSR is $1GHz$.
It is then clear that the output signal is periodic with the periodicity related to the scan velocity given by the controller. However the outgoing signal from the SCFI is too low in magnitude to be accurately measured, for this reason a photodiode amplifier integrated in the scan generator is used. The final output is recorded on a digital oscilloscope *Rigol DS4014E Digital Oscilloscope*.

8.2 Linewidth measurement

Now the linewidth is finally measured. The bias current used ranges from 1.5 to $4mA$, smaller values may give output voltages not measurable on the oscilloscope especially at higher temperature where the magnitudes of the voltages decrease as seen before during IPV. While at higher currents it may damage the VCSEL.
Figure, 8.2 shows what is typically seen on the oscilloscope, here the output comes from D1 biased at $3mA$ at $25°C$. The voltage ramp from the scan generator is plotted too. The

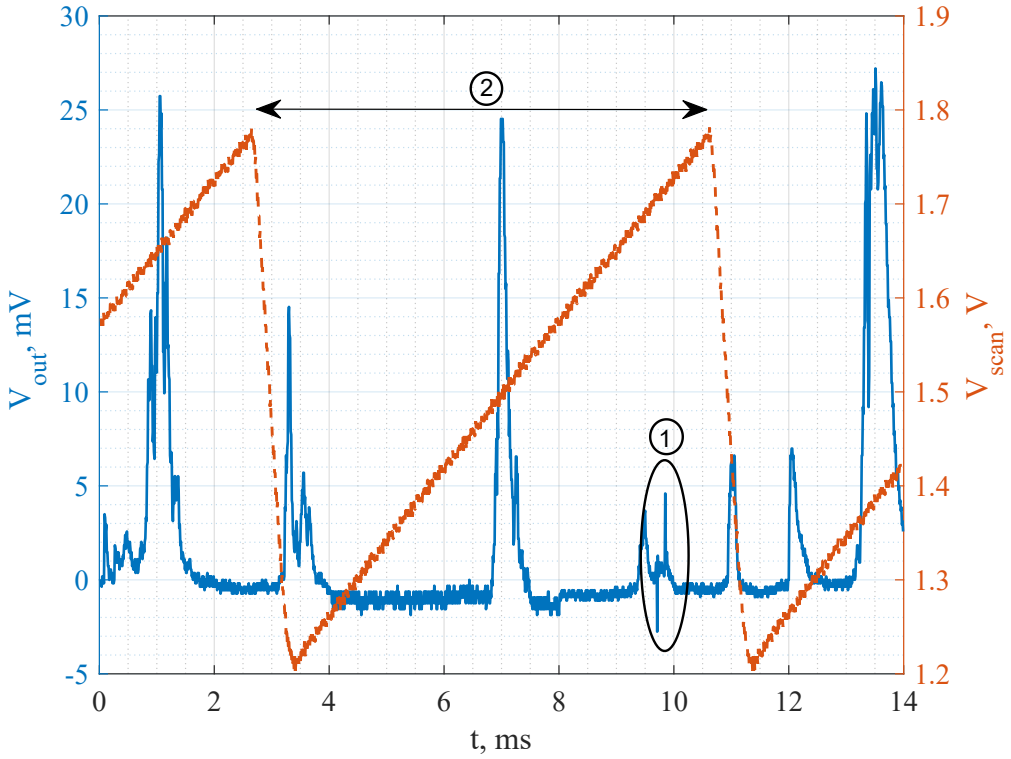

Figure 8.2: SCFI amplified output (left) and scanning voltage from the scan generator (right) seen on the oscilloscope for D1, $I_b = 3mA$ and $T = 25°C$.

first thing to notice is the non uniformity in the shape and number of the peaks for each ramp. Comparing with the literature [44] [45], such outcome is not present. Different VCSELs, of different type and categories, where probed, but the aforementioned problem was always present. In addition the output signal from the SFPI should be periodic with the scan generator, which is clearly not true here. The origin of these non ideality in the measure can be related to multiple reasons, different attempts where made to find a possible solutions.

- The first and more immediate explanation derives from the fact that the measured VCSEL is not completely single mode, so what is seen on the oscilloscope is the composition of different modes (this may be the reason for which some curves presents different peaks, i.e in figure 8.2 V_{out} at $t \approx 14ms$). Note that this problem is present

also in D2 and D2SE07 even if sometimes with less randomness in the peaks appearance as depicted in figure 8.3, meaning that this cannot be the only reason for the appearance of the output.

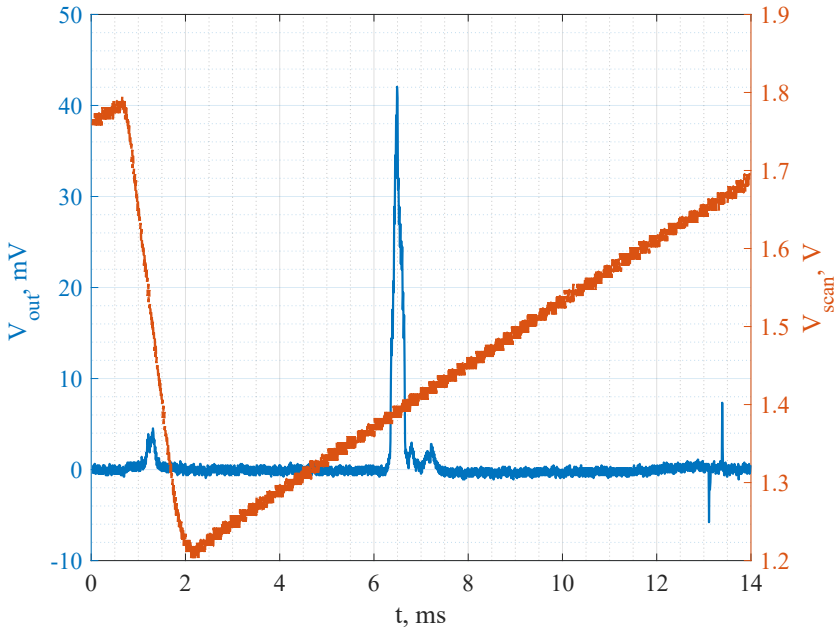

Figure 8.3: SCFI amplified output (left) and scanning voltage from the scan generator (right) seen on the oscilloscope for D2, $I_b = 2.2mA$ and $T = 25°C$.

- Another issue may rises from the direct set-up itself. A proposed explanation for such behaviour may be related to an hypothetical feedback of the light from the SCFI into the VCSEL causing large non-linearity in its output. However the tilting of the probe, in addition to the usage of an optical isolator, makes the reflected light from the SCFI (which is already very low by construction) almost zero.

- To actually see if the problem is related to the first part of the set-up, so to the probe and lens system, the set-up used for spectra measurements was tried. In this way the extremity of the bare fiber was connected to the isolator leaving the remaining part of the linewidth set-up untouched. In this contest no actual true change was recorded. Assuring that the probe is not the problem.

- Lastly the temperature and current generators where changed and different combination of them were analysed. None of these trials lead to the expected outcome. In this contest the assumption made about the current generator was that the non stability in the output current may case oscillations in the output frequency resulting in the randomness of the superposed peaks. Indeed two rather old currents generator, of the same type of the one for IPV and spectra, were used. If the problem was present in both of them then it is impossible to see an actual change.

As a result no actual successful improvement was made to solve such problem. Thus, in order to get a reasonable result for the linewidth, many different peaks are chosen for each measurement and fitted. Only the most suited value of linewidths retrieved for these results are kept. This process cannot be considered as rigorous, but upon discarding the curves presenting multiple peaks, reasonable values for the linewidth can be obtained. Another type of peak not to be considered is indicated in figure 8.2 as (1),since it is related to the SFPI itself. (2) is the period of the ramp voltage Δt_v, its role is fundamental in the calculation of the linewidth, in fact the conversion from the FWHM time measured on the fitted curve Δt_{line} to Hz is done as [44]

$$\Delta\nu_{exp} = \frac{\Delta t_{line}}{\Delta t_v} FSR. \tag{8.1}$$

In this case the period of the scan generator has always been kept constants and equal to $7.49ms$, thus the only unknown in the previous equation is Δt_{line}. The latter is obtained by taking the FWHM of the fitted curve. This procedure is based on fitting the curves with a Lorentzian profile of the type $L(X) = \frac{P_1}{((X-P_2)^2+P_3)} + P_4$ with the parameters P_i obtained in order to minimize the sum of the squared residuals between the original and fitted curve. In order to proceed with an accurate fitting the zone around the central peak[31] is zoomed and partially filtered to exclude excessive spikes. This is required, especially for higher temperature where the noise is higher, as it is possible to see from figure 8.4 (a).

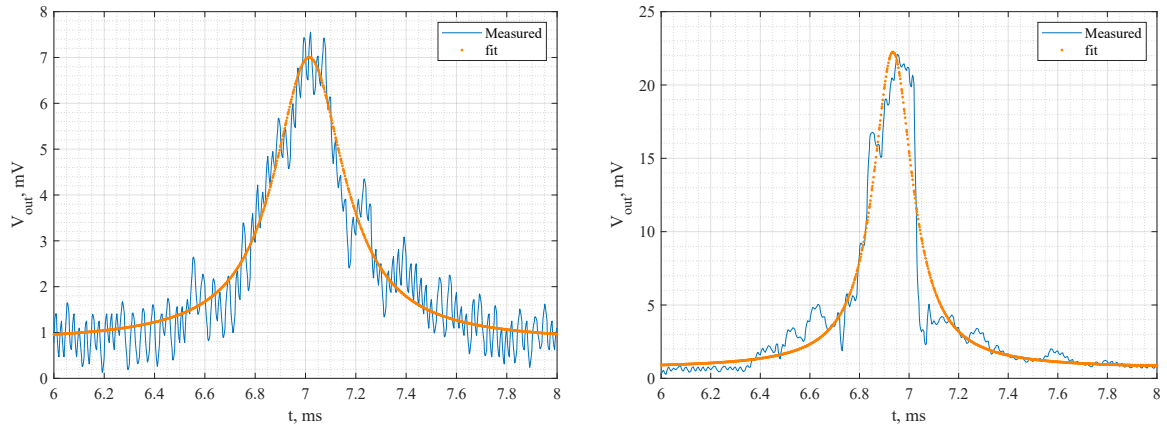

(a) D1, $T = 85°C$ and $I_b = 2.2mA$. (b) D2SE07, $T = 25°C$ and $I_b = 2mA$.

Figure 8.4: Measured and fitted profiles of SFPI amplified output.

The fitting procedure is, in most of the time, successfully performed, expect in some cases where the curve shape presents many spikes. The previous figure shows this discrepancy. In (a) case the fitting gives a good result, while in (b) not completely. The reason is that the curve in (b) does not resemble a Lorentzian shape, meaning that many different noise

[31] After every measurement the peak is manually centred on the digital oscilloscope before saving the result.

sources are present. In other words we see how the problem in the measurement highly affects the final determination of the linewidth.
For those cases the associated error is then higher. By performing the fitting for all temperatures and bias current and using eq. 8.1 with the extrapolated FWHM from each curve, the linewidth is obtained. Figure 8.5 shows the three device linewidths plotted with respect to the inverse of the power obtained from IPV measurements. Here a linear interpolation is performed to actually see the non ideal linear behaviour. The intercept with the y axis should be zero, however due to noise from the instruments such as the current generator, temperature controller, cables and SFPI itself, it has a value larger than zero, which is called residual linewidth. We expect this number in principle to be equal for all the cases. However such task is nearly impossible, because, when changing from one VCSEL to another, the lenses have to be adjusted in order to focus the light in the fiber[32]. While when increasing the temperature for a fixed VCSEL, the temperature controller noise increases due to the larger fluctuation of temperatures. Nonetheless the range in which the residual linewidth takes values is close between the different VCSEL. Comparing D1 and D2, the most important result is that on the whole D2 has a lower linewidth. This means that the weakly carrier confinement design is so detrimental, even if the dimensions of D1 are lower with respect to D2. An additional hint on such result is given by IPV measurements: D2 output power is higher leading to a better coherence time (see eq. 2.16) of the output beam [7]. So the carrier confinement actually makes the spectral width of the output beam lower than in the case of D1 [10].
In addition to this, D2SE07 shows an higher linewidth than D2. In order to give an explanation, we should consider the related IPV, figure 6.6 and 6.7. In fact for D2 the threshold gain must be higher with respect to the D2 case since here photons escapes the cavity faster by design. Thus, to reach lasing, more carrier density is needed. As a result the spontaneous emission is higher since it depends directly on the threshold gain, eq. 2.11. This can also be noticed in the fact that D2SE07 has a threshold current twice the one belonging to D2.

8.3 Theory comparison

In this last section, the results obtained from the theory are used to fit the slope of the straight lines approximating the previously obtained linewidth . To do so eq. 2.18 is implemented by inserting the theoretic E_s and α. While λ_{peak} is directly taken from spectra measurements by looking at the wavelength corresponding to the maximum emission. In order to select an appropriate value for E_s and α, it is necessary to find the carrier density at threshold. In fact looking at eq. 2.11, the value of spontaneous emission is defined

[32]Banally, since D1 hs a lower oxide aperture than D2 the beam light escaping the VCSEL will have different size, thus a new focus must be established

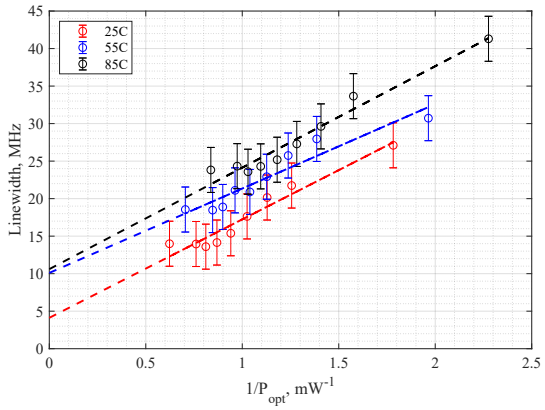

(a) D1.

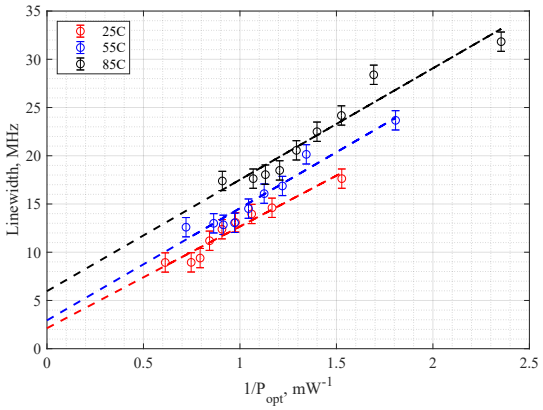

(b) D2.

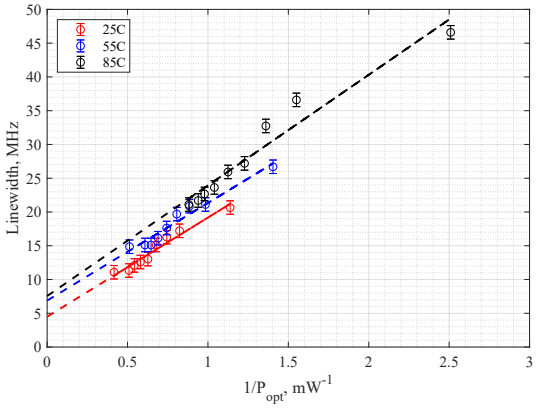

(c) D2SE07.

Figure 8.5: Linewidth results for different temperature for all three devices.

at threshold, so a proper value for G_{th} must be used. Once known, the value of carrier density giving $G(N) \approx G_{th}$ is extracted, and the spontaneous emission and linewidth enhancement factor related to that particular carrier density are considered.
What remains are the confinement factor Γ and τ_m. These values, in conjugation with G_{th}, are obtained from VELM simulations and fitted in order to match the measurements. Figure 8.6 shows the obtained results from the simulation using the values from table 8.1. Here the Γ factor is exactly the one obtained from VELM, which is assumed to be constant with temperature. So variations from the refractive index and electric field in the cavity are neglected, since the confinement factor depends on those.
Looking at the threshold gain, it is clear that D2SE07 has the largest values as a consequence of the highest slope efficiency and thus faster loss of photons from the cavity. Such concept is also partially described by τ_m^{-1}, in fact higher values are reached in the case of D2SE07 meaning that more photons are lost through the mirror per second[33]. While

[33]For sake of completeness, the values for τ_m from VELM simulations in the case of D1 and D2 are around $5ps$. In this way the difference between D1/D2 with D2SE07 is more evident since both D1 and D2 have $\eta = 0.5\frac{W}{A}$. The fitting cause this concept to be partially lost.

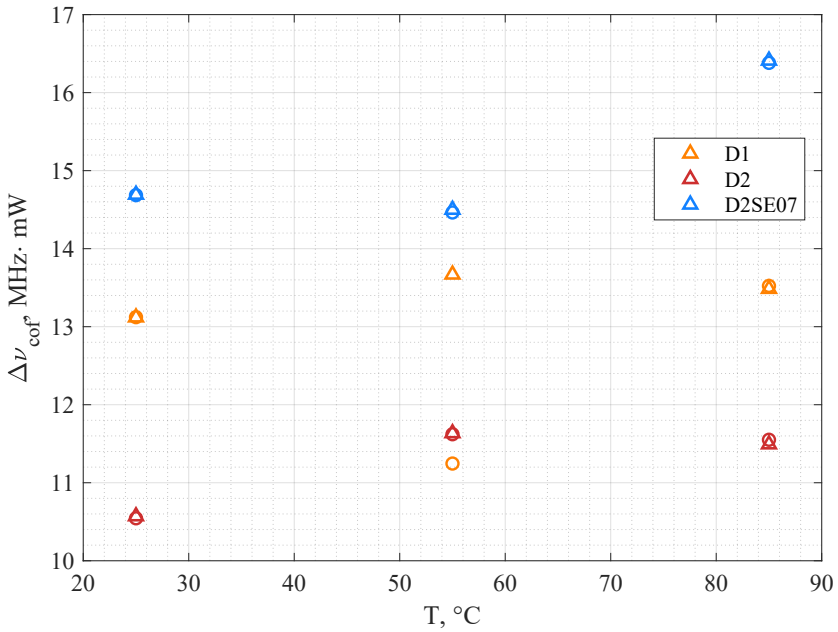

Figure 8.6: Linewidth normalized with respect to the power vs temperature for all three devices. Circles represent the experimental values, while triangles the theoretic ones.

between D1 and D2, the second has a lower threshold gain thanks to the strong carrier confinement which reduces leakages due to current spreading.
Looking at the figure, D2 and D2SE07 are very well approximated, while D1 presents a discrepancy at $55°C$. This result is expected, in fact looking at the experimental linewidth in figure 8.5, the slope of straight line at that temperature is most likely to be wrong since it will intercept the line related to the $25°C$ case. Nonetheless D1 results for the linewidth are those which present the higher errors in the data, thus a better slope can be obtained by proper re-arrangement of the values.
It is interesting to see that all three devices do not present a monotonic increase as expected from common theory [5]. Indeed obtaining a perfect behaviour is impossible in this case due to all the aforementioned problems, nonetheless the single values of linewidth from each device respects the theoretical assumption (except for two cases as in (b) of figure 8.5 near $1mW^{-1}$). In other words, for a fixed bias current, the obtained linewidth is always larger than one at a lower temperature.

Table 8.1: Parameters for the fitting of the normalized linewidth.

VCSEL	$D1$			$D2$			$D2SE07$		
T	$25°C$	$55°C$	$85°C$	$25°C$	$55°C$	$85°C$	$25°C$	$55°C$	$85°C$
G_{th}, cm^{-1}	2790	3348	3625	1792	2590	2824	3388	3726	5064
τ_m, ps	1.11	1.13	1.14	1.23	1.25	1.26	1.08	1.12	1.13
Γ		0.025			0.027			0.027	

In addition is evident that D2SE07 present the highest slope, such result comes from the power related to the minimum bias current, $1.5mA$. In fact since the threshold current for D2SE07 at 85° is very high ((c) figure 6.7), when probing at $1.5mA$ the output power is quite low then $\frac{1}{P_{out}}$ is very high.

Chapter 9

Conclusion

This project focused on the analysis of the linewidth of VCSELs, with great importance on the different involved physical quantities. From the theoretical point of view the attention was put mainly on the computation of the sub-bands and gain in a strained quantum well, rather than a complete description of the linewidth in a laser. In this contestn, the given code from the Microwaves and Optoelectronics group has been revised and updated in order to better describe quantum wells where the strain is present, thus it can also be used for VCSELs not necessarily emitting at 1060 nm by simply setting the constants and doping for the selected materials. Due to time reason and length of the project, a complete discussion on the strain action (with comparisons between strained and unstrained quantity) on the gain, spontaneous emission and other quantities involved in the description of the quantum well were not included.
The experimental measurements were a fundamental part of this project. The availability of three different VCSELs, each with distinct designs, made it possible to perform an in depth description of their power, spectra and linewidth. Considering all the included results, it is clear that the D2 VCSEL is by far the best one among the three in terms of performances, bandwidth and linewidth. Nonetheless the linewidth of D1 is of the order of MHz too, thus it could find applications in those cases where smaller lasers are needed still maintaining an acceptable coherence in the output beam.
Unfortunately the problems in this thesis were mostly related to the measurement of the linewidth. In fact, of the two chosen set-ups, only the SCFI has been a reliable choice. Considering the entity of these problems, the obtained results for the linewidth can be seen as satisfying. In fact they were in accord with all the expectations. While in the case of the normalised linewidth the problems in the measurements are evident.

9.1 Future work

The extension of the code for the strained QW may be useful for the implementation of different VCSELs active regions. Moreover a full inclusion of the gain code into VENUS can hugely benefit of the improved description, while IPV and spectra may be used as a validation tool for output simulations. A more generalised linewidth implementation could also be introduced in order to better fit the experiment.
At the same time, the two linewidth set-ups are ready at Chalmers. Thus linewidth measurements on 1060 nm VCSELs can be repeated in the future hopefully improving the present results. In case the problems persist, additional options such as not using the optical isolator should be taken into account.
Lastly, seeing how good the D2 VCSELs are, an higher focus on this type of devices for future applications may be of great interest.

Appendix A

Techniques for linewidth measurements

Many differents method were considered for linewidth detection, in this appendix all the possible set-ups are briefly exploained with every listed configuration deriving from the reference.
We start by considering the simplest method and then go to more sophisticated ones. In the beginning we consider a general case of a laser, later on some set-up of VCSEL are shown.

Generic Laser

Heterodyne technique

From [46] some typologies of measurements are introduced. The Heterodyne is the simplest one. It is generally based on the mixing of a weak input signal with a reference one in a non-linear device such as a rectifier, and the resulting mixing product is then detected often after filtering out the original signal and the local oscillator frequency. The frequency of the mixing product is the sum or the difference of the frequencies of the signal and the local oscillator. For our purpose we are interested in the difference of the two main frequencies of the two sources.
In the case of optical signals, which is our case, the mixing product is not obtained by mixing the signal and local oscillator wave in a non-linear crystal, but by detecting the linearly superimposed waves with a photodetector, typically a photodiode. In addition a beam combiner is used to align the two beams such that they are mode-matched, meaning that their intensity profiles overlap together with their wavefronts, so that the interference conditions are uniform over the full detector area. Of course, this is possible only if the two beams are spatially coherent. In a fiber-optic set-up, a fiber coupler would be used instead of the beam splitter, and all fibers would be single-mode fibers, possibly of polarization-maintaining type; the mode matching is then guaranteed without a special

alignment (information given from RF photonic).
Figure A.1 shows one of the simplest set-up. An additional laser is required to act as a reference whose operating frequency is the same of the tested laser. Moreover it has to have a narrower linewidth with respect to the tested device[46]. Here we see the fiber

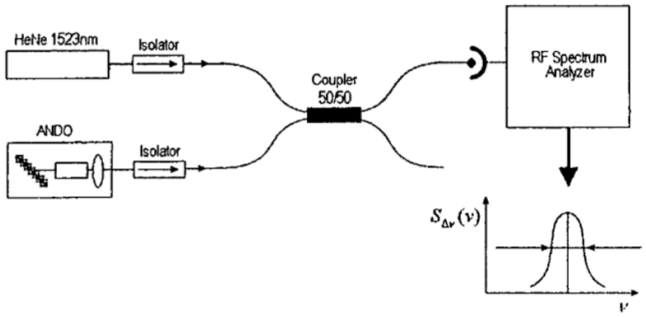

Figure A.1: Heterodyne set-up for estimation of the linewidth of tunable semiconductor laser.

coupler used to couple the two lasers, the resulting output is then detected by a normal RF Spectrum. Although the set-up is really simple, we need an additional laser as said before. In our specific case, if one wants to measure the linewidth of different VCSEL operating at different frequencies es. 1060 and 850 nm VCSEL, we should have either a tunable laser operating in the required range or an additional laser reference for each different operating frequency.

Self-Homodyne technique

Another solution, that avoids the use of a reference laser, is the Self-Homodyne method. Figure A.2[46] shows the basic set-up: The input radiation is injected into a Mach-Zehnder

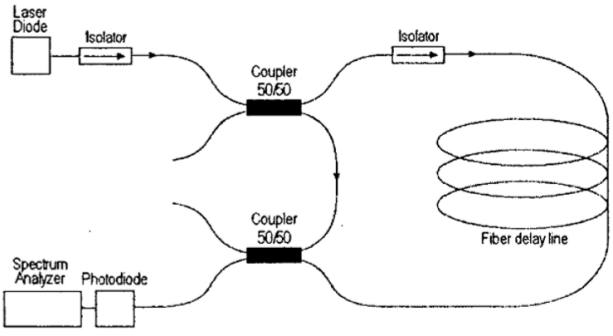

Figure A.2: Delayed self-homodyne set-up.

interferometer and split into two unequal arms. The output signal is then the combination of the original field and the delayed one. To have the actual working of this method the delay time τ_d of the delay fiber must be much larger than the coherence time of the laser

emitted beam. As a result the situation is similar to when we have a superposition of two different uncorrelated lasers. Here we surely have that the two superimposing waves share the same frequency since they come from the same laser. Always from [46] the resulting measured linewidth is twice the real one of the laser. However an important drawback is that, in this method the amplitude noise (noise related to the optical power) is present together with the phase noise, thus the self-homodyne technique cannot be chosen for a good linewidth measurement. Lastly the optical Isolator is used to direct light in only one direction and avoid returning signals to the source (unwanted feedback).

Self-Heterodyne technique

To overcome the previous problem one has to shift the frequency of the radiation of one of the two arms by a reasonable amount of offset frequency that from [46] is quantified in $10-100MHz$ using an acusto optic modulator, that modulates and controls the intensity of an optical beam. In this way we may mitigate the effect of the intensity noise. Note that now the linewidth plot is no more centred at zero but at the AOM frequency, allowing for much better precision. Figure A.3 shows the complete set-up.

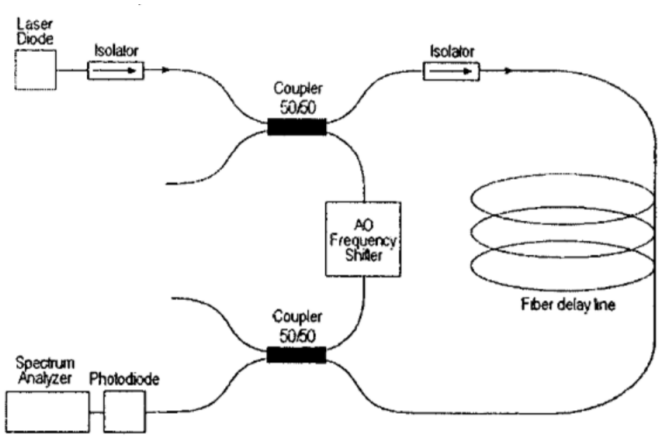

Figure A.3: Delayed self-heterodyne technique set-up.

Also [47] gives the same instrumentations for the self homodyne and heterodyne set-up, confirming the validity of these configurations. Here the reason for the use of an AOM is well described. In fact for RF analyser it is harder to fit the spectrum since it has poor response at low frequencies, moreover one also loose half the spectrum below zero making the final fitting much harder.

Self-Heterodyne technique with ring interferometer

An additional improvement to the set-up is proposed in [48][34]. It is also explained that to increase the resolution and also measure narrow linewidths, the fiber used for the

[34] Also here the normal self-heterodyne method shares the same configuration of the previous references.

delay must be very long. For this reason the authors substitute it with an oscillator ring. The working principle is associated to figure A.4:one beam is directly coupled to a PD (photodiode) and used as a local oscillator. The other beam circulates in the interferometer, and a portion of the circulating beam is coupled to the PD through the FC (fiber coupler). The circulating beam receives a time delay τ_d and a frequency shift ω_s from the delay fiber and the AOM, respectively. Therefore the beam after n circulations it has a delay time of $n\tau_d$ and a frequency shift of $n\omega_s$ with respect to the local oscillator. So one may achieve even better results with respect to the normal self-heterodyne method. Moreover the normal frequency shifts of the AOM should not be too high or the final resulting frequency would be too high too. In this case the problems is related to the losses

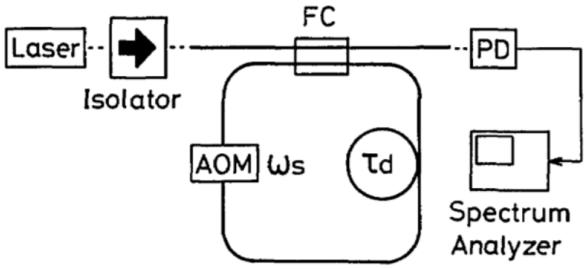

Figure A.4: Improved delayed self-heterodyne technique set-up.

of AOM, especially at high frequencies. As a consequence an additional improvements may be the implementation of a low-loss fiber-optic frequency shifter. Nonetheless the resolution achieved experimentally is only twice that of the conventional method.

Self-Mixing Interferometry

The last technique chosen to measure the linewidth of a laser is reported in [49]. It is based on the measurements of the phase noise, cause of the linewidth, in a self-mixing interferometer. However this type of set-up is based on making the light re-entering the laser, so it may be not suitable for the VCSEL case. For completeness figure A.5 shows the set-up. Light is focused onto a target stuck on a loudspeaker to which a sinusoidal drive signal is applied to make it move. The target can be a mirror or, to have a self-aligned set-up, either a corner-cube or reflective adhesive tape. The variable attenuator is used to obtain the proper feedback level. The self-mixing signal is collected by the monitor photodiode at the rear facet of the laser diode, is amplified, and then sampled by a digital sampling oscilloscope.

The basic idea is that the reflected light from the target, by interacting with active medium of the laser and the lasing field, withstands a modulation of the emitted power which is called self-mixing signal. With a moderate feedback(10^{-6}) and a high enough Distance, the self mixing signal becomes distorted and sawtooth-like. Then it can be retrieved by

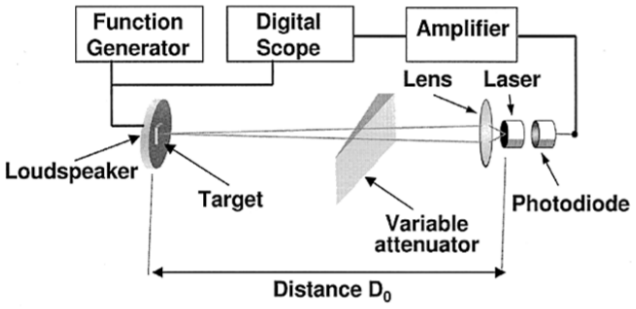

Figure A.5: Experimental setup for self-mixing interferometry.

sampling the waveform with an oscilloscope. Each point of the waveform is recorded after a trigger signal represented by the driver signal. Figure A.6 shows what [49] obtained. The phase noise is obtained by setting it as the variance parameter of the random spikes in the sawtooth waveform transitions between a low (switching not yet occurred) and high state(switching occurred). Thus the probability of the state of the point being "high"

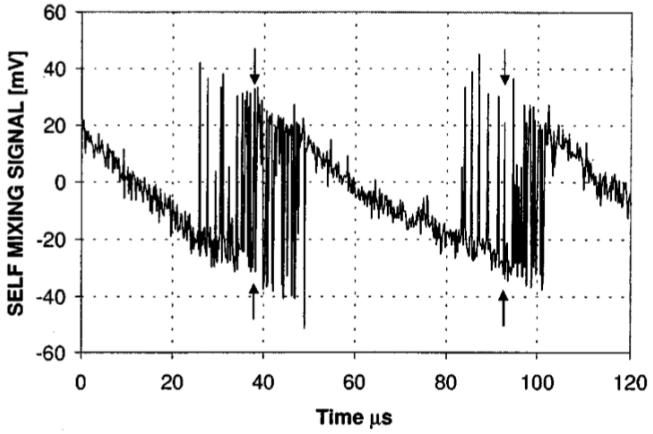

Figure A.6: Self-mixing signal waveform with phase noise, sampled by a digitizing oscilloscope.

or "low" is obtained as a function of the phase noise variance. The resulting total curve will have a maximum whose value of abscissa corresponds to the most probable value of phase noise.
By measuring many values in this way, also varying a little the distance, the linewidth of the laser can be obtained.

VCSEL Linewidth measurements

In this last part, we see which one of the previous methods were used to measure the linewidth of a VCSEL in conjuction with the SCFI. In the paper of Martin and others [50]

the Heterodyne technique was used together with a tunable laser as shown in figure A.7 set-up. Here the configuration is quite simple, the VCSEL is controlled in temperature,

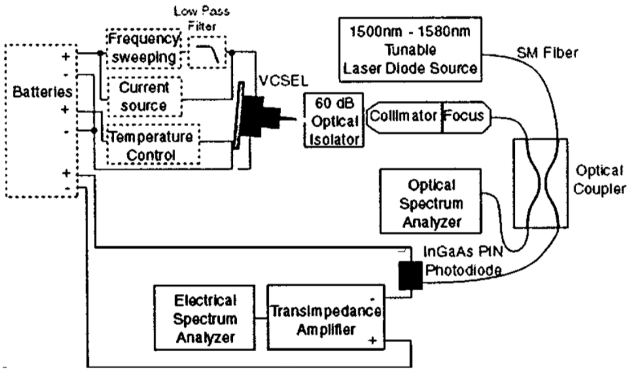

Figure A.7: Schematic of the heterodyne setup for linewidth measurements

current and frequency. While at the same time is tilted (in the laboratory the tilting is applied to the holder of the fiber and never to the VCSEL itself) to prevents feedback in the cavity. Also here the optical isolator is included for further attenuation of back reflections. In addition, the optical spectrum analyser used for spectra measurements is useful in this situation to see if the tunable laser has an operating wavelength very close to the one of the VCSEL. This overall configuration may be a good candidate, even if the problem of the normal heterodyne method is present thus requiring the use of a AOM.
Also the analysis done in the report [51] is based on the normal heterodyne method, figure A.8 is the last proposed set-up. Again we see that the authors choose to use another laser as a reference instead of the long line delay fiber. This last configuration is very similar to the previous ones. Also here it is remarked that the linewidth of the local oscillator (reference laser) MUST be narrower than the one of the analysed set-up. Moreover here we have again an Optical Spectrum Analyser to better align the two wavelength. To measure the linewidth, a pin photodiode connected to a Transimpedance Amplifier which converts the received current in a voltage measured then by the Electric Spectrum Analyzer (ESA).

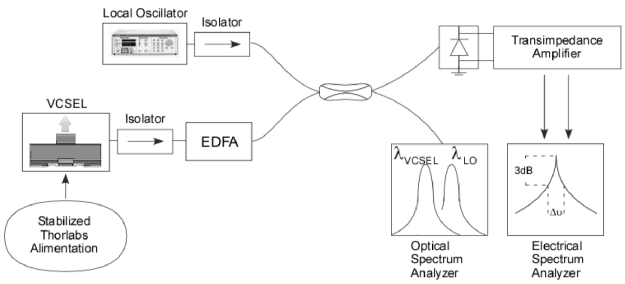

Figure A.8: Optical Heterodyne set-up

Conclusion

Comparing all the results and different set-ups done by the various authors, we may conclude that the Heterodyne set-up is a good solution for linewdith measurements, even without the AOM. The preferred solution is thus based on using a tunable laser as a reference laser with respect to the use of a fiber line for two reasons:

- The length of the line must ensure a time high enough causing to have very long lines in the extreme case. Then if one has to make multiple measurements on different VCSEL, the worst scenario where the longest line is needed has to be taken into account.
- Long lines may cause additional losses and make the overall performances decrease.

In the end the heterodyne method together with the SFPI were successfully implemented and used to retrieve the linewidth. However the first method gave un-consistent results. In fact for a current equal to 1,2 and 3 mA the linewidth of D1 was in all the case equal to approximately 20 MHz. For this reason, and considering the short amount of time available for measurements at Chalmers, only the SFPI was further investigated.

Bibliography

[1] Alberto Tibaldi, Francesco Bertazzi, Michele Goano, Rainer Michalzik, and Pierluigi Debernardi, "VENUS: a Vertical-cavity surface-emitting laser Electro-opto-thermal NUmerical Simulator," *IEEE J. Quantum Electron.*, Vol. 25, Issue: 6, 2019.

[2] Anders Larsson, "Advances in VCSELs for Communication and Sensing," *IEEE J. Quantum Electron.*, Vol. 17, Issue: 6, pp.2329–2330, 1979.

[3] Safaisini,R. et al., "20 Gbit/s data transmission over 2 km multimode fibre using 850 nm mode filter VCSEL," *Electronics latters*, Vol. 50, pp.40-42, 2014.

[4] Åsa Haglund "Mode and polarization control in VCSELs using surface structures," *Doktorsavhandlingar vid Chalmers Tekniska Hogskola* , PhD thesis, Issue: 6, Göteborg, 2005.

[5] Larry A. Coldren et al., "Diode Lasers and Photonic Integrated Circuits," *Wiley series in microwave and optical engineering*, Second edition, 2012.

[6] Haruhisa Soda, Ken-ichi Iga, Chiyuki Kitahara and Yasuharu Suematsu, "GaInAsP/InP Surface Emitting Injection Lasers," *Japanese Journal of Applied Physics*, Vol. 18, Issue: 12, 2011.

[7] Darwin K. Serkland, Weng W. Chow, Kent M. Geib, and Gregory M. Peake, "Narrow-Linewidth VCSELs for Atomic Microsystems," *Sandia National Laboratories* , California, 2011.

[8] G. P. Bava, P. Debernardi, and L. Fratta, "Three-dimensional model for vectorial fields in vertical-cavity surface-emitting lasers," *Phys. Rev.* , Vol. 63, Issue: 2, 2001.

[9] P. Debernardi, "HOT-VELM: A Comprehensive and Efficient Code for Fully Vectorial and 3-D Hot-Cavity VCSEL Simulation," *IEEE J. Quantum Electron.*, Vol. 45, Issue: 8, pp. 979–992, 2009.

[10] A. Larsson, E. Simpanen et al, "1060nm VCSELs for long-reach optical interconnects," *Science Direct*, Vol. 44, pp. 36-42, August 2018.

[11] P.J.A.Thijs et al, "Strained-layer InGaAs(P) quantum well semiconductor lasers and semiconductor laser amplifiers," *Science Direct*, Vol. 49,Issue: 3, pp. 187-224, 1995.

[12] N. J. Ekins-DaukesK, Kawaguchi and J. Zhang "Strain-Balanced Criteria for Multiple Quantum Well Structures and Its Signature in X-ray Rocking Curves," *Crystal Growth & Design*, Issue: 1, pp. 287-292, 2002.

[13] Peng Zhang et al, "Gain characteristics of the InGaAs strained quantum wells with GaAs, AlGaAs, and GaAsP barriers in vertical-external-cavity surface-emitting lasers," *Journal of Applied Physics*, Vol. 105, Issue:5, 2009.

[14] Ioffe Physico-Technical Institute, St. Petersburg, Russia, "Physical properties of semiconductors," http://www.ioffe.ru/SVA/NSM/Semicond/index.html

[15] M. G. Craford, D. L. Keune, W. O. Groves, A. H. Herzog, "The luminescent properties of nitrogen doped GaAsP light emitting diodes," *Journal of Electronic Materials*, Vol. 2, Issue:1, pp. 137–158, February 1973.

[16] R. People and J. C. Bean, "Calculation of critical layer thickness versus lattice mismatch for Ge_xSi_{1-x}/Si strained-layer heterostructures," *Appl.Phys.Lett.*, vol. 47, pp. 322-324, 1985.

[17] A. Larsson, "Semiconductor Optoelectronics Device Physics and Technologies," *Photonics Laboratory*, Department of Microtechnology and Nanoscience, August 2015.

[18] Chris G. Van de Walle, "Theoretical calculations of heterojunction discontinuities in the Si/Ge system," *Phys. Rev. B*, Vol. 34, Issue 8, 1986.

[19] Chris G. Van de Walle, "Band lineups and deformation potentials in the model-solid theory," *Phys. Rev. B*, vol. 39, Issue 3, 1989.

[20] J. Minch, S. H. Park, T. Keating, and S. L. Chuang, "Theory and experiment of $In_{1-x}Ga_xAs_yP_{1-y}$ and $In_{1-x-y}Ga_xAl_yAs$ long-wavelength strained quantum-well lasers," *IEEE J. Quantum Electron.*, vol. 35, Issue 5, pp. 771-782, 1999.

[21] Ratko G. Veprek, "Computational Modeling of Semiconductor Nanostructures for Optoelectronics," *Swiss Federal Institute of Technology*, 2009.

[22] Shun Lien Chuang, "Physics of Optoelectronic Devices," *Wiley Series in Pure and Applied Optics* , University of Illinois at Urbana-Champaign , 1995.

[23] Ratko G. Veprek, Sebastian Steiger, Bernd Witzigmann, "Operator ordering, ellipticity and spurious solutions in k · p calculations of III-nitride nanostructures," *Optical and Quantum Electronics*, vol. 40, Issue 14-15, pp. 1169-1174, 2008.

[24] Peng-Fei Qiao, Shin Mou, and Shun Lien Chuang, "Electronic band structures and optical properties of type-II superlattice photodetectors with interfacial effect," *Optical Society of America* , vol. 20, Issue 3, pp. 2319-2334, 2012.

[25] Yoon-Suk Kim et al., "Accurate band structures and effective masses for InP, InAs, and InSb using hybrid functionals," *Physical Review B*, vol. 80, Issue 3, 2009.

[26] E. O. Kane. "Handbook on Semiconductors," *Ed. W.Paul* , vol. 1, 1982.

[27] M G Burt, "The justification for applying the effective-mass approximation to microstructures," *Journal of Physics: Condensed Matter* , vol. 4, pp. 6651-6690, 1992.

[28] P. Yu and M. Cardona, "Fundamentals of Semiconductors," *Springer Berlin*, 2005.

[29] Bradley A. Foreman, "Elimination of spurious solutions from eight-band $k\cdot p$ theory," *Physical Review B* , vol. 56, issue: 20, November 1997.

[30] Claudine Hermann and Claude Weisbuch, "$\vec{k}\cdot\vec{p}$ perturbation theory in III-V compounds and alloys: a reexamination," *American Physical Society*, vol. 15, issue: 2, p. 823, 1997.

[31] Claudine Hermann and Claude Weisbuch, "A new method of calculating the energy spectrum of carriers in semiconductors. I. neglecting Spin-Orbit interactions," *Soviet physics JETP*, vol. 14, number 2, 1962.

[32] G. L. Bir and G. E. Pikus, "Symmetry and strain-induced effects in semiconductors," *New York, Wiley*, 1974.

[33] Guobin Liu and Shun-Lien Chuang, "Modeling of Sb-based type-II quantum cascade lasers," *Phys. Rev. B*, vol. 65, Issue 16, 2002.

[34] Guobin Doyeol Ahn and Shun-Lien Chuang, "Optical gain in a strained-layer quantum-well laser," *IEEE J. Quantum Electron.*, Vol. 24, Issue: 12, 1988.

[35] G. P. Bava, P. Debernarni and X.Z. Lin, "Optical gain in a strained-layer quantum-well laser," *Politecnico di torino,*, Internal report DE/GE 90-001.

[36] M. Asada, "A new density matrix theory for semiconductor lasers, including non-Markovian intraband relaxation and its application to nonlinear gain," *IEEE J. Quantum Electron.*, Vol. 25, Issue: 9, pp. 2019-2026, 1989.

[37] Guobin Doyeol Ahn and Shun-Lien Chuang, "A new density matrix theory for semiconductor lasers, including non-Markovian intraband relaxation and its application to nonlinear gain," *IEEE J. Quantum Electron.*, Vol. 27, Issue: 6, 1991.

[38] G. Ronald Hadley, "Effective index model for vertical-cavity surface-emitting lasers," *Optics Letters*, Vol. 20, Issue: 13, pp. 1483-1485, 1995.

[39] G. Ronald Hadley et al., "Comprehensive numerical modeling of vertical-cavity surface-emitting lasers," *IEEE J. Quantum Electron.*, Vol. 32, Issue: 4, pp. 607-616, 1996.

[40] Scott Wartenberg, "Rf Measurements of Die and Packages," *Artech House on Demand*, 2002.

[41] Emanuel P. Haglund et al., "Silicon-Integrated 850-nm Hybrid-Cavity VCSEL," *Chalmers Publication Library*.

[42] Erik Haglund et al., "High-Speed VCSELs With Strong Confinement of Optical Fields and Carriers," *Journal of Lightwave Technology*, Vol. 34, Issue: 2, 2016.

[43] E. Simpanen, J.S. Gustavsson et al., "1060 nm single-mode vertical-cavity surface-emitting laser operating at 50 Gbit/s data rate," *IEEE J. Quantum Electron.*, Vol. 53, Issue: 13, pp. 869-701, 2017.

[44] Adnan Hussein Ali et al., "Analysis of laser linewidth measurements based on Fabry Pérot interferometer system," *International Journal of Engineering & Computer Science*, Vol. 13, No. 01, 2013.

[45] Junwen Xue et al., "Pulsed laser linewidth measurement using Fabry–Pérot scanning interferometer," *Science direct: Results in physics* , Vol. 6, pp. 698-703, 2016.

[46] K. M. Abramski, W. Rodzen, P. R. Kaczmarek, L. Czurak, A. Budnicki "Laser diode linewidth measurements," *IEEE*, 2003.

[47] R. Phelan "Linewidth Measurement," *Eblana Photonics*, 2009.

[48] Hidemi Tsuchidaa "Simple technique for improving the resolution of the delayed self-heterodyne method," *Optics Letters*, Vol. 15, Issue: 11, pp. 640-642, 1990.

[49] Guido Giuliani, Michele Norgia "Laser diode linewidth measurement by means of self-mixing interferometry," *IEEE Photonics Technology Letters*, Vol. 12, Issue: 8, pp. 1028-1030, 2000.

[50] P. Signoret et al., "3.6-MHz linewidth 1.55-μm monomode vertical-cavity surface-emitting laser," *IEEE Photonics Technology Letters*, Vol. 13, Issue: 4, pp. 269-271, 2001.

[51] Alexandre Bacou, Angelique Rissons and Jean-Claude Mollier "Spectral behavior of long wavelength VCSELs," *SPIE. digital library*, 2008.